AALBORG UNIVERSITY
STUDENT REPORT

Development of driveability model for piles for offshore wind turbines

Master's thesis

by
Mads Helsager Harpøth

AALBORG UNIVERSITY
STUDENT REPORT

The School of Engineering and Science
Study Board of Civil Engineering
Thomas Manns Vej 23, 9220 Aalborg Ø
http://www.ses.aau.dk/

Title:

Development of driveability model
for piles for offshore wind turbines

Author:

Mads Helsager Harpøth

Project period:

February 2017 - June 2017

Delivered as partial requirement for obtaining the degree of Master of Science in Engineering (Structural and Civil Engineering) at Aalborg University, Denmark.

Supervisors:

Lars Vabbersgaard Andersen
Associate Professor, Aalborg University

Martin Underlin Østergaard
Geotechnical Engineer, COWI A/S

Front page picture:
Aerial photo of a part of the Anholt Offshore Wind Farm, Kattegat. Courtesy of DONG Energy A/S.

Thesis pages: 101
Appendix pages: 43
Completed: 8 June 2017

Synopsis:

This project contains a study of driveability analysis of offshore monopiles driven in sands, which identifies the key components, methods and models involved. The most commonly applied computer program used in these predictions is not truly dynamic and uses some assumptions which may not be appropriate for all situations. An input to the program, the static resistance to driving (SRD), along with a set of parameters relating the resistance to the stiffness and damping within the soil, are not uniquely defined. A thorough investigation into various SRD models is performed, which finds that the models are all semi-empirical and that they can not be expected to be reliable for conditions dissimilar to the conditions from which they were derived. A fully dynamic model seeking to overcome some of the simplifications, using three different discretization regimes for pile, side friction and tip resistance, and using a more advanced transient solving algorithm is developed and tested for sensitivity to model parameters. The SRD models are applied within the model to investigate their ability to reproduce an available driving record from a pile installed in the North Sea, and large variations in accuracy are found.

Dansk resumé

Efterspørgslen efter vedvarende energi er stigende. Dette er primært drevet af politiske mål om uafhængighed af fossile brændstoffer og bæredygtighed og har ført til en intens konkurrence på markedet for store elektricitetsproducerende vindmøller. En stadig større del af den samlede danske økonomi består af vindmøller og relaterede industrier, og området har derfor en særlig politisk bevågenhed herhjemme.

Landbaseret vindmøllestrøm kan under gunstige forhold konkurrere direkte med andre energikilder. Efterhånden som befolkningstætheden stiger, er det forventet at det vil blive vanskeligere at finde placeringsmuligheder for vindmøller på land. Derfor pågår der i øjeblikket en udvikling i markedet for havvindmøller, hvor der især inden for de seneste år er indviet adskillige meget store havvindmølleparker i farvande omkring bl.a. Tyskland, Storbritannien og Danmark.

Den mest almindelige og generelt mest økonomiske funderingsform for havvindmøller er en konstruktion bestående af en såkaldt *monopæl*, hvilket er en række sammensvejste, valsede stålrørssegmenter, som bankes ned i havbunden til en passende dybde, ofte mere end 25 m. Herpå placeres en tung stålkonstruktion designet for montage af mølletårnet.

Denne type fundamenter installeres typisk ved hjælp af hydraulisk drevne og accelererede faldhamre. Omkostningerne ved forsinkelser eller ved valg af for lille hammer for nedbringning til krævet dybde gør, at der kan være store økonomiske risici forbundet med installation af monopæle.

Ved opførsel af havvindmøller udføres som regel in-situ målinger i form af CPT bl.a. til brug for en såkaldt *driveability* analyse med henblik på bestemmelse af størrelse af hammer, som regel vha. af et *bølgeligningsprogram*. Dette involverer erfaringsbaserede modeller for jordens modstand (SRD-modeller), hvoraf adskillige eksisterer. Mange af disse modeller stammer fra installationen af væsentligt mindre pæle i olie- og gasindustrien, og effekten af større pælediameter og mindre fortrægningsevne er indtil videre kun delvist forstået. Et af formålene med projektet har været at foretage et studie af nogle af disse modeller for jordens modstand. Undersøgelsen viste, at modellerne for såvel spids- og sidemodstand er meget forskellige, samt at de alle er empiriske.

SRD-modeller er generelt baserede på regression på mere eller mindre begrænsede datasæt. Det gør dem svære at skalere, svære at sammenligne og usikre for forhold meget forskellige fra de populationer, de er udledt for. Flere af modellerne er baseret på formler for estimering af pæles installerede bæreevne. Dette er ikke nødvendigvis et konservativt mål for modstanden mod ramning. Nogle af modellerne involverer et begreb kaldet *friction fatigue*, hvilket er estimerede formfunktioner for aftagelse i friktionen langs pælens sider efterhånden som afstanden til brudzonen ved spidsen øges.

På baggrund af et litteraturstudie argumenteres for at det populære bølgeligningsprogram GRLWEAP gør nogle forsimplinger vedrørende selve pælen, fordelingen af jordmodstand samt løsningsalgoritme. Modellens præcision er direkte afhængig af en række modelparametre, der definerer bl.a. stivhed og dæmpning. Disse er alle parametre, der basalt set kun kan udledes fra rammejournaler, og som ikke er unikt definerede for konkrete pæl- og jordforhold. Som en kontrast til forsimplingerne og umiddelbart umotiverede valg i pæle- og jordmodel i

GRLWEAP indeholder programmet en stor mængde sofistikerede repræsentationer af en række ramningssystemer.

Mere fysisk troværdige kontinuummekaniske modeller er blevet præsenteret af forskellige forfattere, men disse har alle det til fælles, at de enten er baseret på mere fundamentale jordparametre (hvilke ikke er praktisk mulige at fastslå med tilstrækkelig præcision for de fleste projekter), eller er for komplicerede/dyre at anvende til andet end enkelte hammerslag.

Derfor er et af formålene med projektet at udvikle en dynamisk en-dimensionel model af pæl-jord-hammer systemet, som skal kunne bruges til driveability-analyser, gennem simulering af et nedramningsforløb. Dette skal kunne gøres på baggrund af CPT-målinger alene og med så få bruger-inputs som muligt. Modellen søger at overvinde nogle af de forsimplinger, der anvendes i GRLWEAP ved at behandle pælen som et kontinuum (dog approksimeret med elementmetode), ved at evaluere jordmodstanden i mere end ét punkt per meter og ved at opdatere alle relevante kinematiske variable på lige fod med jordmodstand for hver enkel iteration. Samtidigt lægges der vægt på så simpel en hammermodel som muligt, idet litteraturen antyder at sofistikeret modellering af hammerens faldhøjde, fart mv. ikke forbedrer modellens samlede præcision.

Det vurderes, at modellen må baseres på publicerede modeller for SRD. Disse er stort set udelukkende fremkommet ved brug af GRLWEAP og specifikke værdier af stivheds- og dæmpningsparametre. På grund af manglen på entydighed i disse parametre, og på grund af usikkerheden i evaluering af geomekaniske parametre, argumenteres der for at det ikke er realistisk muligt at udvikle en ny og bedre model for den totale modstand på baggrund af de modeller alene. I stedet adapteres stivheds- og dæmpningsmodellerne fra GRLWEAP til at kunne håndtere en opløsning for evalueringspunkter uafhængig af pælens opløsning, samt med to forskellige sæt opløsninger for løsning af hhv. friktion langs siderne samt spidsen. Der argumenteres for at hvert af disse tre regimer er styret af vidt forskellige karakteristiske længder, og at det derfor ikke giver mening at anvende samme opløsning i dem alle.

En samlet model, der inkorporerer disse betragtninger og som kan anvendes på en vilkårlig geometri og jordforhold er blevet programmeret i MATLAB. Programmet er velegnet til mange lignende beregninger sammenlignet med nuværende proprietære programmer. Programmet anvender en række modelparametre, hvoraf plausible intervaller er fundet på baggrund af litteraturstudier af lignende modeller og vurderinger. En række sensitivitetsanalyser på de involverede modelparametre er herefter udført, hvilket fandt at en relativt grov opløsning af såvel spids- og sidemodstand kan anvendes for relativt ensformige aflejringer, hvorimod særligt opløsningen af spidsmodstand skal være væsentligt højere for jorde med stor variation i styrke. Generelt har modellens numeriske parametre mindre indflydelse på resultatet, men nogle parametre, der kontrollerer lastens form og størrelse, bør kalibreres mod målinger for enkelte hamre.

En applikering af programmet på en case fra Nordsøen viser at det kan anvendes for realistiske situationer, men at det kræver væsentligt længere simuleringstid sammenlignet med GRLWEAP. Det viser sig, at alle jordmodeller ikke kan anvendes direkte i den udviklede model, sandsynligvis pga. for høje statiske modstande i lave dybder. Alm & Hamre modellen er tilsyneladende den mest præcise ud af de undersøgte modeller. De simple SRD-modeller er for upræcise, og det vurderes at disse generelt ikke bør anvendes. De mere omffatende SRD-modeller er i modsætning til forventning ikke nødvendigvis mere præcise.

Preface

This report documents the work done in my tenth semester of studies at Aalborg University. The semester spanned February through June 2017. The thesis is prepared as part of the requirements for obtaining the degree of M.Sc. (*Civilingeniør, cand.polyt.*) through the programme *Structural and Civil Engineering* with the curriculum dated 21 June 2010. The associated appendix report is also part of the project.

I wish to address gratitude towards the supervisors of the project, Lars V. Andersen and Martin U. Østergaard for fruitful supervision and inspiring discussions during the project period.

Prerequisites for reading the report is basic knowledge regarding the AAU Problem Based Learning method, geology, geomechanics and numerical finite element modelling in a technical perspective.

I hereby declare that the work presented is my own in its entirety, and that all sources has been acknowledged and attributed.

Mads H. Harpøth

Reading guide

References to sources are in the form of the Harvard method, with a bibliography in the end of the thesis. References are made for sources with either "[Surname/organisation, Year]" or "Surname/organisation [Year]" and, when relevant, specific pages, tables or figures may be stated. Websites are specified by author, title, URL and download date. Books are specified by author, title, publisher and edition, where available. Papers are furthermore specified with journal, conference papers with time and venue, when available.

The report contains figures and tables, which are enumerated according to the respective chapter. E.g. the first figure in Chapter 4 has number 4.1, the second number 4.2 and so on.

References are made to folders on the enclosures-CD attached to the report, which contains digital files of various kinds. The reference are in the form: "[Enclosures-CD, Folder name]".

The thesis is structured in chapters, and concludes with a discussion of the findings, limitations, and possibilities for future work.

Table of contents

Chapter 1 Introduction and motivation 1

1.1 Offshore wind turbine market . . . 1
1.2 Offshore wind turbine foundations . . . 2
1.3 Installation of monopile structures . . . 4
1.4 Soil variability and associated uncertainty . . . 6
1.5 Objectives of pile driveability analyses . . . 7

Chapter 2 Commonly used methods and scope of project 9

2.1 Energy balance approach . . . 9
2.2 Wave equation analysis in pile driving . . . 12
2.3 Two- and three-dimensional continuum mechanical models . . . 16
2.4 Discussion . . . 16

Chapter 3 Soil resistance models 19

3.1 Common SRD models . . . 20
3.2 Discussion of SRD models . . . 28
3.3 Operational parameters required . . . 34
3.4 Quake and damping . . . 37

Chapter 4 Development of program for pile driving simulation 39

4.1 Pile model . . . 39
4.2 Soil resistance model . . . 45
4.3 Hammer model . . . 54
4.4 Transient algorithm . . . 62
4.5 Summary and discussion . . . 68

Chapter 5 Convergence and sensitivity studies 70

5.1 Test programme configuration . . . 70
5.2 Summary of convergence and sensitivity studies . . . 73

Chapter 6 Back-calculation of pile driven in North Sea sand 76

6.1 Soil conditions . . . 76
6.2 Available information about the driving . . . 78
6.3 Configuration of model . . . 79
6.4 Results and discussion . . . 81

Chapter 7 Conclusion and future work 88

List of symbols 96

References 96

Appendix A Estimating unit weight, soil type and friction angle from CPT A1

A.1 Unit weight and soil type . . . A1

A.2 Effective friction angle A1

Appendix B Newton-Raphson iterative scheme A4

Appendix C Incremental numerical integration by the Newmark-β method A6

Appendix D Derivation of modified Bathe composite scheme A10

D.1 First substep A10

D.2 Second substep A12

Appendix E Enclosed set of scripts A14

Appendix F Results of convergence and sensitivity studies A16

F.1 Case (a) - Constant q_c and δ A16

F.2 Case (b) - Linearly varying q_c and δ A23

F.3 Case (c) - Single, much stronger layer A26

F.4 Case (d) - Numerical model parameters A29

F.5 Case (e) - Load parameters and structural damping A36

1. Introduction and motivation

Since the beginning of manufacturing of large wind turbines after the oil crisis in the 1970s and several technological breakthroughs in the 1980s, the competition on the wind turbine market has been fierce. In the latter years onshore wind energy has become economically competitive compared to conventional sources of electricity, but a gap still exists with regards to turbines installed offshore.

1.1 Offshore wind turbine market

Loads on offshore turbines are more extreme, construction and maintenance costs are higher and the down-time in case of breakdown is most likely longer compared to onshore turbines. In order to reduce noise and other environmental impacts on humans and also to utilize areas with higher and more consistent wind speeds, an increased interest in offshore wind turbines from the public has prevailed in recent years, mainly in Europe.

The average rated capacity of installed offshore wind turbines has increased by 62% in the last decade [WindEurope, 2017], with the most recent additions being +8 MW turbines totalling more than 200 m in height [MHI Vestas, 2016]. An overview of the installed offshore capacity in Europe during recent years can be seen in Figure 1.1. Despite the heavy competition, offshore wind energy is still substantially more expensive than onshore alternatives, with IRENA [2012] stating that typical capital costs amounts to at least twice that of onshore turbines. The levelized cost of energy (LCOE) can in some cases be competitive against onshore turbines due to the higher capacity factor offshore. In order to meet the goal of better competitiveness in the open energy market the construction costs has to be lowered.

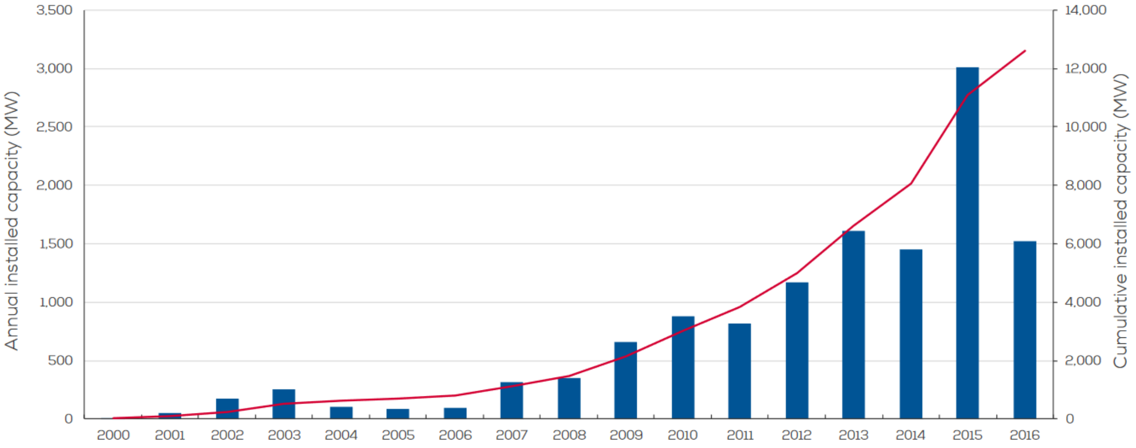

Figure 1.1. Annual and accumulated installed offshore wind turbine capacity in Europe. From WindEurope [2017].

The International Energy Agency has stated that the expected electricity demand of the world is due to increase by 70% by 2040 [IEA, 2016], and that 40% of the necessary increased capacity will most likely consist of wind turbines, mostly onshore. The offshore wind energy market is due to increased population density in emerging economies expected to increase somewhat.

IEA [2016] recognises the main reasons for the lower profitability of offshore wind turbines as being the larger costs of foundations and installation when compared to onshore turbines. IRENA [2012] states that less than half of the cost of an offshore wind turbine is the turbine itself, and up to 30% or more can be attributed to foundations and installation.

As offshore wind turbines have become larger and more common, a trend toward installing the turbines in larger and larger wind farms is emerging - in order to save costs on secondary facilities, power transport and construction. Before 2009, the average offshore wind farm capacity in Europe was less than 100 MW, in 2013 it surpassed 400 MW and it is now expected (according to WindEurope [2017]) to increase to more than 1 GW on average. The majority of installed turbines has a capacity of approximately 4 MW, meaning that an average offshore wind farm in the future could consist of more than 200 typically identical superstructures.

This up-scaling of projects, along with the general increased competition, means that the offshore wind farm projects are becoming more economically sensitive to disruptions in the construction phase, as the margins for error become smaller. Douglas-Westwood [2010] states that the specialised vessels used for construction of offshore wind turbines have a typical day rate of 120 000 EUR, meaning that any delay in construction can mean severe budget overruns. The largest offshore wind developers are focusing their investments on fewer, larger and more profitable projects - and accurate and effortless prediction of the time and resources needed for construction of many similar turbines is thus of paramount importance.

1.2 Offshore wind turbine foundations

This section serves to give a brief overview of the typical substructures and foundations used for offshore wind turbines. Several foundation methods for offshore wind turbines exists, of which a selection is:

Large-diameter tubular steel piles (*monopiles*) driven or otherwise brought to depths of 20-70 m or more. This is by far the most common type of offshore wind turbine foundation. As substructure, transition pieces (almost exclusively in steel) is placed and grouted on these steel piles, typically covering most of the pile length above ground. The transition piece accounts for non-perfect verticality of the pile, provides mounting points for the tower and carry various installations. The monopile has proven to be comparatively cost-efficient, especially in shallow waters. The drawback is the transversal flexibility of the structure, and for greater water depths two problems arise: Extensive design efforts to avoid resonance with typical wave frequencies is needed, and the pile length, diameter and thickness below ground increases, which then poses a problem regarding dynamic performance and weight. A sketch of the set-up can be seen in Figure 1.2. The vertical resistance stems from side friction and the end bearing.

Gravity base concrete structures have been used for some near-shore projects, as they do not experience the flexibility issues associated with monopiles. The structure consists of a cylindrical or conical section terminating in a large plate-type structure typically at sea bed level or slightly below. They are relatively cost-efficient for shallow waters and friction soils, but require some ground preparation before installation, they are not suitable for weak or easily compressible soils because of differential settlements and they require large production facilities.

Tripod and jacket structures consists of tubular steel structures, which are towed to sea and founded on smaller-diameter typically tubular steel piles. This technology is common in the oil & gas industry and is horizontally stiffer compared to the monopile, but requires more pile driving.

Suction bucket or suction caissons is a newer approach, used in place of the below-ground part of a foundation. It is installed using water jets generating low pressure within a "turned-up bucket". The low pressure drags the caisson to the bottom, and once installed, it acts as gravity-base foundation. The method has advantages regarding installation costs, noise, versatility and decommissioning costs, and can be used directly in place of monopiles or smaller diameter piles, but has not yet been widely applied.

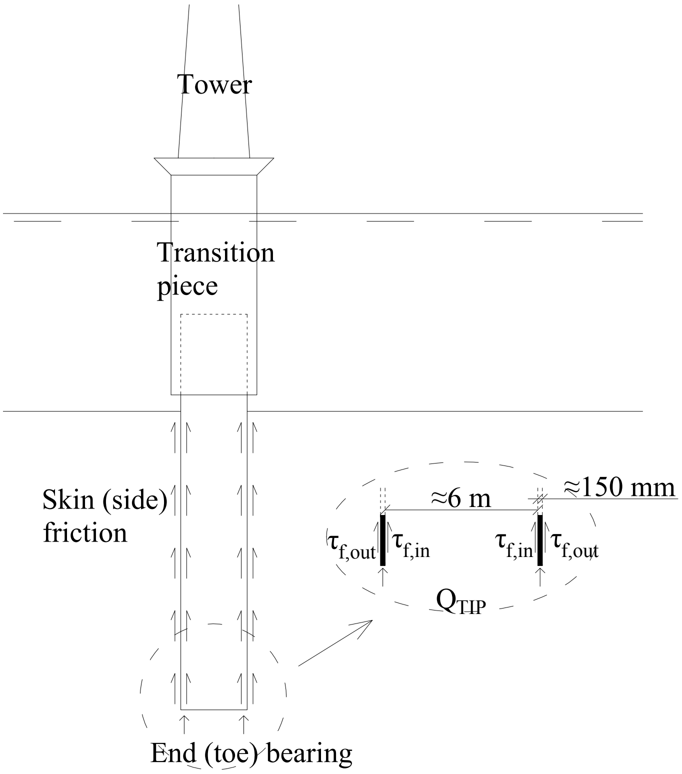

Figure 1.2. Sketch of typical monopile substructure system for a large offshore wind turbine.

According to WindEurope [2017], the majority (88%) of offshore wind turbines installed in 2016 utilizes the monopile/transition piece structure as the foundation/substructure. Hence, the focus of this project is solely the monopile-type substructure. The most common way of manufacturing monopiles is by rolling and welding large steel plates. The monopiles is then either transported by barge, supply ship or simply plugged and floated to the installation site, either in large segments or whole (most common).

1.3 Installation of monopile structures

Heavy-lift cranes such as HLV Svanen (see Figure 1.3) or specialised jack-up vessels for sites with severe wave climate is then used for positioning the pile and as hoist for necessary equipment.

Figure 1.3. Picture of heavy-lift vessel Svanen. Provided through Wikimedia Commons.

Various methods for installation of monopiles exist:

- Hammer driving using various impact hammer types including drop hammers or power assisted drop hammers using either steam, gas, diesel or hydraulic pressure as power source. The pile is hoisted in place and the weight of the pile alone brings the pile the first short distance down until equilibrium with the soil resistance is reached. Hereafter ramming is initiated with a typical frequency of $\approx 0.5 - 1.0\,\mathrm{Hz}$. The individual impacts accelerate the pile top and generate a stress wave, which travels through the pile at the speed of sound in steel. The wave front generates a normal strain, which through adhesion is partially transmitted to the surrounding soil eventually overcoming the soil shear strength at the pile sides and invoking a complex zone of complete yielding at the pile tip. The inertial force of the accelerated pile is then much larger than the plastic limit of the soil, and the pile is displaced until equilibrium is reached again. The drawback of the method is the typically large weight of the structure in order to avoid buckling of particularly the lower part of the pile or excessive fatigue damage during driving.
- Drilling (or micro-tunnelling) involves lowering a drill (essentially a small tunnel drill), which drills a hole in which the pile is continuously lowered into. The method is advantageous if special noise or weight restrictions apply, or if the soil resistance is expected to be very large (e.g. chalk or rock). The drawbacks are increased installation time and more complex and expensive equipment needed. Can involve grouting if drilling in e.g. rock.
- Jacking is a static method, in which a hydraulic jack can be used to simply press the pile down to desired depth. Can only be used for weak soils and is almost never used offshore as enormous counterweight is needed, which is not practical in offshore applications.
- Vibration is the mounting of a vibrator to the pile top, which creates pulses of much higher frequency as compared to hammers. The vibrator creates side slip due to Poisson effect and downward motion of the stress waves along the shaft, which lowers the side friction in

order to drive the pile an amount. The method can be applied to stiffer soils and with less counterweight compared to jacking.

- Combinations of the aforementioned methods is also possible, of which the most common is the vibratory hammer and vibratory jack.

The present project is concerned with installation using impact hammers, as it is the most common installation method for large-diameter monopiles.

Most large monopiles exhibit purely or partially coring behaviour during driving, meaning that no "plug" will form, and only the net area of the pile toe will contribute to the end bearing capacity of the pile. Some soil conditions will invoke plugging of the monopile during ramming, which will increase the soil resistance greatly. This is not common in most North Sea soil types, but little research exist on special conditions, e.g. large monopiles in chalk. Gudavalli et al. [2013] investigated plugging of piles of a smaller diameter in dense to very dense sands. For a 914 mm diameter pile they found a plug length to pile length ratio of 0.91 (fully coring is 1.00), which suggests that a pile with a diameter at least four times larger will not plug.

1.3.1 Hammer pile driving systems

Early pile driving equipment simply consisted of winched drop hammers. Modern hammer/driver types in existence include (hammer efficiency e_h as suggested by Pile Dynamics [2010] in parenthesis):

- Hydraulic impact hammers (0.80-0.95)
- Diesel impact hammers (0.80)
- Air/steam impact hammers (0.50-0.80)
- Vibratory pile drivers/hammers (1.0)

The reason for the high efficiency of the vibratory hammers is probably due to the fact that they are most commonly mounted rigidly to the pile. The vibratory hammer is essentially a lower-frequency vibratory jack with a much heavier set of rotating weights. The diesel, air and steam hammers uses combustion, air pressure or steam, respectively, to either lift (single-acting) or both lift and accelerate the ram (double-acting). According to Seaway Heavy Lifting [2009], the almost exclusively used hammer is the hydraulic type. This system can be modelled in a number of ways. In this project, force-time series will be used. This force series must thus represent any losses in the hammer system.

A sketch of the rest of the principal energetic system of pile driving can be seen in Figure 1.4.

A number of various add-ons between the hammer and the pile top can be used, depending on situation. This includes:

- Pile helmet/anvil usually made of steel
- Pile cushion. Not used for hydraulic hammers.
- Driving head. Integral, strengthened top part of the pile used for high pile stress situations.
- Followers (tube bolted to the pile or attached to installation vessel), which are used when driving directly on the pile top is not possible. Rarely used for monopiles as hydraulic hammers can operate underwater, but common when applying piling templates for e.g. jacket structures.

The energy loss in these add-ons must be considered directly or indirectly through loss factors in any simulation of pile driving.

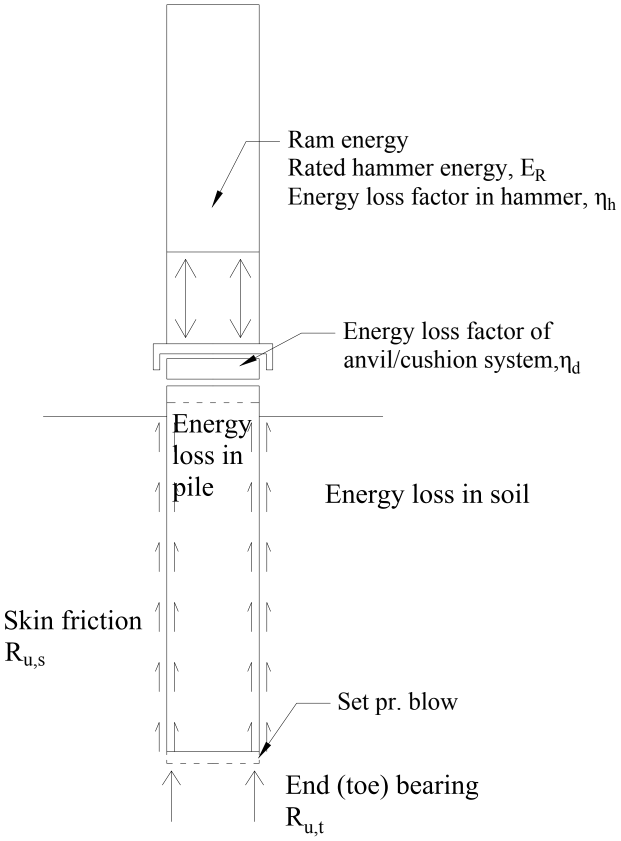

Figure 1.4. Sketch of the principle of pile driving, with main energy balance contributors shown.

1.4 Soil variability and associated uncertainty

The quality of capacity predictions and pile driving simulations depend largely on the availability of high-quality local geotechnical data and possibly local correlations to strength and stiffness parameters. The usual scope of geotechnical investigations in relation to an offshore wind farm is:

- Investigation of literature, geotechnical surveys, reports from nearby sites etc. in order to determine expected types of soil and deposition age
- Boreholes with the purpose of establishing an overall soil classification and stratigraphy for the farm and for taking out intact samples of soil, used in laboratory tests for relatively accurate but expensive determination of in-situ properties
- Numerous CPT's (almost always one per pile), which can give good local estimates on stratigraphy and properties. Usual resolution of CPT data is 2 cm, which in nearly all practical applications can be regarded as continuous. Varying apparatus exist, but the most commonly used equipment measures sleeve friction f_s, cone tip resistance q_c and pore pressure behind the cone u_2 (see e.g. Lunne et al. [1997, Figure 3.1]).

Because soil is a natural material, large variabilities occur. Spatially, continuity/clarity of stratigraphy, essential strength, stiffness and hardening parameters, unit weight and more can vary significantly. It is not commonly possible to obtain completely accurate fundamental soil properties, due to the large variation and the empirical nature of relations between CPT data and most soil properties.

In some cases upper confidence bounds on even basic properties can be several hundred percent larger than the lower bounds, and large partial safety factors are used. Furthermore, most relevant quantities for material modelling can fundamentally not be estimated from CPT investigation. Some special phenomena, essentially involving transient, rapid changes and non-linearities are not fully understood and can thus not be modelled accurately.

In well-defined materials and interfaces fully three-dimensional FEA and sophisticated continuum mechanical models are commonly applied and yields high quality results. Due to the mentioned uncertainties, very sophisticated material models of the pile-soil interface seems unjustifiable, as the added complexity will increase design costs without necessarily decreasing result uncertainty. It is essential that any model of the pile-soil interface is somewhat simple but still as physically sound as possible. Preferably, a material model of the pile-soil interface is calibrated with only a few parameters, so as to ensure fast computation with the aim of not having to simplify soil stratigraphy and behaviour.

Because of the usual abundance of CPT data, direct correlation between these data and pile driveability simulations is preferred. Relating CPT data and pile resistance usually also has the advantage of less uncertainty on the soil properties applied in the simulations and easier automation.

1.5 Objectives of pile driveability analyses

As previously mentioned, the accurate prediction of pile driving is key for a successful installation of offshore wind farms. This is due to a number of complications involved in pile driving, chiefly:

- Most soils will remould and loose strength when driving, but creep or similar occurs hereafter and the strength will thus increase over time. It is preferable to perform as much of the driving as possible in a single run in order to reduce driving time and energy consumption, and changes of hammer need to be avoided.
- Most specialised barges, jack-up vessels etc. have low availability and limited tolerable sea states, limiting their window of operation.
- Breakdowns or damages to piles can in most cases only be repaired in a matter of days/weeks and must therefore be avoided.
- Under-dimensioning of driving system can result in too low penetration and ultimate bearing capacity, leading to expensive remedial work.

The point where the driving system is unable to drive a pile further is called pile refusal. Pile refusal is often specified as a given blowcount, where blowcount is defined as blows/m. The risk of pile refusal must be avoided, as Seaway Heavy Lifting [2009] estimates that the overall installation duration can double or triple due to associated delays. Generally, the risk of refusal obviously increases with soil strength, overburden stress levels or when the soils contains boulders, cemented layers, chalk etc.

Contractors sometime increase pile wall thickness in order to quickly being able to use larger hammers and avoid refusal, which is not only wasteful regarding material, but may also increase the toe resistance to driving. This can be overcome by installing an often cone-shaped pile shoe.

The purpose of a pile driveability analysis is to:

- Establish a relation (simulation) of pile penetration per hammer blow to determine the ability of the hammer to drive to target penetration
- Assess stresses induced on pile during driving, to ensure no damage to especially the pile top and to avoid fatigue

The following chapter contains a review of some methods for doing this analysis, discusses the findings and concludes with a statement of intent of this project.

2. Commonly used methods and scope of project

The purpose of this chapter is to discuss methods for pile driving simulation applied today, identify key problems and finally state the intent and scope of the present project.

Prediction of pile driving can broadly be classified into:

- Energy balance equations. These are the simplest and least accurate methods.
- Numerical solution of the one-dimensional wave equation within the pile domain (finite difference, finite element or equivalent) with soil modelled as a simple spring-dashpot (Kelvin) system, essentially due to the model by Smith [1960] with later refinements.
- Transient two-dimensional axisymmetric or full three-dimensional finite element models of both pile and soil domain using estimates of strength, stiffness and other parameters. These methods generally use the finite element method, some employing standard Lagrangian descriptions and some coupled Eulerian-Lagrangian formulations.

2.1 Energy balance approach

Many engineers have in the past attempted to obtain a rational, easy way of determining the resistance to driving of piles. The only directly available data during driving was, and to some extent is:

- Fundamental properties such as pile length, material, diameter, wall thickness, weight etc.
- Equipment mounted to pile tip or pile head, e.g. driving shoe, pile cap or driving head, anvil, cushion etc.
- Weight and drop height
- Number of blows per permanent set s

Naturally, attempts have been made to relate the energy available to driving (i.e. net hammer energy) to the pile resistance or capacity, as it was expected that the resistance to driving is closely connected to the ultimate capacity of the pile. Referring to Figure 1.4, the basic energy balance in dynamic pile driving can be derived:

$$\begin{aligned}&\text{Impact energy} = \text{Work done} + \text{Losses}\\ &\qquad \eta_h \eta_d E_R = R_u s + E_P + E_s \qquad (2.1)\\ &\qquad \eta_h \eta_d E_R = R_u s + R_u k_P + R_u k_s\end{aligned}$$

where

η_h	Hammer loss factor
η_d	Driving system loss factor
E_R	Rated hammer energy
R_u	Soil resistance, $R_u = R_{u,s} + R_{u,t}$

s	Permanent set pr. blow
E_P	Energy loss in pile
E_s	Energy loss in soil
k_P	Model pile spring stiffness
k_s	Model soil spring stiffness
$R_{u,s}$	Side friction
$R_{u,t}$	Tip resistance

After each blow, the pile system must eventually reach an equillibrium state, which is the idea behind the equation. For the hydraulic hammer, the actual net hammer energy $\eta_h E_R$ is often precisely monitored. Theoretically, if R_u, $\eta_h \eta_d E_R$, E_P and E_s is known, it should then be possible to calculate the permanent set (or penetration) of the pile. It is however not easy to calculate the losses in pile and soil, and can only be estimated if not simulated numerically. Most often the pile material behaviour is assumed purely elastic.

The energy losses in soil and soil resistance is fundamentally a non-linear problem because of the large plastic deformations involved in failure of soil. By introducing linear spring stiffness approximations, the problem becomes computationally easy to manage, but the real soil behaviour is then obviously only indirectly modelled.

Many formulas of the energy-balance type has been derived in the past, using various simplifications (principally regarding estimation of the losses) and/or calibration factors. Pile driving equations of the energy balance type is often called dynamic formulas. For just a few of the particular variations see e.g. Gates [1957], Olson and Flaate [1967], Ovesen et al. [2012] and Hannigan et al. [2016].

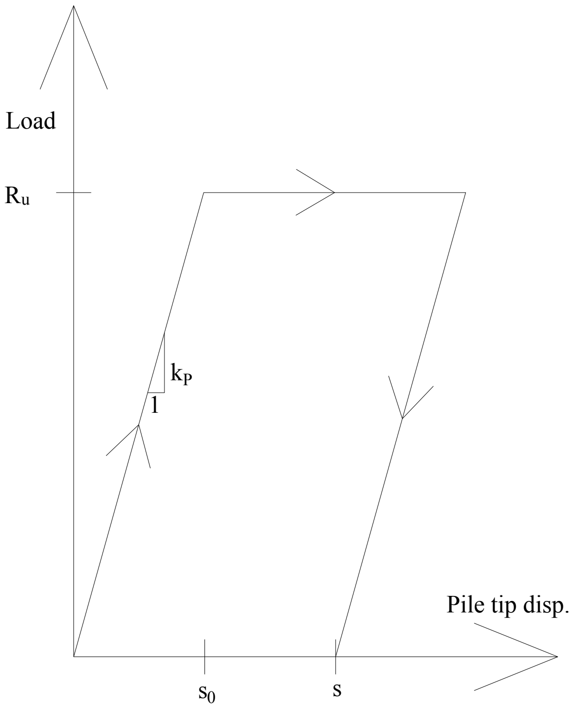

Figure 2.1. Assumed elastic-perfectly plastic load-settlement curve in the "Danish formula" for dynamic pile capacity. s is the plastic soil deformation, s_0 is the elastic pile compression.

The formula sometimes called the "Danish formula" [Sørensen and Hansen, 1957] proposes a very simplified relation between the permanent set and the capacity of the pile. The load-settlement curve assumed in this equation is seen in Figure 2.1. By ignoring soil losses and simply stating that the ram energy minus the work done in compression of the pile is equal to the work done by plastically deforming the soil, it is possible to state:

$$\begin{aligned} \eta_h \eta_d E_R &= R_u s + \frac{1}{2} R_u s_0 \\ k_P s_0 &= R_u \Rightarrow s_0 = \frac{R_u L_P}{A_P E} \end{aligned} \tag{2.2}$$

where

s_0	Elastic pile deformation
L_P	Pile length
A_P	Cross-sectional area of pile
E	Young's modulus of pile material

Assuming $s = 0$ and thus obtaining s_0, the equation can be simplified to:

$$R_u = \frac{\eta_h \eta_d E_R}{s + \sqrt{\dfrac{\eta_h \eta_d E_R L_P}{2 E A_P}}} \tag{2.3}$$

This approach is obviously very simplified, and is best suited for quick calculations, preferably based on driving records. The initial intent of the energy formulas were also simply estimates on pile capacity, not driveability.

Hannigan et al. [2016] discusses the accuracy and validity of dynamic formulas in general, and finds that large variations in reliability exist. The basic problems with the formulas are:

- In reality, the pile inertia is not concentrated and the system does not compress uniformly like a spring. The energy is transferred through viscoelastic stress wave propagation from the hammer through the pile to the tip and back.
- The formulas assume constant, instantaneous soil resistance independent on load and, more importantly, load rate. The load rate has a large impact on a) the reduction of strength due to remoulding in especially clays, and b) the increase in tip resistance due to build-up of pore pressures. The errors due to disregarding the load rate is however smaller in sandy deposits, but still significant.
- They are not related to any fundamental soil properties and thus requires knowledge about local R_u, which depend on e.g. assumed failure criteria, stiffness and other fundamental properties, which varies.
- Lack of adequate modelling of energy losses in the driving system
- Assumes no energy losses in soil due to elastic deformation, friction, pore pressure dissipation etc.

Because of the high risks of refusal when choosing too small a hammer, and risk of pile buckling when choosing a too large hammer, it is essential that the set per blow predictions are accurate, especially for offshore applications. Therefore, the effort of using more sophisticated methods can be justified, and the energy formulas are thus not used offshore.

2.2 Wave equation analysis in pile driving

The wave equation approach is adopted by most commercial and practically used software, including the GRLWEAP [Pile Dynamics, 2010] program, as experience shows that sufficient accuracy can be achieved through extensive calibration performed in the last decades.

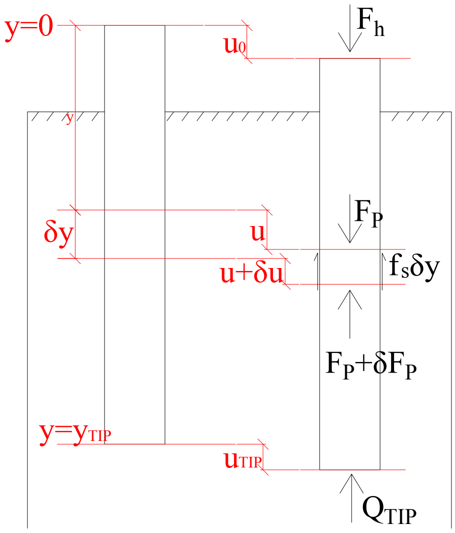

Figure 2.2. Diagram for derivation of the pile wave equation.

Consider an infinitesimal pile element with top coordinate y seen in Figure 2.2, subjected to a hammer force F_H. The element is subjected to a displacement u when the hammer impacts, and will furthermore have a varying velocity $v = \dfrac{\partial u}{\partial t}$ and acceleration $a = \dfrac{\partial^2 u}{\partial t^2}$. If the pile moves slowly, the problem is dominated by the *static resistance to driving* (SRD), and if the movements are rapid, the problem is dominated by soil "damping".

By assuming elasticity, the strain, stress and force acting on the element can be written as (taking $\lim_{\delta \to 0}$):

$$\varepsilon = \frac{\partial u}{\partial y} \quad , \quad \sigma = E\frac{\partial u}{\partial y} \quad , \quad F_P = EA_P\frac{\partial u}{\partial y} \tag{2.4}$$

Where the force F_P can be called the static impact force. An inertia force also develops, described by:

$$\delta F_P = \rho_P A_P \delta y \frac{\partial^2 u}{\partial t^2} - f_s \delta y \quad \Rightarrow \quad \frac{\partial F_P}{\partial y} = \rho_P A_P \frac{\partial^2 u}{\partial t^2} - R \tag{2.5}$$

where

ρ_P	Mass density of pile
f_s	Unit skin friction on pile
R	Soil resistance

Equations (2.4) and (2.5) can be equated and rewritten as:

$$\frac{\partial^2 u}{\partial y^2} = \frac{\rho_P}{E}\frac{\partial^2 u}{\partial t^2} - \frac{R}{EA_P} \quad \text{or} \quad \frac{\partial^2 u}{\partial y^2} = \frac{1}{c_0^2}\frac{\partial^2 u}{\partial t^2} - \frac{R}{EA_P} \tag{2.6}$$

where

c_0	Isotropic elastic wave phase velocity $c_0 = \sqrt{\frac{E}{\rho_P}}$

Naturally, stress waves can reflect at the pile end, and will thus propagate upwards. The phase velocity will be approximately $\sqrt{\frac{2 \cdot 10^{11}\,\mathrm{Pa}}{7850\,\mathrm{kg/m^3}}} \approx 5000\,\mathrm{m/s}$, and thus the complete travel time for the stress wave from the top to the bottom and back will be in the order of 10 ms. For a more rigorous and general three-dimensional treatment of wave propagation in an elastic continuum, please refer to Andersen [2006]. Equation (2.6) in its simplest form is identified as a linear partial differential equation, and may be solved by e.g. separation of variables [Kreyszig et al., 2011] if critical simplifications about the distribution of the soil resistance R (i.e. no stratification and no end bearing) are made or, more applicable to realistic situations, by numerical methods.

2.2.1 Smith model

Smith [1960] proposed a lumped mass model with a finite difference solution scheme. A schematic of the proposed mass/stiffness/damping model can be seen in Figure 2.3.

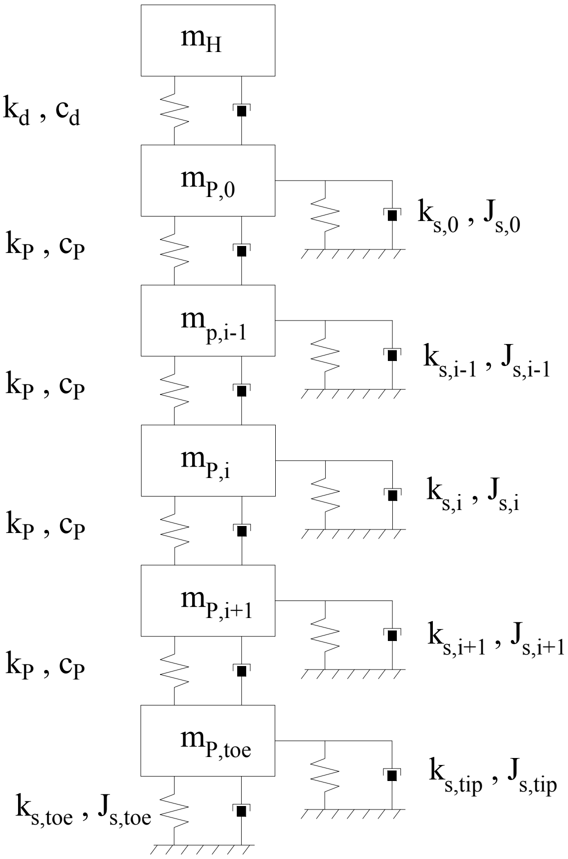

Figure 2.3. Lumped-mass Smith model employing spring-dashpot (Kelvin) systems representing pile material and soil stiffness and damping, for solution of Equation (2.6).

The pile mass is lumped in a number of positions along the pile, between which the material stiffness and damping are modelled as a spring-dashpot system.

The "stiffness" and "damping" of the soil is modelled using a completely analogous spring-dashpot system, also lumped along the length. The spring stiffness is obtained via the simple linearly elastic-perfectly plastic relation seen in Figure 2.1, where $R_{u,i} = R_{s,i}$ and a *quake* q_i (assumed elastic deformation of soil) is used for defining the soil spring stiffness $k_{s,i}$. The static resistance to driving at a given displacement of an element is thus:

$$\begin{aligned} R_{s,i} = \left(\frac{u_i}{q_i}\right) R_{u,i} = k_{s,i} R_{u,i} \qquad &\text{for} \qquad u_i \leq q_i \\ R_{s,i} = R_{u,i} \qquad &\text{for} \qquad u_i > q_i \end{aligned} \tag{2.7}$$

The resistance contribution from soil "damping" and the damping coefficient $J_{s,i}$ are assumed proportional to the static resistance as well:

$$R_{d,i} = R_{s,i} J_{s,i} v_i^n \tag{2.8}$$

where

$J_{s,i}$	Smith damping coefficient [s/m]
n	Damping exponent [-]

This soil "damping" model is identical to the one first suggested by Smith [1960], and has later been advocated by, among others, Litkouhi and Poskitt [1980], Heerema [1979] and Heerema [1981]. Experiments by e.g. Litkouhi and Poskitt [1980] suggests that the exponent should be 0.2. However, the recommendations of Pile Dynamics [2010] of $n = 1.0$ and $J_{s,i}$ depending on soil type is often used instead.

A very simplified model of the radiation damping phenomenon, which can contribute to resistance in pile driving as shown by Meynard and Corte [1984], is included in GRLWEAP (albeit Pile Dynamics [2010] strongly discourages it).

A review of some soil resistance models can be found in Chapter 3.

Smith [1960] proposed a quite crude finite difference scheme for solving the system. Later, a semi-implicit time-marching predictor-corrector algorithm, which is widely applied, i.e. in GRLWEAP [Pile Dynamics, 2010] were developed. The initial condition of the simulation for each blow is the hammer drop velocity. The time increment is determined according to:

$$\Delta t = \frac{\min\left(\Delta t_{cri,i}\right)}{\phi} \quad , \quad \Delta t_{cri,i} = \frac{L_i}{c_{p,i}} \quad , \quad c_{p,i} = \sqrt{\frac{E_i}{\rho_i}} \tag{2.9}$$

where

$1/\phi$	Courant number, default = 0.625
L_i	Element length
$c_{p,i}$	Wave speed assuming only P-waves

The algorithm applied in GRLWEAP consists of the following finite difference scheme (referring to Figure 2.3, i.e. lumped mass, and superscript indicating time step):

1. *Predictor* displacements and velocities are obtained as

   $$u_i^n = u_i^{n-1} + v_i^{n-1}\Delta t$$

   and

   $$v_i^n = v_i^{n-1} + a_i^{n-1}\Delta t$$

   where Δt is time increment and the scheme is marching, such that the initial condition of the first element (a "hammer" element) is the hammer velocity.
2. A spring and damping force between each mass is calculated as $F_i = k_i\left(u_i^n - u_{i-1}^n\right) + c_i\left(v_i^n - v_{i-1}^n\right)$ where k_i is the material stiffness of a pile, hammer or anvil element and c_i is the ditto damping. The superscript refers to time step number.
3. The soil resistance R_i is calculated using the **predictor** displacement and velocity at the position of the masses. It is unclear how the smaller resolution of CPT measurements versus the larger resolution elements is handled by the program. It is likely that the element displacement and velocity is assumed constant $\pm L_e/2$ from each node where L_e is the distance between nodes, where after the soil resistances (dependent on displacement and velocity) are calculated, averaged and used for the spring-dashpot calculation.
4. Using the equation of motion, the acceleration at the current time step is then found as:

   $$a_i^n = g + \left(\Delta F_i^n - \Delta R_i^n\right)\frac{1}{m_i}$$

   where g is the gravitational acceleration, ΔF_i^n is the difference in top and bottom (nodes) internal force, ΔR_i^n is the difference in top and bottom soil resistance and m_i is the element mass.
5. A *corrector* integration is performed assuming linearly varying acceleration:

   $$v_i^n = v_i^{n-1} + \left(a_i^n + a_i^{n-1}\right)\frac{\Delta t}{2}$$

   and

   $$u_i^n = u_i^{n-1} + v_i^{n-1}\Delta t + \left(2a_i^{n-1} + a_i^n\right)\frac{\Delta t^2}{6}$$

   This is iteratively used to re-evaluate the internal forces (but curiously not the soil resistance) and the iteration continues until convergence is obtained.
6. Goes to next time step.

The pile penetration is updated in the end of each step of the time-marching scheme using the permanent set, which in GRLWEAP is estimated according to Equation (2.10). There is no explanation in Pile Dynamics [2010] to why this approach has been adopted instead of just using the toe displacement at the end of each complete wave-down and wave-up cycle as the set per blow, but historical assumptions (i.e. the customary energy balance equations) might be the reason.

$$s = u_{max,t} - q_{ave} \quad , \quad q_{ave} = \frac{\sum R_{u,i} q_i}{R_{u,tot}} \tag{2.10}$$

where

$u_{max,t}$	Maximum toe displacement in step
q_{ave}	Average quake
$R_{u,i}$	Individual resistance of each element
$R_{u,tot}$	Total capacity

2.3 Two- and three-dimensional continuum mechanical models

Extensive research in the dynamics of pile driving has been conducted, most intensively in approximately the last 30 years. The predominant tool for numerical analyses has been the Smith model described in the previous sections. Various authors, including [Deeks, 1992] and [Masouleh and Fakharian, 2007], have published models of axisymmetrical simulations of pile driving or installed piles subjected to dynamic loading.

Most of the published results have utilised self-developed finite element models, boundary element models or similar. In later years commercial software has to various extents been applied, like the Plaxis software [Plaxis, 2017] and more general FEA packages like Abaqus [Dassault Systèmes, 2017].

The chief advantages of these more sophisticated models is the possibility of using more fundamental soil properties and material models, and to actually model the stress state, thus limiting geometrical, site-specific and other bias effects on the pile-soil interface shear strength. Furthermore, the ability of accurately modelling wave propagation in the surrounding soil makes incorporation of radiation damping in a reasonably physical way possible. The disadvantages are naturally the extensive computation and preparation effort, effectively limiting this more scientific approach to research use only. More critically, it is seldom possible to obtain fundamental in-situ soil properties with sufficient accuracy, which are required.

2.4 Discussion

The one-dimensional wave equation approach is still the most common driveability prediction method in use today, through the widespread use of the GRLWEAP program. It has achieved this position due to reasonable accuracy, ease of use and many improvements and driving system model refinements over the past 40 years. The model has been so extensively calibrated, mostly through published SRD relations, that accurate results can be achieved for most standard situations.

It seems as though a focus of the developer of GRLWEAP seems to be very accurate modelling of the driving system, where many sophisticated hammer models are included in the program as a contrast to few, crude soil models. These models are included even though several studies, including Middendorp and van Weele [1986], has shown that precise modelling of the actual hammer geometry, real drop velocity, physical anvil stiffness etc. is not necessary for representing the force-time response of the driving system accurately.

The numerical implementation of the Smith model in GRLWEAP can also be questioned. If no simplifications regarding transient values of soil resistance is made and because of the lumping, the solution methods are limited to explicit integration, with potentially very small time steps [Borja, 1988]. Because of this, GRLWEAP makes approximations to the soil resistance at a given solution step and iterates (while only changing some of the kinematic variables) until convergence.

The initial condition of the simulation for each blow is the hammer drop velocity. Borja [1988] states that the impact force is better described by a force-time series. Describing the entire response at the pile head by a fixed force series alone as done in Borja [1988] is however not entirely accurate, as the inertia and impedance of the hammer itself can not be included explicitly in an easy way.

The Smith model has some inherent shortcomings, chiefly the empirical nature of how the pile-soil interaction is modelled [Deeks, 1992]. The reaction of the soil to the pile motion is not based on fundamental analysis of the behaviour of remoulded, dynamic soil. The static resistance can to some extent be related to fundamental soil mechanics and local calibration through the advent of CPT measurements, but the quake and damping are purely based on experience and convenience, and it is in essence not possible to obtain these parameters from standard experiments. It is however questionable whether it is possible to relate driveability and fundamental soil properties without greatly increasing model complexity (i.e. making at least a two-dimensional, continuum mechanical model), amount of model preparation and resolving time, which all are key issues for any economically viable pile driving simulation.

The proportionality between static resistance and damping does not necessarily have any theoretical merit, but some authors (e.g. Deeks [1992]) states that this connection is convenient and can give good results for proper choice of J and normal (i.e. normal load rate) conditions. Uncertainty and in some cases lack of empirical data (e.g. for unusual pile dimensions or soil conditions) in both the static resistance, the quake and the Smith damping coefficient is a major concern when simulating pile driving. The values of these parameters can fundamentally only be found through back-calculation of driving records, and is thus dependent on specific conditions like hammer energy, pile wall thickness and diameter, local variations in soil strength and stiffness, deposition age and also depth, which makes accurate predictions a question of qualified guessing.

Using a damping exponent = 1 seems unreasonable in nature, as studies have shown that the soil viscosity is dependent on strain rate. Specifically, Litkouhi and Poskitt [1980] found a non-linear dependency between the damping and velocity. This has also been recognised by the authors of the program [Randolph and Simons, 1986], but is however not recommended according to Pile Dynamics [2010].

Pile Dynamics [2010] states that the element length is chosen by the program as approximately 1 m, over which the resistance values (both dynamic and static) are calculated according to the previous time step (even though they depend on the actual pile velocity and displacement) and without variation of displacement and velocity along this length. The numerical treatment of the distribution of resistance along the pile is ambiguously described in Pile Dynamics [2010], but the resistance distributions are at least based on the type of soil input provided, e.g. CPT. A more accurate approach could be to interpolate the displacement and velocities in relatively high resolution along the pile at the current iteration step (not the previous), calculate local resistances, integrate numerically and obtain a more consistent and physically appropriate resistance distribution.

2.4.1 Statement of intent

The existing software (GRLWEAP) is fast and commonly used. As discussed above, assumptions regarding the dynamic soil resistance and the distribution hereof, especially lack of dependence on local displacement and velocity along the pile seems unreasonable. The precision of the program depends on the SRD model applied, which to some extent must be based on experience and back-calculation. This is not a problem for "normal" structures, for which extensive data and published SRD models exist. For more unusual structures, much more emphasis must be put on obtaining appropriate SRD models.

More sophisticated pile driving models have been attempted in the past, mainly axisymmetric FE-models of the pile and immediately surrounding soil with varying success rates, but they rely on fundamental soil properties which are either expensive to obtain or uncertain, making these models impractical and/or no more precise than the simpler models.

The goal of the present project is to

- Review a selection of existing SRD models
- Incorporate and modify existing experience in the form of SRD models in a 1-D dynamic finite element model of the pile-soil-hammer system simulating the driving situation
    - The model should treat the interface between the pile and soil in a more direct and explicit manner within each time step, thus being able to more accurately model the correct soil resistance
    - The hammer impact should be modelled numerically and dependent on pile head response
    - The model should be fast enough for practical use and must be structured in a way so that only minimal user input is required, while aiming for higher precision compared to existing models
    - The soil input parameters must be limited to those easily obtainable through CPT measurements
- Compare the predictions of the developed model to driving records for a real case using various SRD models

3. Soil resistance models

The wave equation approach to pile driving simulation commonly assumes a load-deformation curve similar to the one idealised in Figure 3.1.

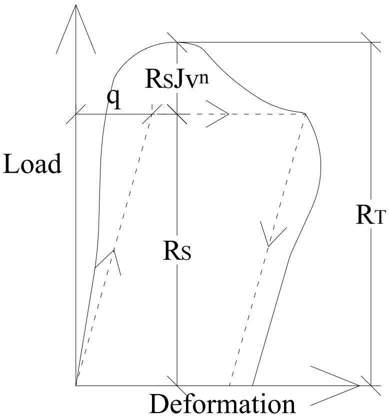

Figure 3.1. Assumed characteristic load-deformation curve of soil using static and dynamic contributions to the total resistance. Inspired by Bartoskewitz and Coyle [1970].

The total resistance to driving in the simplified wave equation approach can be obtained as the combined static and dynamic components [Pile Dynamics, 2010]:

$$R_{T,i} = R_{s,i}(1 + Jv_i^n) \tag{3.1}$$

where

$R_{T,i}$	Total soil resistance in the Smith model at a specific depth [N/m]
$R_{s,i}$	Current static resistance to driving at a specific depth [N/m]
J	Smith damping coefficient (may vary with depth) [s/m]
n	Damping exponent (may vary with depth) [-]

Different authors have proposed various models for obtaining the SRD, as the proportionality (3.1) proposed by Smith [1960] is still the most popular way of describing the resistance to driving.

McVay and Kuo [1999] lists a couple of different other models of the total resistance to driving. Generally, these resistance models are impractical as they depend on either:

- Driving data of a specific pile, such as penetration rate or derivatives hereof
- Shear strength, shear modulus or other in-situ parameters which may not be confidently obtainable from CPT measurements
- Assumptions regarding plane strain/stress and soil damping
- Empirical relations

For the sake of having a larger literature base, the basic Smith soil resistance model, Equation (3.1), is also adopted in the present project. This is further described in Section 4.2.

It should be recognized that the following properties is generally true for pile bearing capacity, also for large-diameter piles:

- Skin friction and toe resistance may not necessarily reach their ultimate values at the same time. This can be somewhat accounted for by splitting the total resistance in a toe and a skin friction contribution, albeit they can not easily be measured independently.
- Skin friction and toe resistance is not constant and it might be non-linearly dependent on displacement, penetration or both. An elastic-perfectly plastic approach is assumed in most Smith-based pile driving analysis with the lowest value being 0 and the highest being the "ultimate" resistance and vice versa for tension piles.
- The skin friction has a maximum value at a certain displacement, whereafter it decreases to a residual value.
- The skin friction is not active along the entire shaft at the same time, even during driving, meaning that the ultimate resistance can not be reached along the entire pile at the same time.

The SRD models may not necessarily incorporate all of these properties to a sufficient degree.

The total resistance is split in a tip and a skin resistance on both the inside and the outside of the pile, i.e.:

$$R_S = \pi D_o \int_0^p f_{s,o} dz + \pi D_i \int_0^p f_{s,i} dz + q_{tip} A_{end} \tag{3.2}$$

where

D_o, D_i	Outer and inner pile diameter
$f_{s,o}, f_{s,i}$	Outer and inner unit skin friction
q_{tip}	Unit tip resistance
A_{end}	End cross-sectional area

The stress field inside the pile which governs the middle part of Equation (3.2) is complicated and not well understood.

It is therefore common to model the internal friction as a fraction of the external resistance or alternatively reducing the unit friction to half and applying this value both internally (as inner skin friction) and externally (as outer skin friction), which is equivalent to averaging the outer and inner wall areas.

3.1 Common SRD models

Some common SRD models are discussed in the following. The review will be limited to **sands and fully coring behaviour**. Two main approaches have been identified: Dedicated empirical relations stating static resistance during driving, and simply using the ultimate capacities as resistance during driving. The latter is in most soil types a conservative approach as significant stiffness degradation occurs in most soils during driving. All methods are empirical or semi-empirical.

3.1.1 Toolan and Fox method

Toolan and Fox [1977] proposed a simple approach with skin friction and tip resistance being fractions of the measured CPT sleeve friction (clays only) and cone tip resistance, respectively.

The unit skin friction and tip resistance in sands are assumed as:

$$f_s = \frac{1}{300} q_c \quad , \quad q_{tip} = q_c \tag{3.3}$$

Anusic et al. [2016] used $q_{tip} = \frac{1}{3} q_c$ instead.

3.1.2 API method

The American Petroleum Institute (API) method as described in Anusic et al. [2016] is based on a *Recommended Practice* for design, but is nevertheless still used in driveability analysis for comparison purposes. The method therefore assumes the ultimate static resistance in a static load test equal to the static resistance during driving.

In that formulation, the unit skin friction and tip resistance are taken as:

$$f_s = 0.8 \sigma'_{v0} \tan\left(\varphi_f - 5^\circ\right) \quad , \quad q_{tip} = \sigma'_{v0} N_q \tag{3.4}$$

where

σ'_{v0}	Effective overburden pressure
φ_f	Angle of internal (or mineral) friction at failure
N_q	Bearing capacity factor, $8 < N_q < 50$

The expression for tip resistance is strictly empirical and seldom used when CPT data are available, as the precision entirely depends on the choice of N_q, which only depend on gradation of the material. Recommended values of N_q can be seen in Table 3.1. Furthermore, the value of 0.8 can be identified as the earth pressure coefficient, which in reality is obviously not a constant. Instead, e.g. $q_{tip} = \frac{1}{3} q_c$ can be used, according to Anusic et al. [2016].

Table 3.1. Recommended values of N_q in Equation (3.4) according to API [2002].

Soil type and rel. density	N_q
Loose-medium sand/silts to very loose sands	8
Medium-dense sand/silts to loose sands	12
Dense sand/silts to medium sands	20
Very dense sand/silts to dense sands	40
Very dense sands to dense gravels	50

Regarding the precision of the method, Kolk et al. [2005] states that it tends to underestimates the resistance for short piles and overestimates the resistance for long piles. This could indicate a bias of the method towards skin friction and also indicates that the tip resistance may be inaccurately approximated by the simple relation. The API method was developed for traditional small-diameter piles, which does not alter the stress field around the pile tip and within the pile as much as larger-diameter piles, and this may also influence the results.

3.1.3 Stevens method

This method was published in Stevens et al. [1982] which explicitly states methods for dealing with the coring/plugging question through a set of four cases. As fully coring behaviour is assumed in the present project, the internal and external skin friction are assumed equal, and the suggested values for skin friction and tip resistance are then:

$$f_s = 0.7\sigma'_{v0}\tan\left(\varphi_f - 5^\circ\right) \qquad , \qquad q_{tip} = 40\sigma'_{v0} \tag{3.5}$$

The suggestion is thus identical to the method suggested by API [1981], but with specific choice of N_q and a slightly reduced constant for f_s, and is not expected to be especially accurate.

3.1.4 Alm & Hamre method

The method includes the *friction fatigue* concept in the SRD model, with case studies confirming higher accuracy than older methods and comparable accuracy to contemporary methods being published regularly, see e.g. Anusic et al. [2016] and Byrne et al. [2012]. The friction fatigue concept was originally developed by Heerema [1978] with further recommendations given in Heerema [1979] and Heerema [1981]. Because the original formulation depends on the horizontal stress coefficient K, which is somewhat subjective and not a constant, the method is in its original form not applied. The model in widespread use was originally published by Alm and Hamre [1998]. Especially the revision directly correlating CPT measurements to the resistance [Alm and Hamre, 2001] has been proven fairly accurate by both the authors and subsequent studies.

The unit skin friction is determined with the same formulation for both clays and sand. The friction fatigue or stiffness degradation is governed by an exponential decay, but only a certain distance from the pile tip.

The unit skin friction is determined as:

$$\begin{aligned} f_s &= f_{s,res} + \left(f_{si} - f_{s,res}\right) e^{k(d-p)} \\ f_{si} &= K\sigma'_{v0}\tan\delta_{cv} \\ f_{s,res} &= 0.2 f_{si} \end{aligned} \tag{3.6}$$

where

f_{si}	Initial side friction
$f_{s,res}$	Residual side friction
K	Coefficient of lateral earth pressure
k	Shape factor of the friction degradation
d	Depth to actual layer
p	Pile penetration
δ_{cv}	Constant-volume or critical-state interface friction angle

The latter expression is still dependent on the earth pressure coefficient, but Jardine and Chow [1996] proposed using an empirical relation to the cone resistance:

$$K\sigma'_{v0} = 0.0132 q_c \left(\frac{\sigma'_{v0}}{p_a}\right)^{0.13} \tag{3.7}$$

where

p_a | Reference pressure $= 100\,\text{kPa}$

This formulation was derived assuming that the only contributing surface to the friction is the outside perimeter of the pile.

A common assumption is to reduce the unit friction to 50% and apply on both inside and outside of the pile (for sands), which is equivalent to taking the wall area as the average of the inner and outer areas. This might not be a reasonable assumption for t/D ratios (with t being wall thickness and D diameter of the pile) larger than what the model has been calibrated for, as the internal horizontal stress may then be significantly different. It is seen, that a best estimate of the interface friction angle and effective weight must still be used in conjunction with this method, which is a drawback with regards to operationality.

k has the purpose of facilitating a rapid friction degradation in dense sands and slower in clays, and is determined as:

$$k = \frac{\sqrt{\frac{q_c}{\sigma'_{v0}}}}{80} \tag{3.8}$$

The unit tip resistance in sands is taken as:

$$q_{tip} = 0.15 q_c \left(\frac{q_c}{\sigma'_{v0}}\right)^{0.2} \tag{3.9}$$

This value for tip resistance is then in between the recommendations of Anusic et al. [2016] of $q_{tip} = \frac{1}{3} q_c$ and Heerema [1981] of $q_{tip} = 0.55 q_c$.

3.1.5 Modified UWA-05 method

The University of Western Australia (UWA-05) [Lehane et al., 2005] method was developed to evaluate the static capacity of piles. It was derived from full-scale experiments using instrumentation which enabled recording of effective stresses. The calibration data sets used for the methods are unfortunately mostly small-diameter piles, resembling onshore conditions. Showed by Byrne et al. [2012], somewhat accurate predictions in North Sea sand with large-diameter piles may be obtainable anyway.

The UWA-05 method can in its original form not be used directly for predicting resistance to driving, but it is interesting in this context as it has been modified to account for the smaller resistance during driving by Schneider and Harmon [2010]. This modified version is presented here.

The unit skin friction in this model is:

$$f_s = \sigma'_{rf} \tan \delta_f = \left(\sigma'_{rc} + \Delta\sigma'_{rd}\right) \tan \delta_f \tag{3.10}$$

where

σ'_{rf}	Horizontal stress at failure
σ'_{rc}	Horizontal stress infinitely long time after installation
$\Delta\sigma'_{rd}$	Horizontal stress change during installation and equalisation
δ_f	Soil-pile interface friction angle at failure, $\approx \delta_{cv}$

σ'_{rc} and $\Delta\sigma'_{rd}$ are estimated as:

$$\begin{aligned} \sigma'_{rc} &= \frac{q_c\left(1-\frac{D_i}{D_o}\right)^{0.3}}{33}\left(\max\left(\frac{p-d}{D},2\right)\right)^{-0.5} \\ \Delta\sigma'_{rd} &= \frac{4G\Delta y}{D_o} \\ G &= 185 q_c q_{c,N}^{-0.7} \end{aligned} \tag{3.11}$$

where

G	Soil shear modulus
Δy	Assumed dilation = 0.02 mm
$q_{c,N}$	Normalised cone tip resistance $= \dfrac{q_c/p_a}{\left(\sigma'_{v0}/p_a\right)^{0.5}}$

According to Schneider and Harmon [2010], the uncertainty in estimating the ratio $f_{s,i}/f_{s,o}$ is larger than the difference in pile diameter and instead of applying half the unit resistance both externally and internally, the method consists of applying $1.5 f_{s,o}$ on the outside and nothing on the inside.

The unit tip resistance of the pile is taken as $q_{tip} = 0.35 q_c$.

3.1.6 MTD/ICP method

The Marine Technology Directorate (MTD) method (or Imperial College Pile (ICP) method) [Jardine and Chow, 1996] [Jardine et al., 2005] is another empirical method for obtaining the *ultimate* capacity of piles based on CPT measurements. Furthermore, the method depends on the geometry of the pile. Following the suggestion of Heerema [1978] and others, the MTD/ICP method also includes friction fatigue to some extent, but not as an exponential decay.

The unit shaft friction 10 days after driving is similarly to the UWA-05 method split in an effective radial stress component associated with ultimate capacity and a dilatancy contribution to the radial stress, and according to this method approximately given by:

$$\begin{aligned} f_s &= \left(a q_c \left(\frac{\sigma'_{v0}}{p_a} \right)^b (\max(h/R^*, 8))^c + \frac{2G\Delta r}{R} \right) \tan\delta_{cv} \\ R^* &= \sqrt{R_o^2 - R_i^2} \quad , \quad h = p - d \\ G &= q_c \left(0.0203 + 0.00125\eta - 1.216 \cdot 10^{-6}\eta^2\right)^{-1} \\ \eta &= q_c \left(p_a \sigma'_{v0}\right)^{-0.5} \end{aligned} \tag{3.12}$$

where

a, b, c	Empirical coefficients, Jardine et al. [2005] and Jardine et al. [2015] suggests $a = 0.029$, $b = 0.13$ and $c = -0.38$
Δr	Radial displacement mobilising a radial effective stress change $\approx 0.02\,\mathrm{mm}$
δ_{cv}	Critical-state interface friction angle as determined in direct shear test (discussed in Section 3.3)
R_o, R_i	Outer and inner pile radii

Jardine et al. [2005] states that the $\frac{2G\Delta r}{R}$ part is mainly dominant for small-diameter piles.

Jardine and Chow [1996] also supplies a criteria for when pipe piles should be considered plugging or not. Piles are considered coring if:

$$D_o > 0.02\,(D_r - 30) \tag{3.13}$$

where

D_r	Relative density of soil at pile tip [%]

Equation (3.13) suggest that all large-pile (larger than say $D_o = 2\,\mathrm{m}$) can be considered fully coring, supporting the initial assumption. The expression does not, however, account for the pile wall thickness or penetration and can thus only be a guideline. The end bearing for unplugged piles is approximated as:

$$q_{tip} = q_c \tag{3.14}$$

Jardine et al. [2005] states that studies have shown that the "pure" end bearing is only approximately $0.7q_c$, but the extra contribution accounts for the inner side friction in coring piles, and the side friction in this method should thus only be applied over the outer area - no explicit inner skin friction should be included.

3.1.7 Fugro 2004 method

API commissioned Fugro in 2004 to improve their design formulae for open-ended piles driven into silica sands. Both the MTD method and various load tests performed suggested that the API method was unreliable. Furthermore, the value of φ is not easily obtainable and not a constant.

Fugro modified the MTD method accordingly and calibrated the empirical constants using a set of tension and compression pile load tests in sand. Five degrees of confidence based on a subjective estimate on the reliability of the data was assigned to each set, and a statistical fit mainly focused on the two highest categories of confidence was performed. According to Kolk et al. [2005], the best estimate for the shaft resistance in compression tests were:

$$f_s = \begin{cases} 0.08 q_c \left(\frac{\sigma'_{v0}}{p_a}\right)^{0.05} (h/R^*)^{-0.90} & \text{for} \quad h/R^* > 4 \\ 0.08 q_c \left(\frac{\sigma'_{v0}}{p_a}\right)^{0.05} (h/R^*)^{-0.90} \left(\frac{h}{4R^*}\right) & \text{for} \quad h/R^* < 4 \end{cases} \tag{3.15}$$

The best estimate for end bearing in compression was found to be:

$$q_{tip} = p_a 8.5 \sqrt{\frac{\overline{q_c}}{p_a}} \sqrt{\frac{R^*}{R_o}} \tag{3.16}$$

where

$\overline{q_c}$	Average cone tip resistance in a depth of $\pm 1.5D$ of the pile tip

Like the MTD method, the Fugro 2004 method is most likely an upper bound on the encountered resistance during driving, as the soil resistance generally increases over time in sandy soils. Equation (3.15) contains several relatively precisely calibrated values, and it is thus possible to question its validity over a wider array of data. As for all statistical fits on small populations, the risk of bias is high. Clausen et al. [2005] indeed criticises the method used by Kolk et al. [2005] in sharp terms, shows that it is biased and claims that a very large skin friction near the pile tip, inconsistent with previous studies, is needed in order to obtain the results of Kolk et al. [2005]. It is assumed that the side friction suggested is applied with half the value on the inner and half on the outer area, as nothing else is stated in Kolk et al. [2005].

3.1.8 NGI-99 method

The NGI-99 method [Clausen and Aas, 2001] is based on an extensive NGI static load test database and in Clausen et al. [2005] compared to the same data set as the Fugro 2004 method. Like the Fugro 2004 and MTD methods, the NGI method includes a friction fatigue effect. Augustesen [2006] contains an extensive study on various pile load tests and recommends the NGI-99 method for open-ended piles longer than 15 m over several other methods.

The unit friction in the NGI-99 method is found as:

$$f_s = \frac{d}{p} p_a F_{Dr} F_{sig} F_{tip} F_{load} F_{mat} \quad , \quad f_s > 0.1 \sigma'_{v0} \tag{3.17}$$

$$F_{Dr} = 2.1 \left(D_r - 0.1\right)^{1.7} \tag{3.18}$$

$$F_{sig} = \left(\frac{\sigma'_{v0}}{p_a}\right)^{0.25} \tag{3.19}$$

$$F_{tip} = 1.0 \quad \text{(open-ended pile)} \tag{3.20}$$

$$F_{load} = 1.3 \quad \text{(compression)} \tag{3.21}$$

$$F_{mat} = 1.0 \quad \text{(steel)} \tag{3.22}$$

where

D_r	Relative density at depth d

The analogy to the Alm & Hamre friction fatigue effect (Equation (3.6)) is that the initial strength is $f_{s,i} = p_a F_{Dr} F_{sig} F_{tip} F_{load} F_{mat}$, the residual is $f_{s,res} = 0.1\sigma'_{v0}$ and the friction degradation factor is $\frac{d}{p}$.

The method requires that the following expression for relative density is used:

$$D_r = 0.4 \ln\left(\frac{q_c}{22\sqrt{\sigma'_{v0} p_a}}\right) \tag{3.23}$$

which can result in a relative density larger than 1.0, which should be used anyway. Consequently, it is in general terms an empirical variable relating soil unit resistance to $a\left(\ln\left(\frac{q_c}{\sigma'_{v0}}\right)\right)^b$ where a and b are empirical constants.

The NGI-99 method is different from the others as there is direct provisions for dealing with open-ended piles. The unit friction above only applies to the outside of the pile wall, whereas the inside friction for coring piles is included in the unit tip resistance.

Tip resistance in the NGI-99 method is found as:

$$Q_{tip} = 3 f_s A_s + A_{end} q_c \tag{3.24}$$

where

A_s	Inside wall area $\approx L D_i \pi$ (coring)
L	Pile length

In the original form, the NGI-99 method depends on knowledge about the soil plug length, which in this case is assumed equal to the pile length. This may not be accurate for small pile diameters.

It is seen that the method, when assuming fully coring behaviour, simply assumes a pile end bearing $q_{tip} = q_c$ and a total skin friction distributed with 25% on the outside and 75% on the inside of an open-ended pile, which means that the equations for total soil resistances in this case are:

$$R_s(0 < d < p) = f_s(A + 3A_s) \tag{3.25}$$

$$Q_{tip} = q_c A_{end} \tag{3.26}$$

where

$R_s(0 < d < p)$	Total skin resistance in depth d
A	Outside wall area

3.2 Discussion of SRD models

As previously discussed, the CPT penetration tests are common. The presented SRD models uses CPT data more or less directly. Generally, CPT and piles have similarity regarding geometry and primary stress directions, and semi-empirical relations between these data and the SRD seems reasonable. The total tip resistance might be similar to the pile end bearing and the sleeve friction to the shaft resistance.

According to Schneider et al. [2010], some phenomena create dissimilarity:

- Reduction in radial stress some distance behind pile/cone tip
- Reduction in radial stress along the pile/CPT sleeve due to friction fatigue
- Changes in local radial stress due to pile loading during driving
- Different interface friction angles for CPT and pile due to different roughness
- Set-up of soil strength and/or effective stresses due to longer duration
- Reduction in strength due to progressive failure of softening soils

All these phenomena may create bias in any CPT-based resistance model. The sleeve friction is generally never used in correlations in drained-behaviour soils, as the cone generally induces a failure zone some distance around the cone, which invalidates the sleeve friction as a measurement of undisturbed friction, and because some excess pore pressure is generally needed for sufficient adhesion to develop.

The incorporation of driving shoes alters the distribution of horizontal stress within the pile, further complicating the comparison between CPT measurements and SRD. An accurate SRD model must thus be based on fundamental soil properties, but even if these properties are available, most of the mentioned phenomena can not be modelled fully. The only realistic way of obtaining SRD models for practical use is through calibration using CPT data and estimates on at least unit weight and relative density of individual soils.

Using design formulas for assessing the resistance to driving can be questionable, but the omission of these will probably lead to bias towards "pure" SRD models, which may be uncertain, and is based on limited data sets. The static load test based methods like the NGI-99 can be used as a SRD model for comparison purposes.

The CPT-based resistance formulas are generally favoured, as they tend to be more accurate in sands, and studies (including Jardine and Chow [1996]) have suggested that they can be precise for tubular piles in silica sands, other studies have shown significant bias in the empirical relations. All design methods for piles have to some extent been subject to controversy because of their empirical nature [Augustesen, 2006]. The problem is too complex to accurately and economically model in its entirety and thus a large number of very different, but essentially non-physical design methods have emerged. These methods can be referred to as "grey box"-methods, as they are at least somewhat physically appropriate. In comparison, the energy-balance equations dynamic formula as discussed in Section 2.1 can be called "black box"-methods.

3.2.1 Side friction

Regarding the shear strength at the pile sides, or skin friction, the core of all the models is essentially the Mohr-Coulomb criterion:

$$f_s = K\sigma'_{v0} \tan \delta_f \tag{3.27}$$

Obtaining the horizontal pressure $K\sigma'_{v0}$ is not straightforward for pile driving, as it is merely a crude representation of a much more complex stress state and because the earth pressure coefficient K depends on the stress itself. Thus, empirical relations between either K, $K\sigma'_{v0}$ or the entire expression $K\sigma'_{v0} \tan \delta_f$ and the CPT cone resistance have been developed.

The Fugro 2004 and NGI-99 models do not explicitly include the need for calculating friction angles for individual layers, and are thus the methods needing the smallest amount of user input. The UWA-05, MTD/ICP and Fugro 2004 methods include the actual pile geometry in the resistance, a feature not included in e.g. the Alm & Hamre model.

The Alm & Hamre, MTD/ICP and Fugro 2004 methods all include similar expressions for $K\sigma'_{v0}$, the main difference being different values of the associated constants.

The MTD/ICP and UWA-05 includes an additional term which for most cases will be small, but serves to include the small changes in radius due to Poisson effect and associated change in surface roughness to median grain size of the soil, which alters the stress state somewhat.

The Alm & Hamre model includes friction fatigue explicitly through the use of an exponential decay between a "residual" resistance given as a fraction of the "initial" resistance, depending on the relative pile penetration h. Some of the other models (UWA-05, MTD, Fugro 2004 and NGI-99) also account for friction fatigue, as they similarly include h in one way or another. The degradation exponent used in the Alm & Hamre method is also an empirical relation, dependent on the cone tip resistance normalised with overburden pressure.

Examining the MTD/ICP, UWA-05 and Fugro 2004 methods, it is clear that these are special cases of the same formula, as stated in API [2002, Errata and Supplement 3]. The methods however differ in their treatment of wall thickness and whether or not a contribution due to transversal deformation is included, which is not accounted for in the review made in API [2002, Errata and Supplement 3].

Generally, the unit resistance per pile length of the suggested methods can all be written in the form:

$$f_s(z) = C_{method} f_0 F_{FF} \tan \varphi_{method} \tag{3.28}$$

where

F_{FF}	Friction fatigue coefficient, dependent on d, p, q_c, σ'_{v0}, R_o, R_i
f_0	Base-value side friction of model, dependent on q_c, σ'_{v0}, R_o, R_i
φ_{method}	Method-specific friction angle
C_{method}	Method-specific pile circumference

Depending on model, f_0 may model the horizontal pressure $K\sigma'_{v0}$ or the entire friction expect friction fatigue.

The various methods vary greatly in the parameters used for correlation, the weight on each parameter and more. An overview can be seen in Table 3.2, 3.3 and Figure 3.2. It is seen that some of the expressions contains a second part, corresponding to the $\Delta\sigma'_{rd}$ part of e.g. Equation (3.10) which, according to Jardine et al. [2005] corresponds to a change in the stress state in the failure zone due to radial stress induced on the soil from a) Poisson effect in the compressed pile material and b) dilation changing the principal stress directions and strength slightly. This contribution may be small for large piles. It can be estimated according to cavity expansion theory to be:

$$\Delta\sigma'_r = \frac{2G\Delta r}{R} \tag{3.29}$$

where Δr corresponds to the roughness of the pile surface, which is the displacement necessary for slip to occur.

Table 3.2. Model parameters of various methods for obtaining the side resistance part of the SRD per unit pile length. All general assumptions mentioned apply. C is external circumference and C_s is internal circumference.

Method	C_{method}	f_0
Toolan & Fox	$\frac{C+C_s}{2}$	$\frac{q_c}{300}$
API	$\frac{C+C_s}{2}$	$0.8\sigma'_{v0}$
Stevens	$\frac{C+C_s}{2}$	$0.7\sigma'_{v0}$
NGI-99	$C+3C_s$	$2.1\left(0.4\ln\left(\frac{q_c}{22\sqrt{\sigma'_{v0}p_a}}\right)-0.1\right)^{1.7}\cdot 1.3\left(\frac{\sigma'_{v0}}{p_a}\right)^{0.25}$
Alm & Hamre	$\frac{C+C_s}{2}$	$0.0132q_c\left(\frac{\sigma'_{v0}}{p_a}\right)^{0.13}$
Fugro 2004	$\frac{C+C_s}{2}$	$0.08q_c\left(\frac{\sigma'_{v0}}{p_a}\right)^{0.05}$
UWA-05	$\frac{3C}{2}$	$\frac{q_c\left(1-\frac{R_i}{R_o}\right)^{0.3}}{33}+\frac{7.4\cdot 10^{-3}q_c}{F_{FF}\left(\frac{q_c}{p_a\sqrt{\sigma'_{v0}/p_a}}\right)^{0.7}R_o}$
MTD/ICP	C	$0.029q_c\left(\frac{\sigma'_{v0}}{p_a}\right)^{0.13}+\frac{4\cdot 10^{-5}q_c}{F_{FF}\left(0.0203+\frac{0.00125q_c}{\sqrt{p_a\sigma'_{v0}}}-\frac{1.216\cdot 10^{-6}q_c^2}{p_a\sigma'_{v0}}\right)R_o}$

Figure 3.2 shows the value of these SRD models as function of depth for an example case. The NGI-99 method is seen to be predicting the largest total side resistance by far, which can probably be attributed to its context as a relatively new design capacity formula. Historically, very little confidence has been put on the side resistance in sands - which has been remedied by the newer

Table 3.3. Model parameters (continued) of various methods for obtaining the side resistance part of the SRD per unit pile length. All general assumptions mentioned apply.

Method	φ_{method}	F_{FF}
Toolan & Fox	45°	1
API	$\varphi_f - 5°$	1
Stevens	$\varphi_f - 5°$	1
NGI-99	45°	$\frac{d}{p}$, for $F_{FF} f_0 \geq 0.1\sigma'_{v0}$ $\frac{\sigma'_{v0}}{10 f_0}$, for $F_{FF} f_0 < 0.1\sigma'_{v0}$
Alm & Hamre	δ_{cv}	$0.2 + 0.8\exp\left(\frac{\sqrt{q_c/\sigma'_{v0}}}{80}(d-p)\right)$
Fugro 2004	45°	$\left(\frac{h}{\sqrt{R_o^2 - R_i^2}}\right)^{-0.9}$, for $h/\sqrt{R_o^2 - R_i^2} \geq 4$ $\left(\frac{h}{\sqrt{R_o^2 - R_i^2}}\right)^{-0.9}\left(\frac{h}{4\sqrt{R_o^2 - R_i^2}}\right)$, for $h/\sqrt{R_o^2 - R_i^2} < 4$
UWA-05	δ_{cv}	$\left(\frac{h}{2R_o}\right)^{-0.5}$, $F_{FF} \geq \frac{\sqrt{2}}{2}$
MTD/ICP	δ_{cv}	$\left(\frac{h}{\sqrt{R_o^2 - R_i^2}}\right)^{-0.38}$, $F_{FF} \geq 0.454$

methods (e.g. NGI-99, MTD/ICP and Fugro 2004). A clear trend regarding the UWA-05 and Alm & Hamre models is that they predict comparatively low resistances, similar to the API method. This might be an indication of their roles as "pure" driving resistance models, and not design capacity formulas.

3.2.2 Tip resistance

The reviewed methods are slightly different and assume that the unit tip resistance is either:

- Proportional to the cone tip resistance, either simply the value or a fraction of the value at the pile tip, or using an average value of q_c some distance above and below the pile tip,
- dependent on the cone tip resistance normalised with overburden pressure,
- or dependent on the cone tip resistance normalised with the reference pressure and the relative pile diameter,

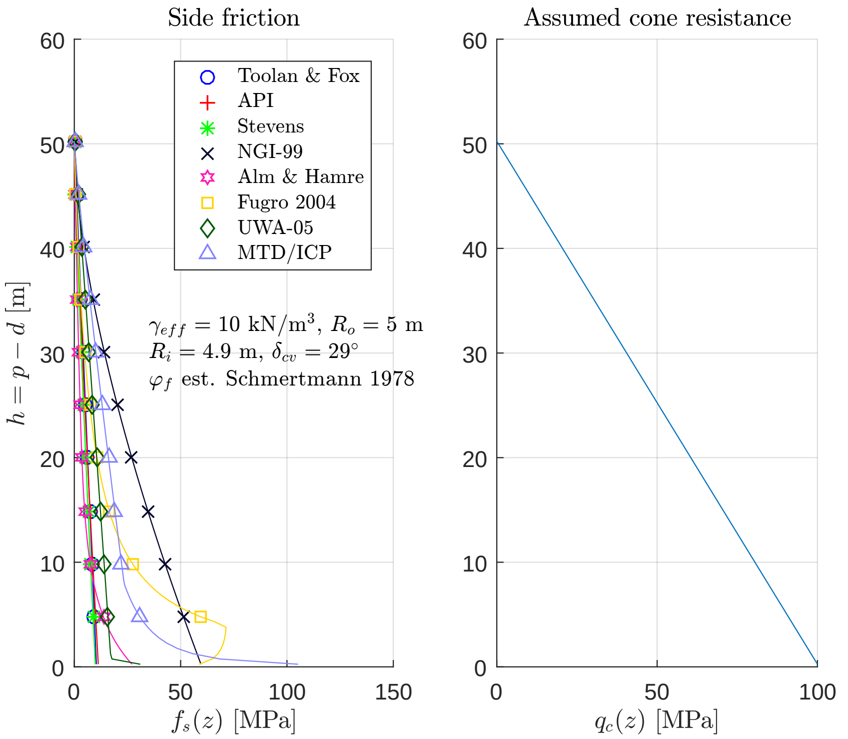

Figure 3.2. Equation (3.28) as function of depth for various SRD models.

The API and Stevens methods essentially assumes a very simplified version of Terzaghi's bearing capacity theorem for circular foundations, which in its general form is:

$$q_{tip} = 1.3c'N_c + \sigma'_{v0}N_q + 0.3\gamma' D N_\gamma \tag{3.30}$$

$$N_q = \frac{e^{2\pi\left(0.75-\frac{\varphi'}{360}\right)}\tan\varphi'}{2\cos^2(45° + 0.5\varphi')} \tag{3.31}$$

$$N_c = \frac{N_q - 1}{\tan\varphi'} \tag{3.32}$$

$$N_\gamma = \frac{2(N_q + 1)\tan\varphi'}{1 + 0.4\sin 4\varphi'} \tag{3.33}$$

where

φ'	Effective friction angle

The reason for why the direct correlation between tip resistance and cone resistance is assumed across the literature (except for the API method) can according to Jardine et al. [2005] be attributed to the fact that:

- The factors N_q, N_c, N_γ etc. are unrepresentative of the real stress field with increasing depth because of the large overburden pressure, dilation and crushing.
- The problem is highly anisotropic, non-linear and pressure-dependent.

These factors make theoretical/analytical solutions very difficult and also unreliable.

A general form of the reviewed methods for obtaining unit tip resistance for fully coring piles driven in sand can be:

$$q_{tip} = a q_c^b F_{A_{end}} F_{\sigma'_{v0}} F_{\overline{q_c}} \tag{3.34}$$

where

a, b	Fitting constants
$F_{A_{end}}$	Correction for end area proportions
$F_{\sigma'_{v0}}$	Correction for normalisation against overburden pressure
$F_{\overline{q_c}}$	Correction for cone tip resistance averaging

The values of the model parameters for the various reviewed methods can be found in Table 3.4. The models are plotted as function of cone resistance and effective vertical stress in Figure 3.3. It seems as though the Fugro 2004, Stevens and API methods all predict very low tip resistances compared to the rest. This reflects the general trend in the discussions of open-ended pile tip resistance in the literature, which more or less agrees that this is an area of high uncertainty. The distinction between design capacity formulas and pure driving resistance models is not as clear for the tip resistance compared to the side friction.

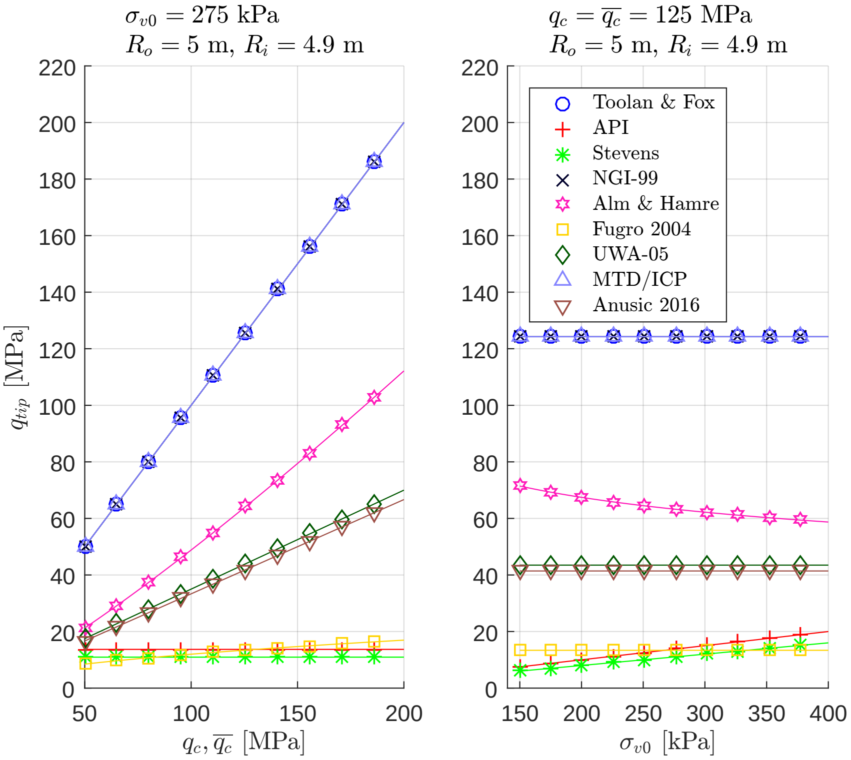

Figure 3.3. Equation (3.34) as function of cone resistance and overburden pressure. The averaged and local value of the cone resistance is in this graph assumed equal.

All models of this nature are somewhat controversial, as they are not fundamental and generally rely heavily on empirical fitting coefficients. The assessment of SRD is further complicated by the fact that it is difficult to measure tip resistance independently of side friction. In reality, the failure zone at the tip obviously effects the side friction and vice versa, but the extent and the stress regime is unclear.

Table 3.4. Model parameters of various methods for obtaining the tip resistance part of the SRD per unit pile length. All general assumptions mentioned apply. $\overline{q_c}$ may be obtained using averaging over $\pm 1.5D$ or $\pm 1.5D_{eq}$ or simply as $q_c(z = p)$.

Method	a	b	$F_{A_{end}}$	$F_{\sigma'_{v0}}$	$F_{\overline{q_c}}$
Toolan & Fox	1	1	1	1	1
API	1	0	1	$(8 \text{ á } 50)\,\sigma'_{v0}$	1
Stevens	1	0	1	$40\sigma'_{v0}$	1
NGI-99	1	1	1	1	1
Alm & Hamre	0.15	1.2	1	$\frac{1}{\left(\sigma'_{v0}\right)^{0.2}}$	1
Fugro 2004	1	0	$\sqrt{\frac{\sqrt{R_o^2 - R_i^2}}{R_o}}$	1	$8.5 p_a \sqrt{\frac{\overline{q_c}}{p_a}}$
UWA-05	0.35	1	1	1	1
MTD/ICP	1	0	1	1	$\overline{q_c}$
Toolan & Fox, mod. Anusic 2016	0.33	1	1	1	1

The CPT-based models (generally perceived to be more advanced and accurate in engineering practice) are essentially regressions between the horizontal earth pressure coefficient and CPT cone resistance, with varying degrees of confidence (with respect to statistical population size and similarity to large-diameter pile conditions). As such they are not invariant to the specific conditions under which they were derived, especially if geometry or loading rate is significantly different.

The investigated models fail to convincingly include parameters influencing the actual stress state within a coring pile in any way, i.e. load rate, the influence of pile diameter, pile wall thickness variations, dilation and compression of the soil etc. This is probably due to the fact that it is impossible to solve analytically and correlations in a more "black-box" sense have thus been preferred. This comes to show, as the models vary in what wall area the unit side friction should be applied over, and are vague in their definitions of what is internal and what is external friction.

3.3 Operational parameters required

The methods listed above requires various parameters as input which can not be unambiguously determined. These are therefore discussed in the following paragraphs. Some guides to obtaining basic parameters from CPT measurements can be found in Appendix A.

It can be uncertain to directly apply research regarding ultimate capacities, as the literature is to some extent concerned with finding *design resistances*. This means that conservative (low) values of i.e. interface friction angle is generally recommended, but this is of course not conservative regarding driveability analysis for the reasons mentioned in the introduction. On the other hand, most of the methods are based on post-driving load tests (say, 10 days after driving as for example in Jardine et al. [2005]) at which point some of the conservatism may have been evened out by the increased strength with time.

3.3.1 Averaging of cone tip resistance

The Fugro 2004 method suggest using an average value of the cone tip resistance in determining the pile tip resistance, generally over a distance some multiple of the pile diameter. This averaging of the cone resistance may become very crude for large-diameter piles, e.g. a pile with a diameter of 5 m would require averaging the cone tip resistance over a depth of 15 m, where the overburden pressure and soil properties are obviously hugely different. Instead, it can be suggested to either:

- Average the cone resistance normalised with local overburden pressure and then multiplying the value with the overburden pressure at pile tip
- Average the cone resistance over a distance of $\pm 1.5 D_{eq}$ instead, where $D_{eq} = 2\sqrt{\frac{A_{end}}{\pi}}$ (commonly applied)
- Not average the cone resistance and simply use the best-estimate interpolated cone resistance at the pile tip (preferable if data quality is varying or incomplete)

3.3.2 Critical-state or constant-volume interface friction angle

The Alm & Hamre, UWA-05 and MTD/ICP methods requires determination of the constant-volume interface friction angle δ_{cv}. The description of the friction angle in Alm and Hamre [2001] does not state whether the friction angle should be taken as the interface or only the mineral friction, but Schneider and Harmon [2010] assumes that it is the interface friction angle and this is therefore also assumed in the present project. The interface friction angle δ depends, among other things, on:

- The grain size, shape and involved mineral type of the sand
- The hardness, roughness and coating quality of the pile
- Stress state and void ratio of the sand

Randolph et al. [1994] states that the range of δ is in the region 0.6-0.7 times the peak measured friction angle. The peak friction angle has several components as seen in Figure 3.5.

A drained shearing test of a soil may typically exhibit a behaviour similar to the one seen in Figure 3.4. The soil may, depending on whether it is normally consolidated clay or loose sand ("wet" (W) side of the critical state line (CSL)) or if it is heavily overconsolidated clay or dense sand ("dry" (D) side of the CSL) either compress or dilate. This results in the possible ambiguity in talking about a single friction angle, as the shear resistance will then have several contributing factors. This can be illustrated by Figure 3.5.

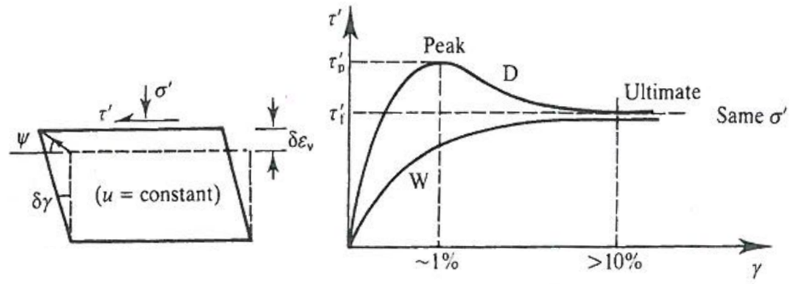

Figure 3.4. Typical drained shear test behaviour of either dense and loose sands or normally and overconsolidated clays. From [Atkinson, 2007].

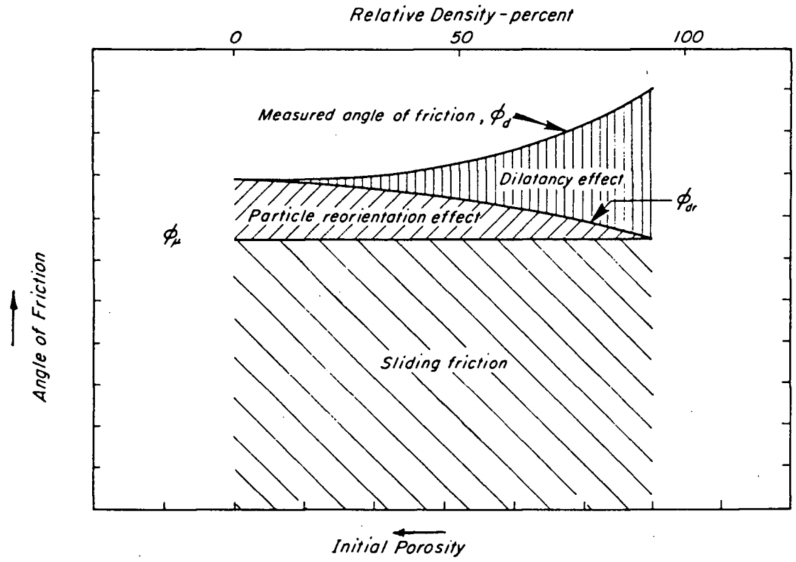

Figure 3.5. Suggested components of the shear resistance of sands. From Wijewickreme [1986].

When the soil reaches the CSL, a unique relationship exists between the normal and shear stress and the void ratio, i.e. the critical-state parameters may be seen as "material constants" [Schofield and Wroth, 1968]. The CSL is defined as:

$$\tau'_f = \sigma'_f \tan \varphi'_{cv} \tag{3.35}$$

where

τ'_f, σ'_f	Shear and normal stress at failure
φ'_{cv}	Critical-state or constant-volume eff. friction angle

This concept of critical state mineral friction also extends to the interface friction angle used in the described methods.

Jardine et al. [2005] suggests that a direct-shear test should be performed for all involved soil types. This may involve considerable effort and it can be difficult to control the stress state correctly in these types of tests, which means that it is not economically feasible for most real applications. Instead, guidelines and correlations to CPT data may be performed. Various correlations to the value exist, for which one suggested by Jardine et al. [2005] is seen in Figure 3.6. It is seen that a trending value is found as $\delta_{cv} = 29°$, which CUR C118 [2001] argues that all sands will tend towards because of local crushing. The more elaborate curve by Jardine was made from clean standard well-sorted test sands and close to smooth steel plates using direct shear equipment. The Shell UK Ltd trendline is based on ring shear (Bishop) tests. Generally, it is seen that the interface friction angle may be reduced for coarser-grained soils, as the difference between steel surface roughness and particle size increases and reduces the friction.

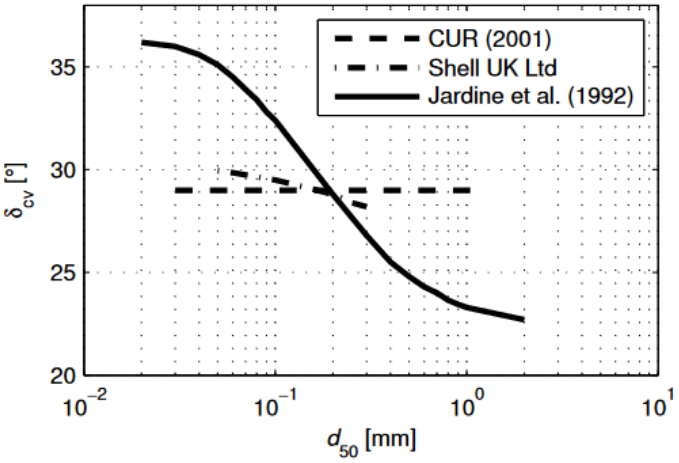

Figure 3.6. Trends in correlation of critical-state soil-steel interface friction angle to mean grain size. Modification of Thomassen [2016, Figure 2.3] (based on Jardine et al. [2005, Figure 5]).

API [2002, Errata and Supplement 3] states that an upper limit on the interface friction angle corresponds to the statement by CUR C118 [2001], $\tan \delta_{cv} \leq 0.55$.

It is in reality not practical to perform either shear tests of accurately determine the mean grain size for a sufficiently high resolution of depths. On the other hand, using $\delta_{cv} = 29°$ might be convenient and conservative for design equations, it might be too low for dense or very dense sands.

The empirical relation of $\delta_{cv} = \varphi_f - 5°$ as suggested by e.g. Stevens et al. [1982] might actually be more accurate in driveability analysis.

3.4 Quake and damping

Apart from the static resistance which may be related to the ultimate capacity of the pile as discussed in the previous sections, the three parameters related to the soil stiffness and damping in the Smith model of resistance is the quake or deformation at yield q (as seen in Figure 3.1), the damping coefficient J and the damping exponent n. Pile Dynamics [2010] provides some guidelines to what values might be used.

As the Smith model is merely a convenient approximation and can not accurately represent the complex behaviour of the surrounding soil, the uniqueness of the parameters is not ensured [Forehand and Reese, 1964]; a number of different combinations of q, J and n may yield the exact same result for a particular driving condition. Because of this and because of the high uncertainty on soil parameters in general, a pile driving analysis [Pile Dynamics, Inc., 2017] is often performed when driving either pilot piles or on all piles. The analysis consists of iterative signal matching between a pair of strain gauges (which can then provide velocity and force through $F = Zv$, with Z being pile impedance) mounted on the pile top and a Smith model. This "signal"-matching approach can be viewed as the inverse of a driveability study and is iterated until an acceptable particular solution for these three (six including pile tip damping and quake) variables are found. If no signal matching analysis has been performed, the values must be estimated.

McVay and Kuo [1999] examined an array of various theoretical expressions for the damping and quake parameters presented by Liang and Sheng [1992], but found that they are impractical to evaluate given the typical data available when driving piles. McVay and Kuo [1999] disregarded the non-linearity of the damping (assumes damping exponent $n = 1$) and performed a linear regression using the following proportionality assumptions:

$$q \propto \{\text{Soil type}, \quad N_s(p), \quad E_{eff}\} \tag{3.36}$$

$$q_t \propto \{\text{Soil type}, \quad N_t(p), \quad E_{eff}, \quad D_o\} \tag{3.37}$$

$$J \propto \{\text{Soil type}, \quad N_s(p), \quad E_{eff}\} \tag{3.38}$$

$$J_t \propto \{\text{Soil type}, \quad N_t(p), \quad E_{eff}\} \tag{3.39}$$

where

q, q_t	Skin and tip quake, respectively
J, J_t	Skin and tip Smith damping coefficient, respectively
Soil type	Cohesive, non-cohesive, other
$N_s(p)$, $N_t(p)$	SPT-N value at side and tip, respectively, at current penetration
E_{eff}	Transferred energy to pile top

A database consisting of 21 cases were used by McVay and Kuo [1999] for a regression. The data consisted of:

- Failure criteria from static load test
- PDA results
- Driving logs with blowcounts
- SPT profiles

The regression performed was unfortunately not using normalised relations to the transferred energy and is thus a function of time. As all the input data were wildly scattered, the equations found were at best small improvements over the default values of Pile Dynamics [2010] and show coefficients of variation to PDA measurements larger than 0.4.

API [2002] gives provisions regarding the quake values in sands and clays for both side friction and tip resistance in terms of the phrase "movement required to mobilize full resistance". For side friction, the recommendation is identical to that of Pile Dynamics [2010], i.e. 0.1 inch or 2.5 mm. A non-linear function is recommended for toe quake with the ultimate quake recommended as $0.1D$. This may create very large quake values and thus little end stiffness for typical monopiles and should probably be used with caution in driveability analysis.

Conclusively, it does not seem justifiable to deviate from the recommendations of Pile Dynamics [2010] regarding quake and damping. Deviating much from the recommendations will because of the lack of uniqueness also invalidate some of the SRD relations specified in the previous section.

4. Development of program for pile driving simulation

The dynamics of pile driving is a complex system, which can not be solved analytically to sufficient accuracy. In order to obtain a solution, a finite element model of the system has been developed. This chapter contains a description of the developed program.

It is assumed that the pile material is fully elastic at all times, whereas the soil can naturally be highly non-linear in its behaviour.

4.1 Pile model

The continuous pile is modelled as a finite element system. As shown in Chapter 2, the problem can be considered as a one-dimensional wave propagation problem. A free-body diagram of the system can be seen in Figure 2.2 and for an infinitesimal pile element in Figure 4.1. In reality, the problem is of course three-dimensional and continuous, but as discussed a closed-form solution to the problem can only be found if a) tip resistance is neglected, b) the skin friction is continuous and c) the stiffness of the pile itself is constant along the length of the pile. Neither of these conditions are upheld in most cases, and a numerical solution of the problem is therefore needed. It is assumed that a full three-dimensional model of the pile itself is unnecessary, as the pile to all intents and purposes is completely uniform within each segment, and shear waves are thus assumed to be negligible.

4.1.1 Finite element procedure

The basic steps of the Galerkin finite element method is [Cook et al., 2002] [Andersen, 2006]:

1. Establish strong form (differential equation)
2. Establish weak form (multiplying by a virtual field and integrating by parts)
3. Discretize the field in nodal values
4. Select shape functions for physical and virtual field
5. Compute element matrices
6. Assemble global system matrices and obtain global system of equations
7. Apply nodal forces and boundary conditions
8. Solve system
9. Strains etc. are obtained by interpolation

Strong form

Considering an infinitesimal pile element seen in Figure 4.1, force balance and using d'Alemberts principle yields the equation of motion for the pile, Equation (4.1).

$$EA\frac{\partial^2 u(y,t)}{\partial y^2} + p(y,t) = \rho A\frac{\partial^2 u(y,t)}{\partial t^2} \tag{4.1}$$

where

EA	Axial stiffness
$u(y,t)$	Displacement
$p(y,t)$	Loads including gravity, hammer impact and soil resistance
ρA	Unit mass per length

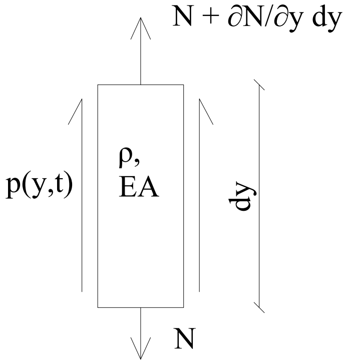

Figure 4.1. Free-body diagram of an infinitesimal pile element.

Weak form

The weak form of Equation (4.1) is obtained for a single bar element by multiplying with the virtual field $\delta u(y,t)$ and integrating over an element length $l_e = y_{e,2} - y_{e,1}$ (where $y_{e,1}$ and $y_{e,2}$ are the first and second end coordinate of the element respectively):

$$\int_{y_{e,1}}^{y_{e,2}} \delta u(y,t) EA\frac{\partial^2 u(y,t)}{\partial y^2}dy + \int_{y_{e,1}}^{y_{e,2}} \delta u(y,t)p(y,t)dy = \int_{y_{e,1}}^{y_{e,2}} \delta u(y,t)\rho A\frac{\partial^2 u(y,t)}{\partial t^2}dy \tag{4.2}$$

Using integration by parts gives:

$$\begin{aligned}
&\int_{y_{e,1}}^{y_{e,2}} \frac{\partial \delta u(y,t)}{\partial y} EA\frac{\partial u(y,t)}{\partial y}dy + \int_{y_{e,1}}^{y_{e,2}} \delta u(y,t)\rho A\frac{\partial^2 u(y,t)}{\partial t^2}dy \\
&\quad = [\delta u(y,t)N(y,t)]_{y_{e,1}}^{y_{e,2}} + \int_{y_{e,1}}^{y_{e,2}} \delta u(y,t)p(y,t)dy \qquad (4.3)\\
&N(y,t) = EA\frac{\partial u(y,t)}{\partial y}
\end{aligned}$$

It is possible to identify $[\delta u(y,t)N(y,t)]_{y_{e,1}}^{y_{e,2}}$ as the normal forces at each element end.

Discretization and shape functions

For convenience and because the gradients within elements are not of particular interest in this application, linear interpolation is applied. The system is therefore defined by two-node bar

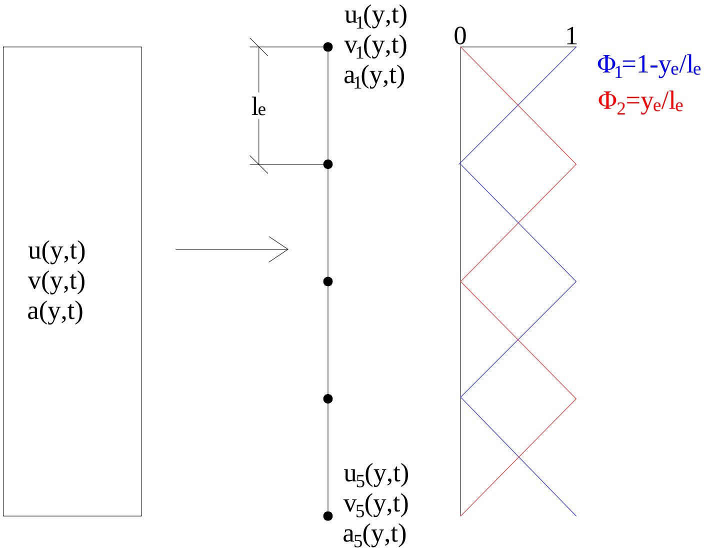

Figure 4.2. Discretization of pile and shape functions.

elements, as seen in Figure 4.2. The physical and virtual displacements at the introduced degrees of freedom for each element can then be described by:

$$\{u_e(y,t)\} = \begin{bmatrix} u_{e,1}(t) & u_{e,2}(t) \end{bmatrix}^T \tag{4.4}$$

$$\{\delta u_e(y,t)\} = \begin{bmatrix} \delta u_{e,1}(t) & \delta u_{e,2}(t) \end{bmatrix}^T \tag{4.5}$$

Using the shape functions and the Galerkin assumption of equal shape and weight functions, the internal displacements can then be described by:

$$u(y_e,t) = \{\Phi(y_e)\}\{u_e\} \tag{4.6}$$

$$\delta u(y_e,t) = \{\Phi(y_e)\}\{\delta u_e\} \Leftrightarrow \delta u(y_e,t) = \{\delta u_e\}^T\{\Phi(y_e)\}^T \tag{4.7}$$

$$\{\Phi(y_e)\} = \begin{bmatrix} 1-\frac{y_e}{l_e} & \frac{y_e}{l_e} \end{bmatrix} \tag{4.8}$$

where

$\{\Phi(y_e)\}$	Element displacement interpolation vector

The discretized weak form is then:

$$\begin{aligned}&\int_{y_{e,1}}^{y_{e,2}} \{\delta u_e\}^T \frac{\partial\{\Phi(y_e)\}^T}{\partial y} EA \frac{\partial\{\Phi(y_e)\}^T}{\partial y}\{u_e\}^T dy \\ &\quad + \int_{y_{e,1}}^{y_{e,2}} \{\delta u_e\}^T\{\Phi(y_e)\}^T \rho A\{\Phi(y_e)\}\frac{\partial^2\{u_e\}}{\partial t^2}dy \\ &= \left[\{\delta u_e\}^T\{\Phi(y_e)\}^T N_e(y_e,t)\right]_{y_{e,1}}^{y_{e,2}} + \int_{y_{e,1}}^{y_{e,2}} \{\delta u_e\}^T\{\Phi(y_e)\}^T p(y,t)dy\end{aligned} \tag{4.9}$$

$$N_e(y_e,t) = EA\frac{\partial\{u_e\}^T\{\Phi(y_e)\}^T}{\partial y} \tag{4.10}$$

$\{\delta u_e\}$ is arbitrary but not $\{0\}$ and since the shape functions are invariant in time, the equation of motion can be rewritten as:

$$\begin{aligned}&\{\delta u_e\}^T \int_{y_{e,1}}^{y_{e,2}} \frac{\partial\{\Phi(y_e)\}^T}{\partial y} EA \frac{\partial\{\Phi(y_e)\}^T}{\partial y} dy \{u_e\}^T \\ &+ \{\delta u_e\}^T \int_{y_{e,1}}^{y_{e,2}} \{\Phi(y_e)\}^T \rho A \{\Phi(y_e)\} dy \frac{\partial^2\{u_e\}}{\partial t^2} \\ &= \{\delta u_e\}^T \left[\{\Phi(y_e)\}^T N_e(y_e,t)\right]_{y_{e,1}}^{y_{e,2}} + \{\delta u_e\}^T \int_{y_{e,1}}^{y_{e,2}} \{\Phi(y_e)\}^T p(y,t) dy\end{aligned} \tag{4.11}$$

$$\begin{aligned}\Rightarrow &\int_{y_{e,1}}^{y_{e,2}} \frac{\partial\{\Phi(y_e)\}^T}{\partial y} EA \frac{\partial\{\Phi(y_e)\}^T}{\partial y} dy \{u_e\}^T + \int_{y_{e,1}}^{y_{e,2}} \{\Phi(y_e)\}^T \rho A \{\Phi(y_e)\} dy \frac{\partial^2\{u_e\}}{\partial t^2} \\ &\quad = \left[\{\Phi(y_e)\}^T N_e(y_e,t)\right]_{y_{e,1}}^{y_{e,2}} + \int_{y_{e,1}}^{y_{e,2}} \{\Phi(y_e)\}^T p(y,t) dy\end{aligned} \tag{4.12}$$

Element matrices

The equation of motion can be written as:

$$[K_e]\{u_e\} + [M_e]\frac{d^2\{u_e(t)\}}{dt^2} = \{p_e(t)\} + \{b_e(t)\} \tag{4.13}$$

where

$$[K_e] = \int_0^{l_e} \frac{\partial\{\Phi(y_e)\}^T}{\partial y_e} EA \frac{\partial\{\Phi(y_e)\}}{\partial y_e} dy_e = \frac{EA}{l_e}\begin{bmatrix} 1 & -1 \\ -1 & 1 \end{bmatrix} \tag{4.14}$$

is the element stiffness matrix,

$$[M_e] = \int_0^{l_e} \{\Phi(y_e)\}^T \rho A \{\Phi(y_e)\} dy_e = \frac{\rho A l_e}{6}\begin{bmatrix} 2 & 1 \\ 1 & 2 \end{bmatrix} \tag{4.15}$$

is the element mass matrix,

$$\{p_e(t)\} = \int_0^{l_e} \{\Phi(y_e)\}^T p(y_e + y_{e,1}) dy_e \tag{4.16}$$

is the consistent nodal load vector and

$$\{b_e(t)\} = \left[\{\Phi(y_e)\}^T N(y_e + y_{e,1}, t)\right]_0^{l_e} = \begin{bmatrix} N_{e,1} \\ N_{e,2} \end{bmatrix} \tag{4.17}$$

is the boundary load vector.

Cook et al. [2002] argues that a so-called combination matrix of a completely lumped and consistent mass matrix often better matches the actual eigenvalues of the system in dynamic analysis compared to the consistent one (Equation (4.15)). This is especially true for higher modes, where consistent mass matrices tend to overestimate the natural frequencies and lumped tend to underestimate them. The element mass matrix in the present project is therefore calculated according to the suggestion of Cook et al. [2002] as:

$$[M_e] = \frac{A\rho l_e}{6}\begin{bmatrix} 3-\beta_m & \beta_m \\ \beta_m & 3-\beta_m \end{bmatrix} \tag{4.18}$$

where

β_m	Mass lumping parameter, default $\beta_m = 0.5$

To include the energy dissipation induced by structural damping, the equation of motion is expanded to:

$$[K]\{u\} + [C]\frac{d\{u(t)\}}{dt} + [M]\frac{d^2\{u(t)\}}{dt^2} = \{p(t)\} + \{b(t)\} \tag{4.19}$$

where $[C]$ is the damping matrix. The physical damping is assumed to be in the form of Rayleigh damping:

$$[C] = \alpha\,[M] + \beta\,[K] \tag{4.20}$$

where

α, β	Rayleigh coefficients, $\alpha \geq 0$, $\beta \geq 0$

Rayleigh damping is frequency-dependent, as seen in Figure 4.3. The nature of the Rayleigh damping ensures the diagonality of the damping matrix. The stiffness-dependent Rayleigh damping tends to damp high modes most and the mass-dependent Rayleigh damping damps low modes most. Stiffness-dependent damping is sometimes used to forcibly dampen out numerical noise in simulations [Cook et al., 2002]. As seen in Figure 4.3, minimum damping at a certain frequency can be obtained. This frequency is approximated as the natural frequency of the pile with regards to the stress waves, i.e. the frequency of a stress wave in a fixed-free rod:

$$f_0 = \frac{c_0}{4L} \tag{4.21}$$

where

L	Pile length

The Rayleigh coefficients can then be found at the minimum by:

$$\alpha = \zeta_{min} 2\pi f_0 \quad , \quad \beta = \frac{\zeta_{min}}{2\pi f_0} \tag{4.22}$$

where

ζ_{min}	Dimensionless damping ratio at minimum damping

The minimum damping ratio at the first natural frequency is most accurately determined by experiment. This is not possible in the present project and it is instead estimated according to Chopra [1995, Table 11.2.1] to be 2-3% at low stress levels and 3-5% at high stress levels. It is assumed to be $\zeta_{min} = 0.05$. The resulting damping ratios for various pile lengths can be seen in Figure 4.4.

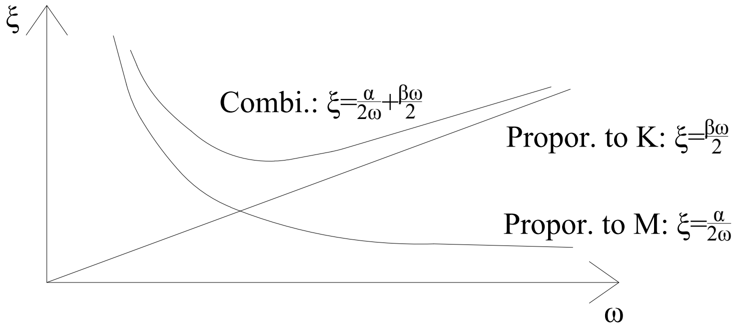

Figure 4.3. Frequency dependency of damping for various Rayleigh damping configurations. Reproduced from Chopra [1995].

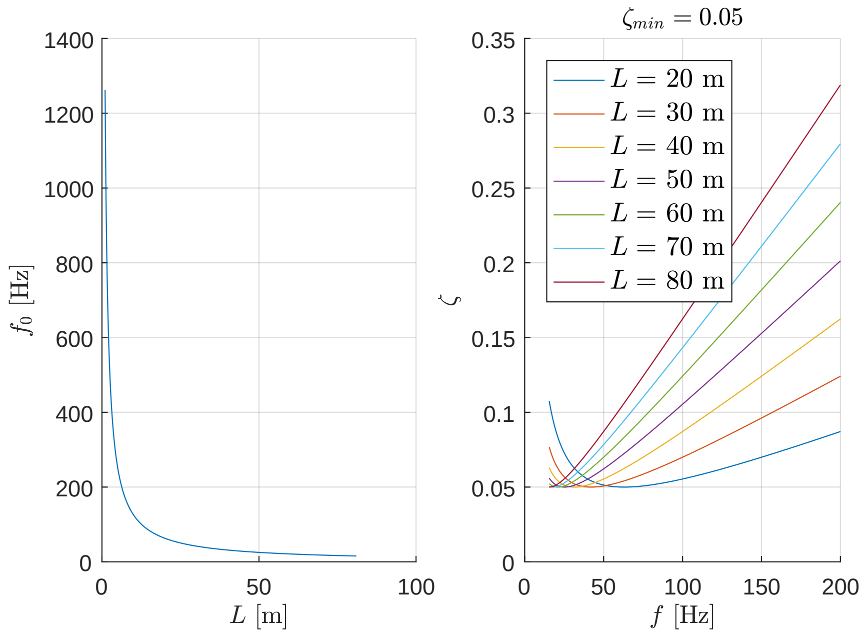

Figure 4.4. Natural frequency of wave propagation for various pile lengths (left), and assumed structural damping ratios versus frequency for various pile lengths (right).

Assembly

When the local element matrices have been calculated, the global system of equations is obtained by adding the contributions for all shared nodes, which in the case of the linear element naturally is all nodes expect the ends. The global system of equations of motion can then be written in the standard form as:

$$[K]\{u(t)\}+[C]\{\dot{u}(t)\}+[M]\{\ddot{u}(t)\}=\{f(t)\} \tag{4.23}$$

To avoid instability and imprecise distribution of changes in impedance over physical segment boundaries, a change in cross section will result in a change in element in the finite element model. Thus, all mass, stiffness and damping properties are constant within an element.

Nodal forces and boundary conditions

As shown in Figure 2.2 there are no displacement boundary conditions. A set of nodal force conditions are imposed on the system:

- The self-weight of the pile f_g
- The soil resistance to driving is distributed in the relevant nodes

As the unit mass per element is constant, the contribution to the global self-weight vector can for each element be calculated as:

$$\{f_{e,g}\} = \frac{l_e A \rho g}{2} \begin{bmatrix} 1 \\ 1 \end{bmatrix} \tag{4.24}$$

The skin friction and tip resistance is calculated independently and integrated in order to provide nodal values. This is described in Section 4.2.

Solution and post-processing

The transient response of the system is solved using a specific solution algorithm as described in Section 4.4.2. After each time step has passed the normal strain and stress in each element is evaluated as:

$$\varepsilon_e = \frac{u_{e,2} - u_{e,1}}{l_e} \quad , \quad \sigma_e = E \varepsilon_e \tag{4.25}$$

This is done in order to check whether there is a risk of the pile becoming plastic, which will terminate the solution process as this is both violating the elastic assumption and normally not allowed in pile installation.

4.2 Soil resistance model

The most important part of the pile driving problem is the soil resistance model. As discussed earlier, the total soil resistance is assumed to be comprised of a static or "stiffness" contribution, i.e. dependent on displacement, and a dynamic or "damping" contribution, i.e. dependent on velocity. These forces must be included in the equation of motion.

The resistance from the soil on movement can be viewed as an "internal" force in the sense that it adds to the stiffness and damping of the system. To exemplify, the internal force vector of the entire pile can, if the dimensionless damping exponent n is assumed to be one and the soil stiffness and damping assumed to be constant, be expressed in a general sense as:

$$\begin{aligned} \{F_{int}\} = & \int_L [\Phi]^T f_s \Omega dy + \int_L [\Phi]^T f_s \Omega J [\Phi] \{v\} dy + \int_L [B]^T (EA) [B] dy \{u\} \\ & + [q_{tip} A_{end}] \hat{1}_{toe} + [q_{tip} A_{end} J_{toe} v_{end}] \hat{1}_{toe} \end{aligned} \tag{4.26}$$

where

F_{int}	Internal force vector
L	Pile length
f_s	Static side friction per unit area, $f_s(y,u)$
Ω	Relevant pile circumference
J	Side Smith damping coefficient
$\{v\}$	Nodal velocity vector
σ	Tip resistance per unit area, $\sigma(u_{end})$
A_{end}	Pile end cross-sectional area
J_{toe}	Toe Smith damping coefficient
$\hat{1}_{toe}$	Column vector with unity in last row and zero everywhere else
$[B]$	Strain interpolation matrix
$\{u\}$	Nodal displacement vector

Examining Equation (4.26), the stiffness matrix $[K]$ is identified as $\int\limits_L [B]^T\,(EA)\,[B]\,dy$, which means that the tangential soil stiffness matrix can be identified as:

$$[K_{soil}(u,v,t)] = \frac{\partial}{\partial\{u\}}\left(\int\limits_L [\Phi]^T f_s\Omega(1+J\,[\Phi]\,\{v\})\,[\Phi]\,dy + [q_{tip}A_{end}(1+J_{toe}v_{end})]\,\hat{1}_{toe}\right) \tag{4.27}$$

$$[K_{total}] = [K] + [K_{soil}(u,v,t)] \tag{4.28}$$

and similarly, the tangential soil damping matrix can be identified as:

$$[C_{soil}(u,v,t)] = \frac{\partial}{\partial\{v\}}\left(\int\limits_L [\Phi]^T f_s\Omega(1+J\,[\Phi]\,\{v\})\,[\Phi]\,dy + [q_{tip}A_{end}(1+J_{toe}v_{end})]\,\hat{1}_{toe}\right) \tag{4.29}$$

$$[C_{total}] = [C] + [C_{soil}(u,v,t)] \tag{4.30}$$

The partial derivatives are not easily approximated for complicated resistance models, which means that the explicit force of Equation (4.26) or independently evaluated is more versatile in a general formulation. The solution algorithm in the present project (described in Section 4.4.2) uses the soil resistance explicitly (and not Equations (4.27) and (4.29)) in the calculations.

This has the advantage of easy implementation of any soil resistance model in all details (as it may be evaluated independently of the pile model in each discrete soil node), and, more importantly, eliminating the need for recalculating the stiffness and damping matrices to account for soil resistance, which greatly improves solution efficiency. Furthermore, three distinct discretization schemes may be chosen for pile, side resistance and tip resistance, which is valuable in the sense that:

- The stress waves in the pile has large wavelengths and only few finite elements (say 1 element per 5-10 m) is necessary to represent this variation
- The side resistance is generally dependent on local soil parameters, and must thus possess a much finer discretization (for instance 1 soil node per 1 m), but is less dependent on the local conditions as compared to the tip resistance.

- The tip resistance is highly dependent on the current position of the tip and the governing soil parameters in that position. Much finer node spacing (say 2-10 cm) for this calculation seems more appropriate.

4.2.1 Modelling considerations

Generally, the SRD is dependent on current permanent pile penetration, relative displacement and relative velocity between pile and soil. As the soil some distance from the pile is stationary, the two latter equals the displacements and velocities calculated in the pile model. This entails assuming that all the phenomena in the pile-soil interface is completely described by the SRD model. The SRD model generally delivers a force that is non-linearly dependent on displacement and velocity.

The total soil resistance is assumed to be of the general form described in Chapter 3, meaning that a static resistance R_s is the governing factor, related to both displacement and velocity through a quake and a Smith damping factor as described by Equation (3.1). The soil node displacements are for ease of interpolation measured relative to $z = 0$, and thus the quake at depth z is defined as $q_{i,total}(z) = q_{i,local} + z$. This can be illustrated by Figure 4.5, where it can be seen that a larger *total* quake is defined at greater depth as a larger displacement relative to the surface is required for the soil to go plastic.

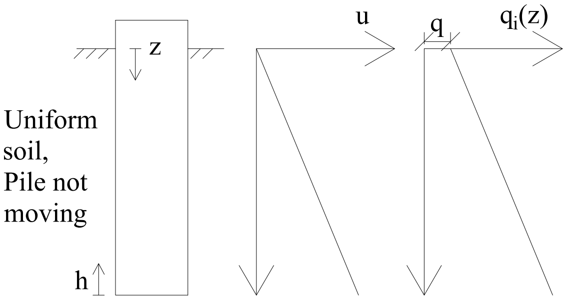

Figure 4.5. Definition of displacements and total quakes.

For simplicity, side friction is described in the following, as the tip resistance is accounted for separately.

A diagram of the general implementation of a SRD model for side friction can be seen in Figure 4.6 with supplementary information in Figure 4.10. Any model parameter from the pile system equations such as pile properties, displacement, velocities and accelerations can be transferred back and forth. For illustration an implementation of the Alm & Hamre model (see Section 3.1.4) is used in this description. The total resistance is dependent on:

- Constant soil properties: Cone resistance q_c, friction angle φ, overburden pressure σ'_{v0}, atmospheric pressure p_a
- Constant model properties: Skin quake q, toe quake q_{toe}, skin damping factor J, toe damping factor J_{toe}, damping exponent n
- Dynamic model parameters: displacement in soil u_s, velocity in soil v_s, current pile penetration p

As seen in Figure 4.6, the soil properties are discretized in a number of points to some depth larger than the desired installed penetration. It makes little sense to apply variable soil node spacing due

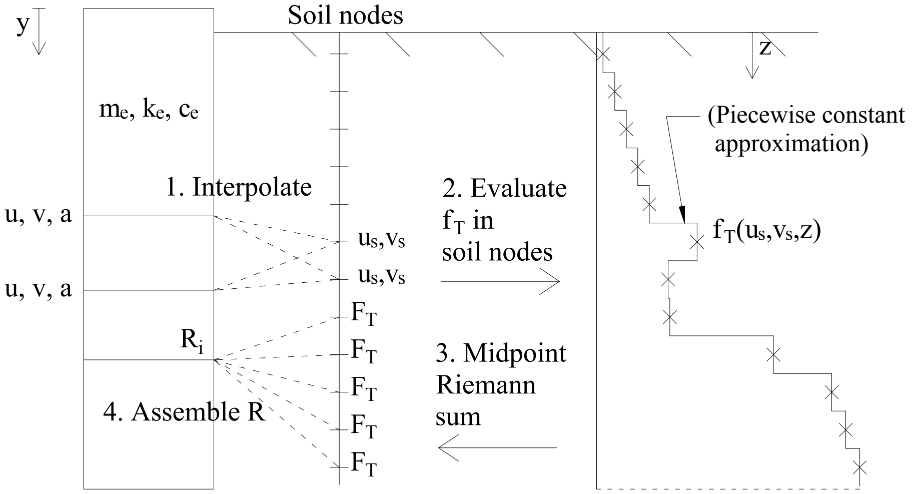

Figure 4.6. Simplified schematic of implementation of interpolation and soil resistance evaluation/integration model.

to the progressive nature of the system.

Large differences in cone resistance and friction angles and thus the most important soil properties used in an SRD model typically occur at major stratum boundaries. See Figure 4.7 for an example of clear strata boundaries. Minor strata (of depth of less than ≈ 1 m) have small impact on pile driving, unless they are penetrated and are highly cohesive. Physically, this suggest that the spacing of soil nodes should be chosen at least fine enough to capture major soil changes within a reasonable accuracy. If no clear stratigraphy is present and the strength increases monotonically or stays quasi-constant, a much larger spacing can be chosen.

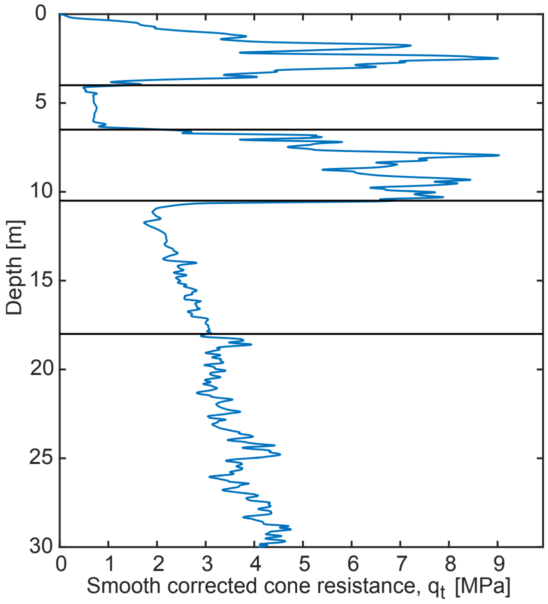

Figure 4.7. Example of cone resistance profile with somewhat clearly defined stratum boundaries and need for fine node spacing (upper three layers), and less clearly defined layer boundary (if any) between the two lower layers and no need for particularly fine node spacing.

Several of the SRD models presented in Chapter 3 involves friction fatigue. This is an important parameter regarding pile driving, as it can have significant influence on the resulting soil resistance. For the Alm & Hamre model as an example, this involves an exponentially decaying friction degradation function. As the skin resistance is only evaluated at the soil nodes, the spacing should be chosen accordingly small in order to accurately capture this variation, as illustrated by Figure 4.8.

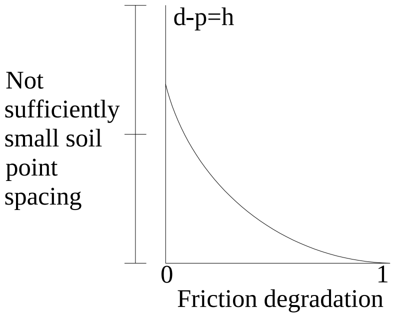

Figure 4.8. Example of badly chosen soil node spacing with regards to friction fatigue.

In an average sense, the local variations of the skin friction are small compared to the total soil resistance at a given penetration. However, the tip resistance is not an averaged parameter (while the cone tip resistance may be an averaged value), and is thus much more variable and sensitive to sudden changes in soil properties. Because of this, two soil node discretization systems have been adopted:

- Fine spacing Δz_p in the tip resistance coordinate system
- Several times larger spacing Δz in the side friction coordinate system

The choice of soil node spacing should be based on the soil profile:

- If clearly defined shallow layers and non-linear variations in the soil profile is observed (e.g. upper three layers in Figure 4.7), a very fine tip discretization should be used. Furthermore, if the soil profile implies very large side resistance (e.g. large overburden pressure and friction angle) in a relative shallow layer compared to final penetration, the side friction discretization should be chosen so that at least four soil nodes (in order to capture both stratum boundaries) are contained within the layer.
- If most layers are deep and fairly continuous across stratum boundaries which may or may not be clearly defined (e.g. lower two layers in Figure 4.7), a relatively large tip and even larger side friction spacing can be chosen, given that the friction fatigue degradation factor is sufficiently well described.

In the program implementation used, all soil properties are specified in the z_p discretization. If z is not a multiple of z_p, linear interpolation is applied.

4.2.2 Numerical procedures (soil)

The soil model consists of several steps, some performed once, some at each discrete time interval and some at each solution iteration. The overall procedure for obtaining nodal values of the driving resistance is:

- Initially, a structure of soil constants based on input is calculated, which for each soil node describes the relevant constants such as q_c, δ_{cv}, σ'_{v0}, damping and quake values. Furthermore, the resistance model specific strength parameters $f_{s,i}$, $f_{s,res}$ and k are calculated.
- For each time step, the current pile penetration is used to update the soil structure by calculating the degradation factor (for example $\exp(k(z-p))$ in the Alm & Hamre model) and effective maximum unit skin resistance of each node.
- For every iteration:
  - A routine is used to identify the two pile DOF closest to each soil node and whether the individual soil nodes are currently situated in a pile element interior. The Lagrange shape functions is then used to determine the "soil" displacements u_s and velocities v_s in these "activated" soil nodes.
  - Looping over activated soil nodes, the local unit skin resistance is calculated according to Equation (3.1) (see Figure 4.10) and the mentioned assumptions.
  - The total skin resistance is obtained using Riemann integration with the appropriate integration weights and local pile circumferences. Using the Lagrangians of Figure 4.2, the nodal values of the integrated skin friction is obtained.
  - The soil node in the tip discretization system just above and the node just below the pile tip are identified and the parameters in these two nodes are interpolated to the pile tip, where the penetration and pile tip velocity is used directly for calculation of the tip resistance.

Identifying activated soil nodes

Given that the coordinate of the pile is y, the coordinates relative to the ground surface of the activated pile nodes can be found by the transformation:

$$y_s = y - (y_{tip} - p) \tag{4.31}$$

where only $y_s \geq 0$ is considered and p is the current pile penetration. The coordinates of the soil nodes are denoted z_s and a routine is employed to identify whether $y_{s,i} \leq z_{s,j} < y_{s,i+1}$ for all pile coordinates $\{y_{s,1}, ..., y_{s,i}, ..., y_{s,tip}\}$. This results in vector $\{z_s\}$ of soil node coordinates. The displacements $\{u_s\}$ and velocities $\{v_s\}$ of the activated soil nodes are then calculated as:

$$\begin{bmatrix} u_{s,j} \end{bmatrix} = \begin{bmatrix} \dfrac{y_{s,i+1} - z_{s,j}}{y_{s,i+1} - y_{s,i}} & \dfrac{z_{s,j} - y_{s,i}}{y_{s,i+1} - y_{s,i}} \end{bmatrix} \begin{bmatrix} u_i & u_{i+1} \end{bmatrix}^T \tag{4.32}$$

$$\begin{bmatrix} v_{s,j} \end{bmatrix} = \begin{bmatrix} \dfrac{y_{s,i+1} - z_{s,j}}{y_{s,i+1} - y_{s,i}} & \dfrac{z_{s,j} - y_{s,i}}{y_{s,i+1} - y_{s,i}} \end{bmatrix} \begin{bmatrix} v_i & v_{i+1} \end{bmatrix}^T \tag{4.33}$$

Evaluation of unit soil resistance in soil nodes

Regarding the skin friction, a slight modification of the basic Smith model is applied. Because the reaction of the individual soil nodes is governed by a varying strength f_s, the stiffness also changes non-linearly depending on actual displacement. The Alm & Hamre model assumes an exponential decay in strength depending on relative penetration h as described in Chapter 3.

The loading and unloading stiffness is in accordance with Pile Dynamics [2010] assumed identical (this can however easily be changed if needed). Likewise, both positive and negative damping is assumed to have the same shape, with the total resistance being:

$$f_t = \mathrm{sgn}(v_s)\left(f_s + |f_s|J|v_s|^n\right) \tag{4.34}$$

A certain amount of stiffness regeneration is expected, and due to this a stiffness regeneration factor $0 < \kappa \leq 1$ is assumed. Because the displacements as obtained from the pile model are *total* values, the quake is linearly increasing with depth as explained in Section 4.2.1. For any given point along the force-displacement curve seen in Figure 4.9, upper (initial *i*) and lower bounds on the stiffness can be estimated as:

$$k_0 = \frac{f_{s,i}}{q} \quad , \quad k_s = \frac{f_s}{q} \tag{4.35}$$

The actual stiffness depend on a number of things, e.g. the local variations in elastic yield limit and also the relative displacement. The correct relation between the physical parameters and the instantaneous local stiffness is not well defined and must thus be modelled within these bounds, which is done as:

$$k = \frac{1}{2}\left(\frac{f_{s,i}}{q}\kappa + \frac{f_s}{q}(1-\kappa)\right) \tag{4.36}$$

where $\kappa \to 1$ results in little plasticity and $\kappa \to 0$ gives strong dependence on current yield limit, i.e. progressively plastic behaviour. κ in sands must for calibration purposes therefore be related to relative density, which may be estimated from CPT measurements. As dense sands is the main focus of this project, a default value of $\kappa = 0.8$ is assumed unless otherwise stated.

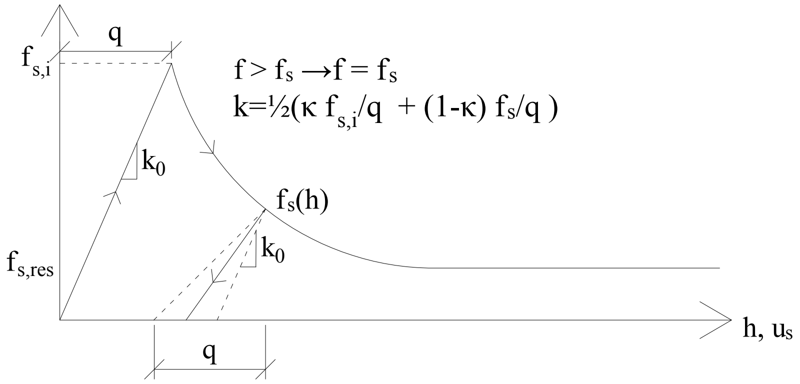

Figure 4.9. Assumed strength-stiffness relations in evaluation of skin friction at a specific depth, i.e. a different graph exist for different depths, because both the total quake and the stiffness changes.

Figure 4.10 shows the principle (simplified) of how the side friction is calculated along the pile. The displacement and velocities in soil nodes are found from interpolation of the nodal values. Each soil node has an associated integration weight equal to node spacing except for the last one, for which two possible configurations exist:

- The pile tip is situated exactly at a soil node
- The pile tip is situated in between the two soil nodes just above (in pile interior) and just below the pile tip (outside of pile interior)

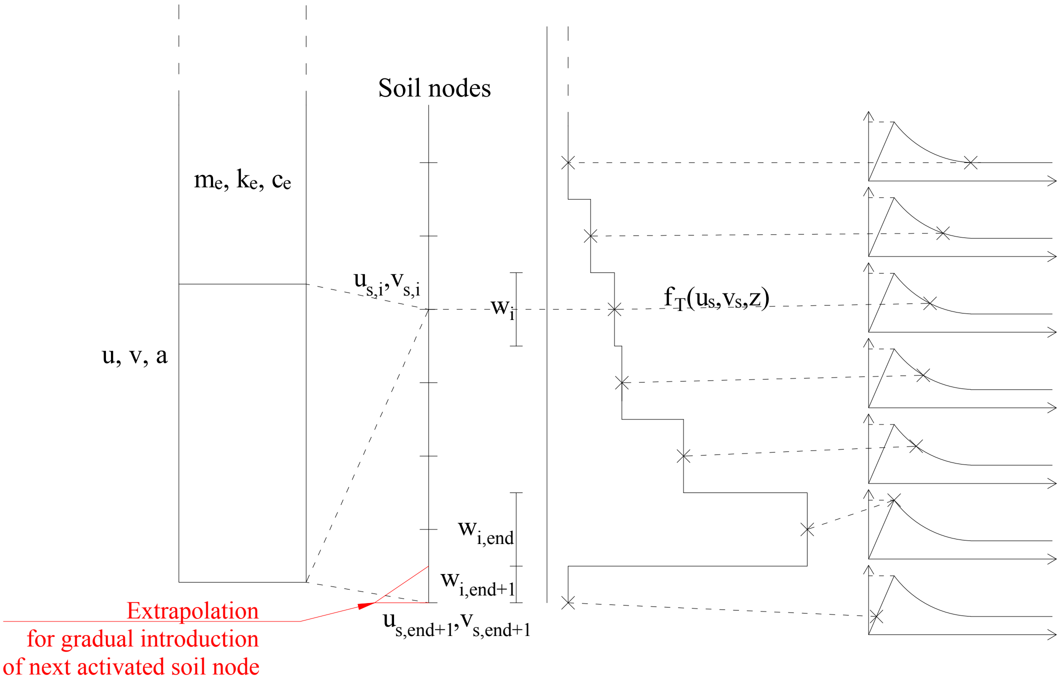

Figure 4.10. Illustration of calculation of skin resistance distributions. The displacement-resistance curves shown to the right is in reality different for each depth, but are for illustration purposes shown here as identical.

If the pile tip is situated in between two soil nodes and at a distance greater than halfway to the soil node just below the pile tip, the soil node below the pile tip is also partly activated. A Lagrangian equal to 0 at the halfway point and 1 at the soil node below the pile tip is used to extrapolate the pile tip displacement and velocity to this soil point as seen in Figure 4.10. This is done in order avoid "jumps" in the side friction because of the sudden inclusion of a soil node if the pile tip surpasses it. Using this approximation, the integration weight of the soil node just below the pile tip is found as the coordinate of this point minus the penetration.

Once the skin friction in all activated soil points has been calculated, an integration scheme is applied to calculate total skin friction.

Skin friction integration

In order to calculate the pile nodal reactions to the skin resistance, nodal values must be calculated for each element as:

$$F_e = \int_0^{l_e} \{\Phi\} f_t dy \tag{4.37}$$

The found skin resistance f_t is discontinuously distributed throughout all individual soil nodes.

It is possible to interpolate linear variation between soil nodes with a $J-1$ order Lagrange polynomial where J is number of soil nodes, but due to the non-linear dependence on both depth, displacement and velocity, an approximate continuous Lagrange polynomial interpolation containing the values of all the soil nodes, either along the entire pile or within individual finite elements, may likely be of very high order (higher than number of soil nodes), altering the shape of the interpolated distribution to be different from the physical.

If one despite this assumes a Lagrange polynomial may be obtainable, a non-physical discontinuity may still arise at pile element ends. Furthermore, the additional effort required to create a soil resistance distribution of appropriate (and unknown beforehand) order for every single iteration and time step can potentially be significant.

Had a single continuous polynomial of order n been obtainable, Gauss quadrature of order $2n-1$ could be utilised in order to obtain a fast, exact solution of this integral [Kreyszig et al., 2011]. Alternatively, a simple midpoint Riemann sum at the location of the soil nodes can be performed (see Figure 4.6), which is adopted in this project.

The contribution to the nodal values of the soil resistance from an element spanning node $j=1$ to $j=2$ can with the midpoint rule be found as:

$$\begin{bmatrix} r_1 \\ r_2 \end{bmatrix} = \begin{bmatrix} \{N_{1,i}\} \\ \{N_{2,i}\} \end{bmatrix} \{f_{t,i}W_{mid,i}C_e\} \tag{4.38}$$

where

$\{N_{1,i}\}$, $\{N_{2,i}\}$	Vectors of values of displ. interpolation matrix at soil nodes
$\{f_{t,i}W_{mid,i}C_e\}$	Vector of values of product of resistance, interval lengths and pile element circumference

Evaluation of tip resistance

The pile tip resistance is likewise non-linearly dependent on displacement and velocity. A force-displacement relation and damping contribution similar to the side resistance is in lack of better knowledge assumed for the tip resistance:

$$R_{tip} = \begin{cases} 0 & \text{for} \quad v_{end} < 0 \quad \text{(pile tip moving upwards)} \\ A_{end} q_{tip} \dfrac{u_{end}}{q_{toe}} \left(1 + J_{toe} v_{end}^n\right) & \text{for} \quad v_{end} > 0 \quad , \quad 0 < u_{end} < q_{toe} \\ A_{end} q_{tip} \left(1 + J_{toe} v_{end}^n\right) & \text{for} \quad v_{end} > 0 \quad , \quad u_{end} > q_{toe} \end{cases} \tag{4.39}$$

where

u_{end}, v_{end}	Displacement and velocity of last pile DOF
q_{tip}	Unit tip resistance (at current penetration) according to SRD model
$q_{toe,k}$	Assumed elastic deformation limit of soil (quake), toe (at current penetration)
$J_{toe,k}$	Smith damping coefficient, toe (at current penetration)

It is seen that a unique set of quake and damping parameters exist for the tip resistance, which is similar to the approach used in the derivation of the SRD models reviewed in Chapter 3.

q_{tip} can be found according to any of the SRD models, for example according to the Alm & Hamre model:

$$q_{tip} = 0.15 q_c \left(\frac{q_c}{\sigma'_{v0}}\right)^{0.2} \tag{4.40}$$

The SRD model parameters are interpolated to the current penetration using Lagrangians, and the displacement and velocity at the end is simply taken directly from the end node of the pile model.

4.3 Hammer model

As part of any analysis of the dynamic response of a hammer-pile-soil system, it is necessary to model the dynamic force generated by the hammer impact.

4.3.1 Hydraulic pile hammers

A diagram of the basic hydraulic hammer system can be seen in Figure 4.11. From this it is seen that the hammer system is mounted to the pile and that the moving ram can be accelerated to more than g by the pressure build-up in the chamber generated when the ram is lifted (containing either air, some inert gas or oil).

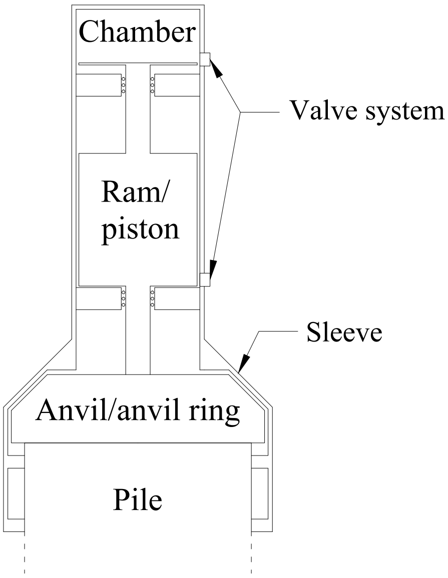

Figure 4.11. Basic principle of a hydraulic hammer type pile driver according to IHC Merwede [2017].

The data available in the design phase is usually limited to pile make-up, ram and total hammer weights and maximum and minimum energy deliverable to the pile head, sometimes including anvil, cushion systems etc. The hammer has a computer-controlled hydraulic system which automatically adjust hydraulic pressure, stroke and valve timing in order to control the impact energy [IHC Merwede, 2017]. This is due to the fact that any combination of hydraulic pump with a specific capacity, efficiency and power supply to a hammer with a specific valve flow rate, ram weight and cushion has an optimal blowrate and stroke for maximum driving efficiency and minimum power consumption.

The kinetic energy transferred to the anvil is adjusted during ramming so that the pile is not driven unintentionally fast or slow.

4.3.2 Load series characteristics

A typical impact duration is $\approx 40\,\text{ms}$. The optimal blowrate for large hydraulic hammers is typically 40-60 blows/min., and the load magnitude is thus zero for most of the driving time.

The penetration rate is ultimately governed by the magnitude, duration and shape of the force pulse in the pile. Furthermore, the soil properties and penetrated length of the pile influences whether the pile is point-bearing or tends toward being a friction pile, which has a large influence on the optimal shape of the force pulse [Parola, 1970].

Parola [1970] states that it is reasonable to regard the individual blows as completely independent. Thus, the problem limits to a question of reasonable modelling of the pile head force during individual blows and not necessarily a complete model of the entire ram motion. This assumption is based on the shape seen in Figure 4.12, where the independence assumption can be seen to be appropriate.

Figure 4.12 shows the characteristics of a typical hammer blow:

1. The initial increase in force is due to the hammer impacting the pile head
2. This generates a stress wave, which travels downwards
3. The wave is reflected at the pile tip
4. Upon returning to the pile head the wave will reflect down again, reduced in magnitude, due to the weight of the hammer auxiliaries such as sleeve, hammer assembly etc.

The secondary impulse can be important depending on the total amount of soil damping and therefore the current penetration. The stress wave may oscillate several times if very little soil resistance is present. Furthermore, the number of oscillations depends on the mechanical properties of the ram, anvil and pile head. In general however, the number of oscillations is limited to one or two unless driving in very stiff soils at small depths.

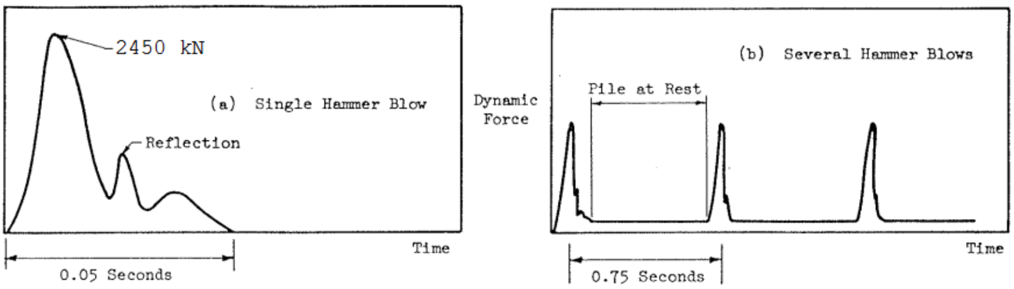

Figure 4.12. Example of load measurements in a pile head. Modified from Parola [1970].

4.3.3 Discussion of existing hammer models

The literature contains many more or less complex models of the hammer impact, of which only a few will be briefly discussed here.

Historically (and in GRLWEAP), the force-time signal is not computed directly, but an extension to the numerical model is applied instead. Smith [1960] proposed a model where all the components of the driving system is lumped masses, and the motion is governed by a set of springs/dashpots analogously to the pile model presented in Section 2.2. This driving system model is then simply appended to the top pile element. This driving system model has been extended to account for more and more complex sub-models with the intention of modelling more and more complex driving systems, i.e. diesel, hydraulic and vibratory hammers of all kinds and dimensions [Deeks and Randolph, 1993] [Pile Dynamics, 2010]. The drawback of this approach is that for the entire simulation, the actual driving system geometry, internal friction, damping, hydraulic pressure variations and all losses in the driving accessories must be modelled directly somehow. All losses which can not be included directly must be either approximated via empirical (and in reality varying) *energy efficiency factors*.

Parola [1970] used a model where the ram mass impacts a spring, which delivers a force to a lumped-mass anvil, which is simply fixed to the pile head. The model is used to compare and evaluate the effectiveness of a wide variety of cushion materials for small-diameter piles using drop hammers, but uses an array of rather non-physical parameters and coefficients in order to achieve this, some of which are non-scalable to larger piles and ram masses.

Deeks and Randolph [1993] recognised that analytical derivations of the force-time signal has advantages regarding easy implementation in driveability analysis and quick parametric studies, and derives a sophisticated multi-degree-of-freedom model, which incorporates the pile material and geometry via the pile impedance. This model can account for separation of the hammer from the pile and energy losses in anvil/cushion, and is solved using Laplace transforms. The results are apparently accurate when compared to field measurements. The drawbacks of the analytical solution are:

- It is only valid for drop hammers (single-acting)
- It is only valid as long as the wave travel downwards, i.e. it is only valid for either long piles or short impact durations
- It is not independent on choice of non-dimensional anvil/cushion stiffness and damping, which in practice can only be determined from measurements
- It does not account for changes in pile cross-section and associated changes in impedance
- It does not in a sufficient way account for soil "impedance" (proportional to soil damping and quake, both of which are also uncertain), which will increase in significance with increase in penetration

Take et al. [1999] used a lumped-mass model similar to Deeks and Randolph [1993] but substituting a parallel (Kelvin) spring-dashpot system with a series (Maxwell) spring-dashpot system. This adds to the complexity of the model with another set of dimensionless parameters which are only obtainable through measurements. Instead of using Laplace transforms in the solution, a forth-order characteristic equation is instead found and solved using assumptions regarding the nature of the roots of this equation. All the limitations applicable to the solution of Deeks and Randolph [1993] are still present with essentially the same results.

4.3.4 Hammer model in present project

Middendorp and van Weele [1986] showed that if the force delivered to the pile head is modelled somewhat correctly, the precise properties of the driving system is not directly necessary for obtaining accurate driving simulation results.

Adopting that reasoning, an explicit "bare-minimum" model of the force-time response seems computationally desirable compared to modifying the system matrices analogously to the Smith approach, as the expected differences in properties of the driving system elements compared to the pile elements will greatly increase computation time for the entire system, with no guaranteed improvement in result quality. Furthermore, the analytical solutions have several drawbacks and no significant advantages over an approximate numerical model with regards to unknown parameters.

The goal is to represent the energy delivered by the hammer, as this is the specification available and because this number is what is controlled during driving to avoid damage to the equipment and/or pile. For older, purely mechanical, hammers such as winched drop hammers or single-acting hammers such as diesel hammers, the typical specification prescribed is the potential energy or simply the ram weight and stroke or all of these. For the hydraulic hammers, the typical specification is the kinetic energy delivered to the pile head [IHC Merwede, 2017].

It is important to recognize, that matching the *transmitted* energy to the pile head to measurements/specifications is not sufficient for modelling the response. If the effect of the "rebound" (the secondary or reflective force peak shown in Figure 4.12) is not included, considerable loss of energy is implied.

The hammer is modelled as a single-degree-of-freedom (SDOF) system as seen in Figure 4.13, where the ram mass is lumped in a single coordinate. It is connected to the pile via a spring-dashpot system. The spring-dashpot system represents the anvil and all losses in the driving system.

The ram mass possesses a certain kinetic energy at impact equivalent to the specified hammer energy for each blow. This is equivalent to specifying a velocity as initial condition for the mass in a dynamic system.

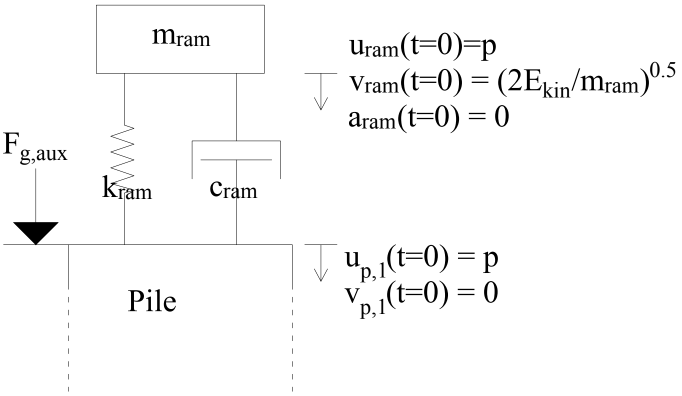

Figure 4.13. Illustration of hammer model assumed in the present project.

The spring element can only deliver a force when in compression. This force is specified as the boundary force on the first pile element and is obtained as:

$$f_{ram}(t) = k_{ram} u_{rel}(t) \tag{4.41}$$

where

$f_{ram}(t)$	Ramming force
k_{ram}	Ram system stiffness
$u_{rel}(t)$	$= u_{ram}(t) - u_1(t)$
$u_1(t)$	Displacement of first pile DOF according to pile model

Similarly to the displacement, the relative velocity is also specified in relation to the pile head as $v_{rel} = v_{ram} - v_1(t)$. u_{rel} and v_{rel} is updated at each time step, in order to account for movement of the pile head. The equation of motion of the ram mass is:

$$m_{ram}a_{ram}(t) + c_{ram}v_{rel}(t) + k_{ram}u_{rel}(t) = 0 \tag{4.42}$$

where

$a_{ram}(t)$	Ram acceleration, $a_{ram}(0) = 0$
$c_{ram}(t)$	Ram damping coefficient

By division with m_{ram}:

$$\begin{gathered} a_{ram} + 2\zeta_{ram}\omega_0 v_{rel}(t) + \omega_0^2 u_{rel} = 0 \\ \omega_0 = \sqrt{\frac{k_{ram}}{m_{ram}}} \quad , \quad \zeta_{ram} = \frac{c_{ram}}{2\sqrt{m_{ram}k_{ram}}} \end{gathered} \tag{4.43}$$

where

ω_0	First angular eigenfrequency
ζ_{ram}	Ram damping ratio

Several characteristic solutions of this equation exist, where $\zeta_{ram} = 0$ corresponds to an undamped system, $0 < \zeta_{ram} < 1$ an undercritically damped system (most real systems), $\zeta_{ram} = 1$ a critically damped system and $\zeta_{ram} > 1$ an overcritically damped system. The present system is assumed undercritically damped and a default value of 0.2 for the damping ratio may be appropriate.

If u_{rel} and v_{rel} can be found, Equation (4.42) can be solved readily for all instances. These quantities are however non-linear functions of pile and soil properties and are solved independently.

Instead, a discrete solution is sought for, which means that at any instant the solution at time step t is known and the solution at time step $t + \Delta t$ is sought for. This can be introduced as a sub-scheme not directly involving the pile-soil solution scheme which will be discussed in Section 4.4 below.

The solution can for example be approximated via the constant-acceleration Newmark equations (please refer to Equation (C.6) for the general formulation of the Newmark equations):

$$\begin{aligned}
a_{ram}(t+\Delta t) &= \frac{-c_{ram}\left(v_{rel}(t)+\Delta t a_{ram}(t)/2\right)}{m_{ram}} \\
&\quad \frac{-k_{ram}\left(u_{rel}(t)+v_{rel}(t)\Delta t+\Delta t^2 a_{ram}(t)/4\right)}{m_{ram}} \\
v_{rel}(t+\Delta t) &= v_{rel}(t)+\frac{\Delta t a_{ram}(t)\Delta t+a_{ram}(t+\Delta t)}{2} \\
u_{rel}(t+\Delta t) &= u_{rel}(t)+\Delta t v_{rel}(t)+\frac{\Delta t^2 a_{ram}(t)+\Delta t^2 a_{ram}(t+\Delta t)}{4}
\end{aligned} \tag{4.44}$$

With the initial conditions defined in Figure 4.13, the solution can simply march forward at each pile/soil model time step in order to provide the spring force at time step $t+\Delta t$.

The relative shape of the pulse is important, i.e. whether a long-duration, low-peak pulse or short-duration, high-peak pulse is assumed. This is dependent on the assumed hammer stiffness. Several different values for an example case has been examined in Section F.5.

Based on the findings of Parola [1970], which employed a similar hammer model, the hammer stiffness may possibly be in the range of 1×10^8 N/m to 1×10^{10} N/m. The damping ratio is presumed to be in the range of 0.1-0.4 due to the fact that the motion is most likely undercritically damped, but far from critically damped.

Gavrilov et al. [2016] stated a so-called "best-fit" value of $k_{ram} = 8\times10^9$ N/m, albeit for a somewhat small (compared to monopile drivers) hammer rated at 280 kJ for a simplified version of the analytical model proposed by Deeks and Randolph [1993]. Using that value, a 270 kJ impact yielded a force pulse of $\approx$ 12 ms duration and a peak value of 17.5 MN.

It is however emphasized that these values are modelling constants, i.e. assumptions, which can not be obtained precisely unless calibrated to field measurements. If the pulse duration, i.e. the time from impact to the ram bounce initiates, can be obtained, this can serve as the single calibration data necessary. Furthermore, the damping ratio and perhaps also the stiffness are in reality most likely not constants, but their dependence on various physical conditions are not clear.

Assuming an infinitely long, infinitely stiff pile, a parametric study on the value of the hammer stiffness and the damping ratio can be performed independent on specific pile and soil properties. A characteristic series of force, displacement and velocity when assuming a ram energy of $E_{kin} = 2$ MJ and ram mass of 100 t can be seen in Figure 4.14. It is seen that the ram is "shut off" when the ram displacement becomes negative, i.e. when the ram is moving upwards, and that the overall shape somewhat mimics the shape of Figure 4.12.

Regarding the resulting spectral distribution, the wavenumber can be defined according to Andersen [2006] as:

$$k = \frac{2\pi f}{c_0} \tag{4.45}$$

As the stress waves through the pile are assumed non-dispersive, the phase velocity may be seen as constant, and it is thus possible to plot a wavenumber spectrum based on the Fourier transform of the load series. This can seen for various values of ζ_{ram} (a critically damped example has been included for illustration) and k_{ram} in Figures 4.15 and 4.16. As expected, the impact duration decreases with stiffness and the peak force decreases with damping ratio. The lowest stiffness

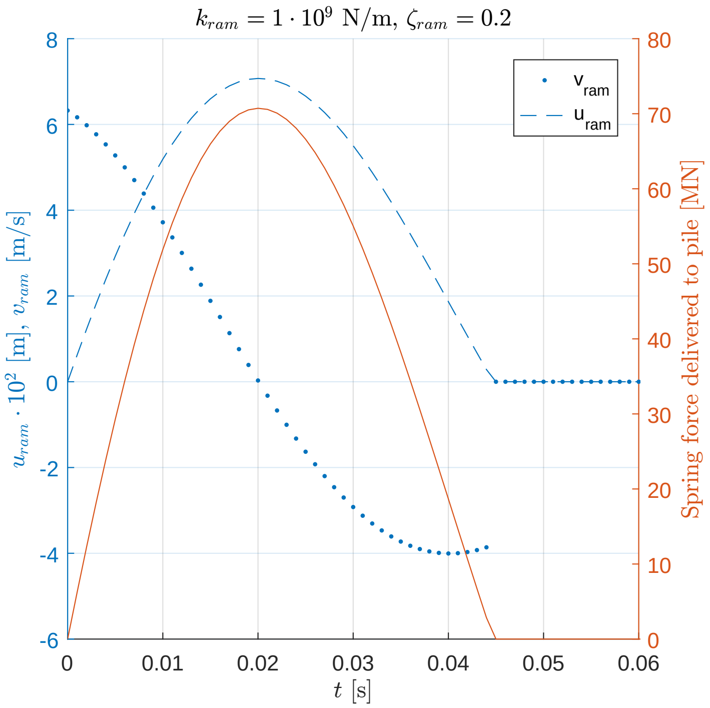

Figure 4.14. Example of force, displacement and velocity series as determined by hammer model assuming an infinitely long and infinitely stiff pile, a ram energy of $E_{kin} = 2$ MJ and ram mass of 100 t.

values seem to give too long impact durations, whereas the higher stiffness values give realistic results.

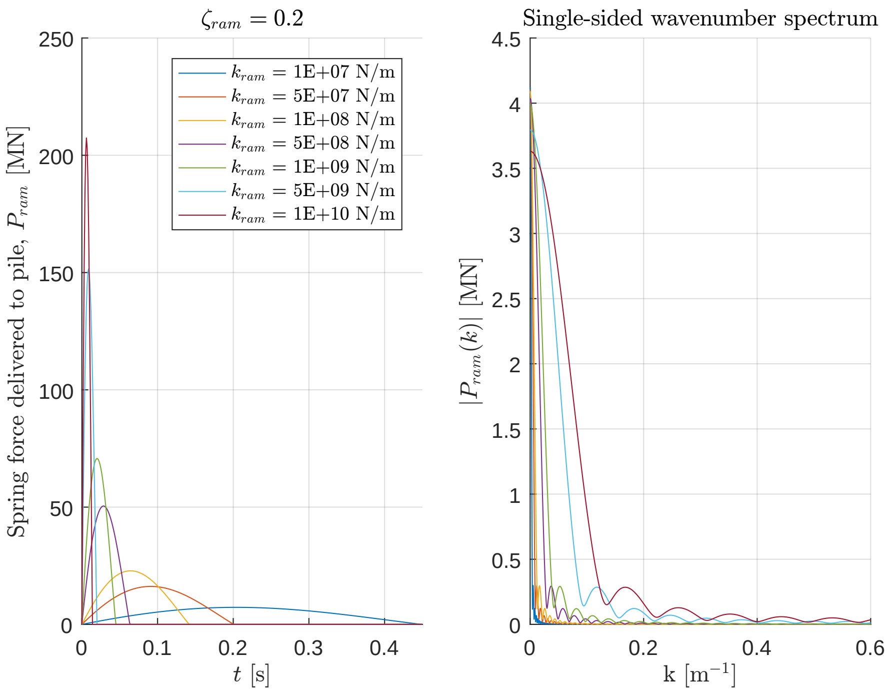

Figure 4.15. Force series and wavenumber spectrum as determined by hammer model when keeping the damping ratio constant. Made assuming an infinitely long and infinitely stiff pile, a ram energy of $E_{kin} = 2\,\text{MJ}$ and ram mass of 100 t.

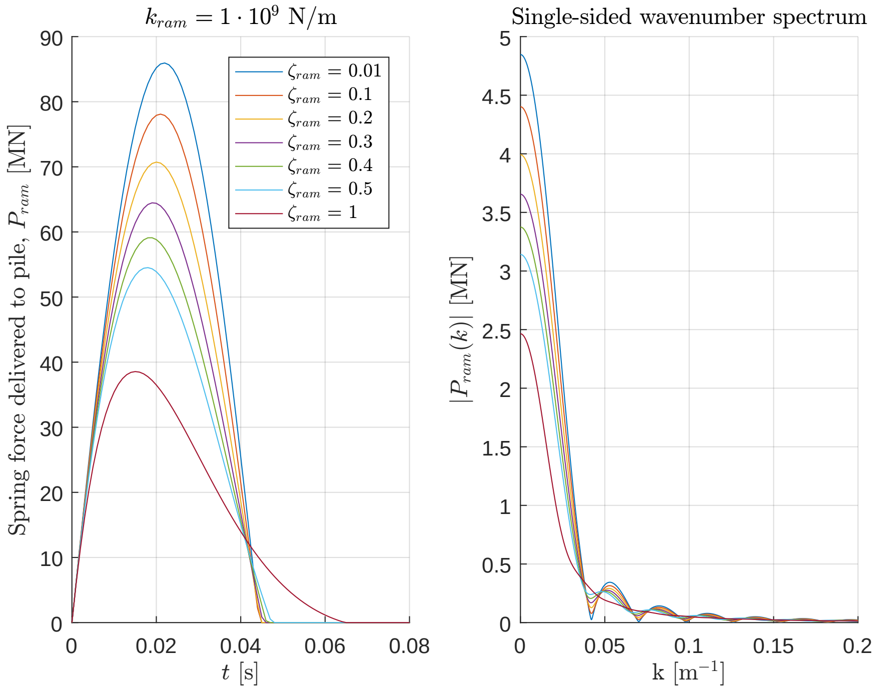

Figure 4.16. Force series and wavenumber spectrum as determined by hammer model when keeping the stiffness coefficient constant. Made assuming an infinitely long and infinitely stiff pile, a ram energy of $E_{kin} = 2\,\text{MJ}$ and ram mass of 100 t.

4.4 Transient algorithm

The described system can be combined in the extended non-linear equation of motion:

$$[M]\{a(t)\}+[C]\{v(t)\}+[K]\{u(t)\}+\{R(u,v,t)\}-\{P(t)\}=0 \tag{4.46}$$

where

$\{v\}$, $\{a\}$	$\{\dot{u}\}$, $\{\ddot{u}\}$
$\{R(u,v,t)\}$	Soil resistance vector
$\{P(t)\}$	Self weight and hammer load (hammer load applied to first DOF)

This equation is identified as a non-linear differential equation and requires a stable time integration scheme in order to solve for the displacement and its derivatives. To keep the required effort of the solution down, an efficient (i.e. accurate and stable), yet fast transient solver is needed. As all the involved variables can be discretized in various ways as shown in the previous sections, the solution algorithm can be based on a number of solvers for step-by-step (or time marching) solutions, where the equation of motion is satisfied at each time step.

4.4.1 Choosing time integration scheme

Overall, numerical time integration schemes can be categorized as either explicit or implicit. Explicit methods can be used for calculating the future state of a system from the present state, while implicit methods involves assumptions about the future state and the variation of the derivatives from the present to the future state, or in short:

$$\begin{aligned} S(t+\Delta t) &= Ex(S(t)) \quad \text{(explicit methods)} \\ Im(S(t),S(t+\Delta t)) &= 0 \quad \text{(implicit methods)} \end{aligned}$$

Combinations of the two method classes are also possible. Of classical explicit methods for solving ordinary differential equations in structural dynamics one can mention the forward Euler method or the basic Runge-Kutta methods, and of implicit methods the most common are the Newmark-β method and the Crank-Nicolson method [Andersen, 2006]. The Newmark method has the advantage of operating directly on the equation of motion compared to the state-space formulation needed for the general solvers (e.g. Runge-Kutta) [Andersen, 2006]. The implicit methods requires extra computations, but can employ much larger time steps, as the variation in between time steps is included implicitly. Furthermore, the present problem is stiff and it can thus be expected to have high eigenfrequencies, which may or may not reduce the time step in explicit methods to a very small number.

The requirements of a solver for the system in the present application is:

- Unconditional stability independent of time step (it is desirable to choose the time step based on expected frequency response to keep number of time steps down)
- Time step choice may only effect accuracy
- The method must be able to handle non-linearities well, i.e. ensuring energy and momentum equilibrium in every time step

- Must be stable even in large deformation, long duration analysis
- Stability and convergence may not depend on choice of "computational" parameters like e.g. the values of β and γ in the Newmark method, to ensure convergence for any configuration of pile, soil and especially frequency response - so as to keep the model holistic.

The obvious choice of time integration scheme would be any of the successfully applied schemes to linear structural dynamics problems, especially the convenient implicit methods like the Newmark-β scheme [Newmark, 1959] [Andersen, 2006] [Bathe, 2016]. However, the simple Newmark incremental scheme shown as an example in Appendix C may a) diverge or b) become unstable for general unconstrained non-linear problems such as the present [Bathe and Cimento, 1980].

The dynamics of pile driving is characterised by being highly non-linear, by having large differences in stiffness throughout the structure and by being subject to very short-duration loads giving large stress waves at high frequencies, thus making it impossible to directly apply findings regarding stability and accuracy developed for ordinary linear systems. The central difference scheme, as applied in Pile Dynamics [2010], has the advantage of stability, given that the time step chosen is sufficiently small. The trapezoidal rule Newmark method is unconditionally stable for any linear system, and the choice of time step merely depends on the desired accuracy.

However, numerical instability, especially period elongation and amplitude decay may lead to divergence and unreliable results, even for schemes believed to be *unconditionally* stable. Most statements in the literature regarding terms like these refer to linear systems or short-duration non-linear systems where the period elongation effects may be negligible. Silva and Bezerra [2008] states the reason for instability in long duration, large deformation applications is due to the significant increase in total potential energy of the system over time. In short: The usual convergence guidelines, i.e. unconditional stability in the constant acceleration scheme does not necessarily apply to the present system.

Attempts to remedy the instabilities of implicit schemes in non-linear structural dynamics can according to Bathe [2007] be grouped into essentially two categories:

- Introduction of numerical damping by use of new algorithms
- Using various sub-algorithms to enforce energy and momentum conservation

Both of these methods will affect accuracy as they actively alter the spectral accuracy of the scheme itself, or in other words, numerical dissipation (which must be carefully calibrated) is directly influencing the results.

To better meet the requirements an extensive literature review has been performed, and based on the findings of Zhang et al. [2017] the *Bathe two-step composite integration scheme* seems to be the most efficient of the algorithms explicitly suited for structural problems with large non-linearities in long time frames.

4.4.2 Applied scheme

An algorithm based on Silva and Bezerra [2008] has been adopted and slightly modified according to the present problem and the stability and accuracy considerations in Bathe and Cimento [1980]. Please refer to Appendix D for a mathematical derivation of the method.

The algorithm is founded on the Bathe composite time integration scheme presented in Bathe and Baig [2005], Bathe [2007] and Bathe and Noh [2012]. This scheme is based on a single step, two sub-steps approach. The position of the sub-step is adjusted by the factor $\gamma \in [0,1]$, as illustrated by Figure 4.17. The Newmark method assuming constant acceleration is used for the first sub-step, and the Euler three-point backward method used for the second substep.

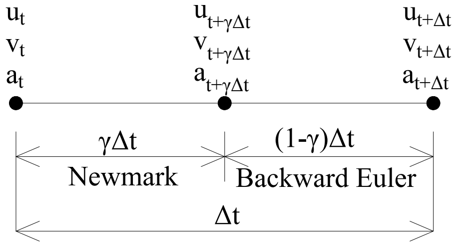

Figure 4.17. Illustration of sub-step approach.

The approach is implicit and combines the stability (in linear analysis) and good accuracy of the Newmark constant acceleration method, with the tendency of explicit methods to introduce numerical damping. Numerical damping is in general not desired, but Zhang et al. [2017] suggest that the damping is insignificant (albeit in a linear SDOF system) and here it makes sure that the stability is almost unconditional, also for non-linear unconstrained systems.

The algorithm can be described by the flowchart seen in Figure 4.18. The constants c_1, c_2 and c_3 originates from the backward Euler approximation:

$$\dot{u}_{t+\Delta t} = c_1 u_t + c_2 u_{t+\gamma\Delta t} + c_3 u_{t+\Delta t} \tag{4.47}$$

$$c_1 = \frac{1-\gamma}{\gamma\Delta t} \quad , \quad c_2 = \frac{-1}{(1-\gamma)\gamma\Delta t} \quad , \quad c_3 = \frac{(2-\gamma)}{(1-\gamma)\Delta t} \tag{4.48}$$

The value of γ dictates the value of the iteration matrices $[K_1^*]$ and $[K_2^*]$. If the value $\gamma = \sqrt{2}-2$ is used, these matrices become identical and is assumed throughout this project unless otherwise stated.

Strictly speaking, when applying the full Newton-Raphson iteration scheme, a new tangent stiffness (and damping) matrix should be calculated at each iteration step corresponding to the current soil resistance, as shown in Equations (4.27) and (4.29). This is not a computationally inexpensive task, and as the stiffness of the pile material for most of the analysis is larger than the soil stiffness and constant, the initial stiffness modified Newton-Raphson method is used. In practice, only few iterations (which can be computed using a constant, pre-inverted matrix) are needed for equilibrium even when using the initial stiffness.

Convergence criteria and acceleration

The definition of convergence criteria in Figure 4.18 is based on Bathe and Cimento [1980], which discusses some general considerations when solving non-linear structural equations.

A convergence criterion may be based on incremental displacement norm, norm of residual (or out-of-balance load) or the combination of the two: The increment in internal energy, i.e. the work done by the residual r on the displacement increment Δu. In this project the convergence

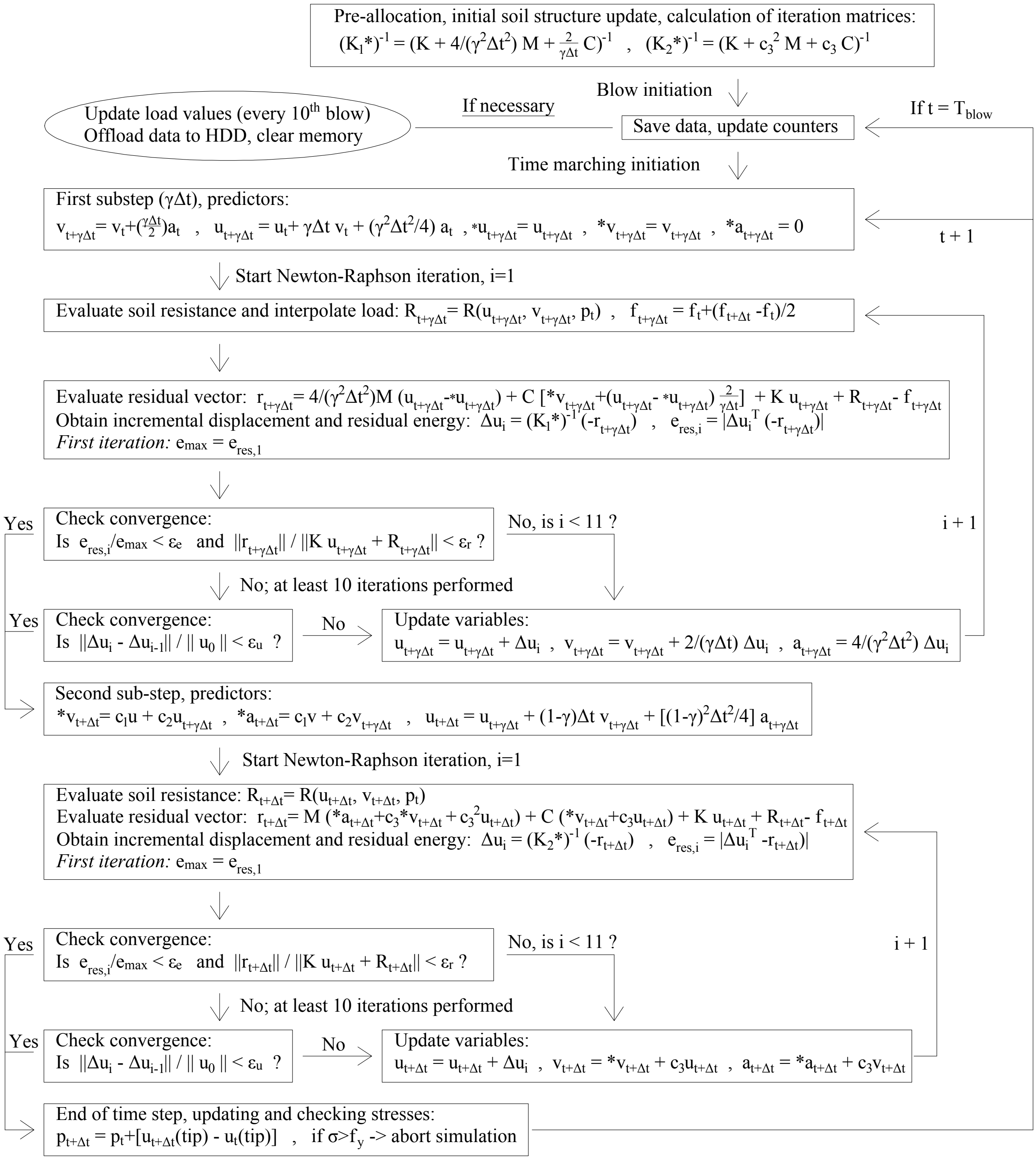

Figure 4.18. Flowchart of solution algorithm for response of system. Matrix and vector notations are omitted for simplicity. A further convergence criterion, which is omitted in the figure is whether the norm of the difference of two succeeding Δu are smaller than floating-point precision of the computer.

criteria are combined in order to not falsely conclude convergence, consequent error build-up and eventually blow-up.

The displacement criterion is according to Bathe [2016] not favourable for most applications, as it in special cases tends to predict convergence even if the residual is sizeable. However, the residual may in some cases change very slowly, e.g. when the hammer load value is zero for the last part of each blow series.

As shown in Figure 4.18 a compromise is made, where the displacement criterion is checked after 10 iterations in which the energy and force criteria have been unsuccessful. Is the displacement criterion met, the iterations are stopped. Is the displacement criterion not met, the iterations proceed until either the force and energy criteria or the displacement criterion is met. The displacement criterion is compared to $||u_0||$, which is the vector norm of the calculated displacement after the pre-simulation equilibrium has been reached.

As the initial stiffness Newton-Raphson method is used, the tangent stiffness may become imprecise over the simulation duration, excessively increasing the number of required iterations. This is partially countered through the use of the *Aitken convergence acceleration scheme* [Aitken, 1937].

For every even iteration count (i.e. $i = \{2, 4, 6, ...\}$) Δu_i is multiplied by:

$$[\alpha_i] = \begin{bmatrix} \dfrac{\Delta u_i}{\Delta u_{i-1} - \Delta u_i} & & \\ & \dots & \\ & & \dfrac{\Delta u_i}{\Delta u_{i-1} - \Delta u_i} \end{bmatrix} \quad \text{(factor calculated for individual DOF's)} \tag{4.49}$$

This relates the local secant stiffness to the initial stiffness. The denominator in Equation (4.49) may become small and thus lead to "explosions" in acceleration. Therefore, if any of the resulting acceleration factors exceeds 2, the update is not performed.

4.4.3 Discretization

In order to obtain a numerical solution of the dynamical problem, Equation (4.46) is evaluated at a number of discrete time points t_j. The spacing between time step t_j and t_{j+1} is Δt and depends on a number of things:

1. Sufficient resolution of the load pulse
2. The Courant-Friedrich-Lewy (CFL) criterion
3. Numerical stability

Regarding 1., the Nyquist frequency of the system assuming a specific time step Δt is $f_{Ny} = \dfrac{1}{2\Delta t}$. The basic frequency of the load pulse may as discussed be of the order $f_{pulse} \approx \dfrac{1}{20\,\text{ms}} = 50\,\text{Hz}$. f_{Ny} must therefore be larger than this. The elastic wave in the pile is in practice the governing factor regarding the temporal discretization. The CFL condition [Courant et al., 1928] states that any wave should not be able to move through an element without being noticed. This condition is easy to fulfil in the present application as a single wave speed is dominant. The largest allowable time step due to the CFL condition is found from:

$$Cr = \frac{c_0 \Delta t}{\min(l_e)} \quad , \quad C \leq 1 \tag{4.50}$$

where

Cr	Courant number
l_e	Pile finite element lengths

Regarding 3., as discussed in Section 4.4.2, numerical stability should be ensured for all time step sizes using the present integration scheme. Unless otherwise stated, a Courant number of 1.0 has been assumed throughout this project.

Regarding spatial discretization, a number of considerations must be taken. Typically, monopile structures are not uniform. The outer diameter may be constant, but generally the wall thickness may vary according to Figure 4.19.

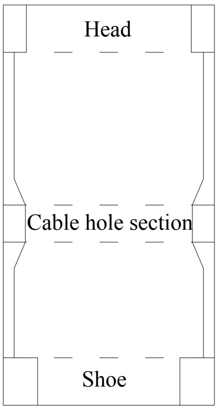

Figure 4.19. Schematic overview of typical wall thickness distribution in a monopile structure. The individual segments may be tapered more than shown here and are typically 3 m in height dependent on weight.

Stresses are typically evaluated at the welds for fatigue analysis. In finite element models, the stresses are most accurately calculated in element interiors. This poses a dilemma, because it is crucial in structural dynamics that the stiffness is accurately represented and changes in cross-section not averaged out. The accuracy of the dynamic analysis is assumed to be more important in the present project. The stresses in adjacent elements to a weld may be computed and through use of special S-N curves, fatigue analysis may still be accurate.

The stress wavelength in the pile can be approximated as:

$$L_w = c_0 T_{pulse} = \frac{c_0}{f_{pulse}} \approx \frac{5000\,\mathrm{m/s}}{50\,\mathrm{s}^{-1}} = 100\,\mathrm{m} \tag{4.51}$$

which is longer than the typical length of a monopile. Andersen [2006] states that for linear elements, $n_{ele,w} > 10 - 12$ should be used.

Using these considerations, an algorithm is applied for defining the finite element model domain:

1. Define the individual model segments such that a change in cross-section results in a segment change
2. Define $\max(l_e) = \dfrac{L_w}{n_{ele}}$
3. Loop over each segment
    a) Calculate $n_{ele} = \dfrac{l_{segment}}{\max(l_e)}$ and round up to nearest integer
    b) Calculate element length in segment as $l_{e,segment} = \dfrac{l_{segment}}{n_{ele}}$
4. Save element lengths, assemble coordinates, calculate cross-sectional variables etc.

After this procedure $\min(l_{e,segment})$ is used in the Courant condition to determine the time step.

Implementation

To avoid shock-waves and interference between gravity load and hammer load, the gravity load is first "ramped" up linearly one DOF at a time for a period of 0.1 s, whereafter this pre-simulation is run until equilibrium between pile weight and soil resistance has been reached, i.e. until the pile tip velocity slows to zero. Hereafter, the main simulation starts, which proceeds with additional hammer blows until the target penetration has been reached.

The algorithm has been programmed to run in MATLAB and is enclosed with the present report, please see Appendix E.

The computational speed is due to the program being run in MATLAB highly dependent on computer performance, most importantly processor speed, and can benefit greatly from being compiled in a more efficient environment.

The developed program presents good opportunities for easy parallelization for many calculations with known parameters (i.e. a wind farm as mentioned in the introduction). Another possibility is to automatically train a MATLAB convolutional neural network with this implementation and a database of CPT-measurements and driving records, in order to obtain end-to-end regression between the physical hammer properties, soil data, pile geometry and resulting blowcount as function of depth with no required user input regarding the model parameters. A focus if implemented in a neural network should be error handling and automatic error pattern recognition, as unrealistic results may occur for out-of-range values of the various soil parameters etc.

4.5 Summary and discussion

A study of the GRLWEAP program and the underlying model (which have survived more or less unchanged since the 1960s) has revealed some shortcomings regarding the dynamic model, the solution hereof and the evaluation and discretization of the associated soil model. Specifically, the discretization is identical for both pile, side friction and tip resistance, even though different characteristic lengths are relevant for these three sub-models. A questionable procedure in GRLWEAP is that the soil resistance parameters are simply interpolated to the current pile coordinates, which are spaced "approximately 1 m apart" according to the documentation. This may unintentionally reduce the characteristic variations in the soil resistance profile. Even though the resistance depends on both displacement and velocity it is not updated for each correction of those quantities. This in turn means that the time increment must be small in order to capture the variation in soil resistance with displacement and velocity somewhat appropriately. It should be noted that GRLWEAP is a proprietary software and as the source code is not available to the public, the assessment of the program is based on the somewhat limited documentation available. GRLWEAP and other similar programs is in such widespread use, that a set of default model parameters have become de-facto standards.

To propose an alternative to GRLWEAP and to address some of the issues regarding it, a dynamic numerical model has been developed. The model evaluates the tip resistance and side friction in more reasonable spatial resolutions, both of which can be changed independently of the pile discretization and each other.

The soil model is based on the existing approaches, in order to be able to use published soil resistance models, but as it is separated from the calculation of stiffness and damping in the pile model, it may take any form and may be dependent on more fundamental approaches to estimating the soil stiffness and damping. This organisation fits with the recommendations regarding future developments of the soil resistance models as explained in the section above.

A literature study has revealed that even though a hammer model is basic and does not entirely model the characteristics of the entire driving system, it may still yield accurate results. Several analytical solutions to various hammer models have been identified in the literature. All of these models make use of assumptions regarding pile and soil impedances, which can only be approximations due to the empirical nature of the soil resistance. With this in mind, a simple SDOF numerical sub-model has been derived instead, which through the compression of a spring delivers a force to the pile head. The initial condition for each hammer blow is the velocity associated with the current hammer energy, which is adjustable in the field.

The simple numerical hammer model is a more versatile formulation compared to the analytical models, as the pile and soil impedance are implicitly included by simply using the pile head movements in calculation of the spring compression. It can be used for any type of hammer and for the entire simulation duration. A parametric study showed that in practice, the user must know the maximum pile force and/or pulse duration in the pile head to correctly configure the hammer model. Along with relatively short computation time, the library of hammer characteristics is the biggest advantage of GRLWEAP over the program developed in the present project.

The developed program uses a relatively complicated solution algorithm for the transient response. Contrary to most finite element models, pile driving simulation involves short bursts of very large differences in stiffness and damping, large deformations and long duration (i.e. many time steps), which may introduce large errors, divergence and "blow-up" of any non-suitable algorithm. The first development of the presented model applied a more straight-forward incremental Newmark scheme believed to be unconditionally stable. This alleged unconditional stability is however only true for linear or short-duration small-deformation non-linear systems. The applied scheme uses relatively long time increments and handles errors (which are especially pronounced for the calculated nodal accelerations) by using a combination of an implicit and explicit scheme to form a more robust, but slower solution.

5. Convergence and sensitivity studies

In order to investigate the convergence of the proposed scheme, along with gaining an understanding of the plausible ranges of the modelling parameters, a test programme of different cases in which the various parameters are varied has been run. The purpose of this chapter is to outline the main outcomes of this test programme.

The available output is substantial, and only some of it is relevant for specific studies. Relevant results are presented and discussed for all the performed analysis in Appendix F. A summary of the findings can be found in Section 5.2 below. The output considered in the analysis includes:

- Displacement, velocity and acceleration in pile DOF's
- Tip resistance, side friction and blowcount as function of depth (an example of this can be seen in Figure 5.1) and average values hereof where appropriate
- Hammer force and soil resistances as function of simulation time
- Total number of blows required to reach target penetration

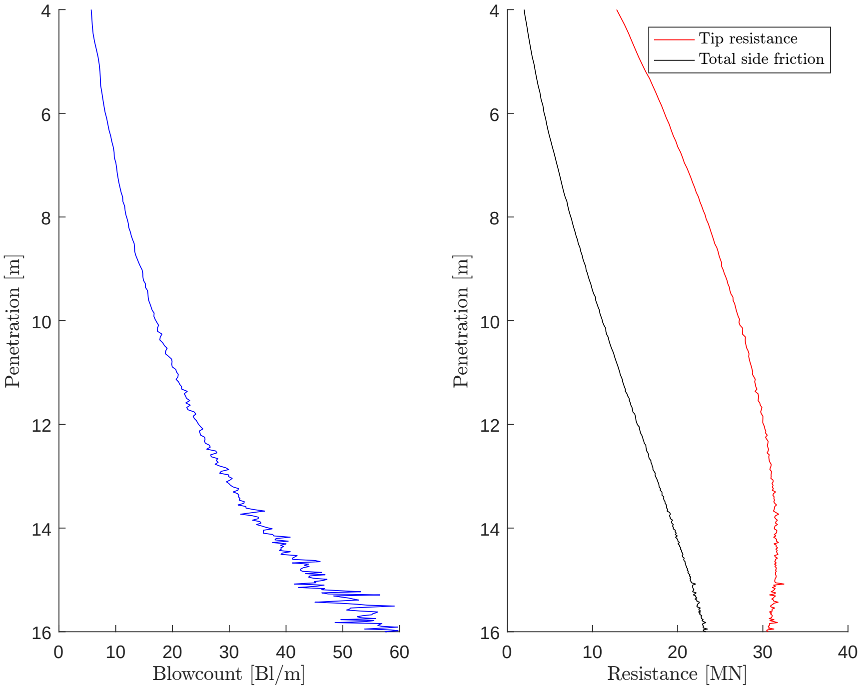

Figure 5.1. Case (b): Blowcount and resistance vs. depth in the configuration $\Delta z = 0.05\,\mathrm{m}$ and $\Delta z_p = 0.05\,\mathrm{m}$, sampled at the time of maximum pile tip velocity of each blow.

5.1 Test programme configuration

A set of cases, each examining various properties of the model essential for configuring models for general use, has been devised. The cases considered are:

- **(a)** Entirely constant soil parameters with depth to investigate whether the choice of soil discretization as expected in this case have little influence on the results
- **(b)** Simple linear variation with depth of q_T and δ_{cv} to investigate whether similar discretization to case (a) is sufficient in this case
- **(c)** Simple linear variation as case (b) but with a single, thin layer at a significant depth to examine the soil discretization necessary to capture this variation
- **(d)** Same as (b), but investigating (independently) the influence of:
  - Courant number Cr
  - Precisions ε_F, ε_e and $\varepsilon_{\Delta u}$ of Newton-Raphson scheme
  - Sub-step position γ
  - Number of pile elements per wavelength, $n_{ele,w}$
- **(e)** Same as (b), but investigating (independently) the influence of:
  - Simulation time for each hammer blow
  - Hammer stiffness k_{ram}
  - Hammer damping ratio ζ_{ram}
  - Structural damping ratio ζ_{pile}

5.1.1 Common parameters

The example pile has four cross-sections and has the properties listed in Table 5.1.

Table 5.1. Assumed pile properties (reference) for example simulation.

Length L	20 m
Specific density γ_p	7850 kg/m^3
Young's modulus E	2×10^5 MPa
Damping ratio ζ_{pile}	0.05
Outer diameter D_o	5 m
Segment height $l_{segment}$	5 m
Segment wall thickness w_t	50 mm, 55 mm, 60 mm and 65 mm
No. elements per wavelength $n_{ele,w}$	20
Element length l_e	5 m
Initial self-penetration due to self-weight (assumed) p_{ini}	1 m
Final penetration p_{final}	16 m

A number of soil model parameters seen in Table 5.2 have been assumed. Constant damping parameters have been assumed, but they may depend on depth as well. The Alm & Hamre SRD model has been assumed.

Table 5.2. Assumed soil parameters (reference) common to all sensitivity test cases.

q_s [mm]	q_t [mm]	J_s [s/m]	J_t [s/m]	n	κ
2.5	2.5	0.25	0.5	0.5	0.8

For case **(a)** through **(c)**, the force Newton-Raphson tolerance have been set to $1\cdot10^{-2}$ and the energy and displacement tolerances to $1\cdot10^{-3}$, the sub-step position $\gamma=2-\sqrt{2}$ and the Courant number to 1.00. This is also used as reference values in case **(d)** and **(e)**.

Table 5.3. Assumed hammer properties (reference) for example simulation.

Ram energy E_{kin}	1200 kJ
Ram mass m_{ram}	60 t
Hammer stiffness k_{ram}	1×10^9 N/m
Hammer damping ratio ζ_{ram}	0.2
Auxiliary mass incl. anvil	80 t

The default hammer properties are as listed in Table 5.3.

The configuration chosen involves a relatively short pile in relatively weak soil in which the effect of the overburden pressure increases somewhat with depth, and a high ram energy. This combination has been chosen in an attempt to investigate whether the model is stable for very high penetration rates, i.e. whether the model handles the geometric non-linearity somewhat sufficiently.

5.1.2 Investigated ranges of parameters

Cases (a) through (c) involves varying the soil node spacing. 20 configurations of this discretization has been examined, as seen in Table 5.4.

Table 5.4. Investigated combinations of soil discretization in m.

Δz	Δz_p				
1.00	0.75	0.50	0.25	0.1	0.05
0.75	0.75	0.50	0.25	0.1	0.05
0.50		0.50	0.25	0.1	0.05
0.25			0.25	0.1	0.05
0.1				0.1	0.05
0.05					0.05

Case (d) and (e) entails investigating the influence of various model parameters not related to soil discretization. The ranges of the investigated parameters can be seen in Table 5.5.

Table 5.5. Ranges of investigated computational and hammer model parameters.

Parameter	Range
Courant number Cr	0.25-1
Sub-step position γ	0.3-0.95
No. ele. per wavelength $n_{ele,w}$	20-100
Newton-Raphson tolerances $\varepsilon_e = \varepsilon_{\Delta u} = 0.1\varepsilon_F$	0.0001 - 0.1
Simulation time to pulse duration τ/T_{Pulse}	1.5-15
Hammer stiffness coefficient k_{ram}	1×10^9 N/m -1×10^{10} N/m
Hammer damping ratio ζ_{ram}	0.01-0.4
Structural damping ratio ζ_{pile}	0.03-0.08

5.2 Summary of convergence and sensitivity studies

Various convergence and sensitivity studies have been performed, and the total blowcount for Cases (a), (b) and (c) can be seen in Table 5.6 through 5.8.

Table 5.6. Case (a): Total blowcount for various configurations of tip resistance and side friction discretizations. Δz and Δz_p in m.

$\Delta z \downarrow \mid \Delta z_p \rightarrow$	0.75	0.50	0.25	0.1	0.05
1	275	273	273	274	274
0.75	275	276	275	275	275
0.5		276	277	277	277
0.25			277	278	278
0.1				279	279
0.05					278

Table 5.7. Case (b): Total blowcount for various configurations of tip resistance and side friction discretizations. Δz and Δz_p in m.

$\Delta z \downarrow \mid \Delta z_p \rightarrow$	0.75	0.50	0.25	0.1	0.05
1	268	268	267	267	268
0.75	270	267	268	267	268
0.5		268	267	267	268
0.25			268	270	267
0.1				270	270
0.05					271

Table 5.8. Case (c): Total blowcount for various configurations of tip resistance and side friction discretizations. Δz and Δz_p in m.

$\Delta z \downarrow \mid \Delta z_p \rightarrow$	0.75	0.50	0.25	0.1	0.05
1	312	392	385	381	379
0.75	314	383	353	347	344
0.5		389	373	367	366
0.25			369	363	360
0.1				356	358
0.05					356

The final number of blows for Case (d) and (e) along with other results of the sensitivity studies can be found in Appendix F.

On the basis of the results presented and commented in Appendix F, the following can be stated (mainly valid for end-bearing piles):

- Regarding soil discretization:
  - For uniform soils, the choice of discretization does not effect the overall (average) results, but does effect the smoothness. A relatively coarse discretization for both the tip and side resistances is sufficient, depending on overburden pressure. The same considerations are applicable to linearly varying strength parameters.
  - Regarding tip discretization in non-uniform soils (i.e. with abrupt property changes), a relatively fine tip discretization of approximately five elements per m or more

    is necessary in order to realistically predict the change and average values of tip resistance and blowcount. Unfortunately, smaller tip discretization does not alone guarantee convergence.
  - Regarding side discretization in non-uniform soils, the side discretization should be chosen finer than approximately three elements within the layer with significant differences in soil strength (and sufficiently fine with respect to friction fatigue degradation factor, if this is used), in order to obtain realistic results for the side friction. The total blowcount converges toward smaller values for finer side discretization, which is an appropriate direction of convergence for practical use.
- Regarding numerical model parameters:
  - For piles driven to small depths, the Courant number has relatively small influence and may be chosen as 1. The influence of the Courant number on the soil resistance increases with depth and for longer piles it is advisable to choose $Cr < 1.00$.
  - Contrary to expectations, the position of the sub-step does not affect the predicted soil resistances significantly or with a clear trend, and a value of $2-\sqrt{2}$ seems to be a good choice due to slightly faster computation.
  - A value of 20 pile elements per wavelength is estimated to be sufficient, as finer discretization yields lower blowcounts (i.e. is less conservative) and as only minor differences with increased values have been detected.
  - Bathe and Cimento [1980] used an iteration precision of $\varepsilon_F = 0.01$ and $\varepsilon_e = \varepsilon_{\Delta u} = 0.001$, which is sufficiently accurate. No significant difference in results for tighter tolerances is seen, and no significant decrease in computation time is found for larger tolerances.
- Regarding load parameters and structural damping:
  - It is more conservative (due to higher blowcounts) but requires considerably more computational effort to choose a large simulation time for each blow compared to the duration in which the force is actually different from zero.
  - It is impossible to determine the hammer stiffness k_{ram} and hammer damping ratio ζ_{ram} from hammer specifications alone, as they are not physical parameters. Knowledge about the pulse duration and maximum or minimum load magnitude can be used to calibrate the parameters within sufficient accuracy. The driving system is more effective the closer the hammer and top pile segment stiffness and impedance match.
  - Regarding structural damping in the pile, it is assumed that a damping ratio of 0.05 is a good compromise between a conservative and a realistic (across the relevant spectrum) estimate on the real damping. For higher damping ratios more energy is lost and the blowcount is thus more conservative compared to reality.

The sensitivity and convergence study serves as a proof-of-concept showing that the model is stable and that it can keep numerical errors in especially the acceleration bounded. This objective has been met, as the model is stable and performs consistent (as seen in Appendix F), relatively invariant to the values of computational model parameters. As desired, the model present some theoretical and practical advancements (but also drawbacks regarding computational speed) over the models prevalent in the industry today.

Another objective was to examine the relative importance of the different model parameters and discretization options (within reasonable intervals). It is concluded, that the values of the set of parameters discussed above can be chosen somewhat confidently, also for general analysis.

The ratio of simulation duration to load pulse duration along with the hammer stiffness (and to some extent damping ratio), is uncertain and has large influence on the model results. The ranges of these parameters has been estimated based on physical considerations and examining the literature. For accurate choices a force-time or strain-time series from full-scale measurements for each individual hammer model, preferably for as long and stiff a pile-soil system as possible, must be available. It has not been possible within the frame of this project to obtain such data necessary for establishing these parameters with confidence. A unique relationship between load pulse magnitude and duration to hammer energy, stiffness coefficient and damping ratio exists for all driving system combinations.

The following chapter contains a study of the application of the model to a case involving a monopile driven in a relatively uniform sand in the North Sea. That study serves two purposes: To examine the validity of the model when compared to an actual driving record, and to compare the soil resistance models discussed in Chapter 3.

6. Back-calculation of pile driven in North Sea sand

To test the applicability and validity of the model, a so-called back-calculation of an available driving log for a monopile driven in the German sector of the North Sea has been performed.

6.1 Soil conditions

A geological survey is available for the specific location. The classification in that survey is based on CPT measurements and 40 core samples. The soil conditions on the site can be described as consisting of mainly marine and recent deposits of loose to medium-dense sands overlying dense to very dense sands and a single layer of silt. A simplified strata description until 48.50 m below seabed can be seen in Table 6.1.

Original data of the CPT measurements are not available, and a simplification based on a graph of the corrected cone resistance is assumed, as seen in Figure 6.1. The simplification is believed to be conservative regarding driveability analysis.

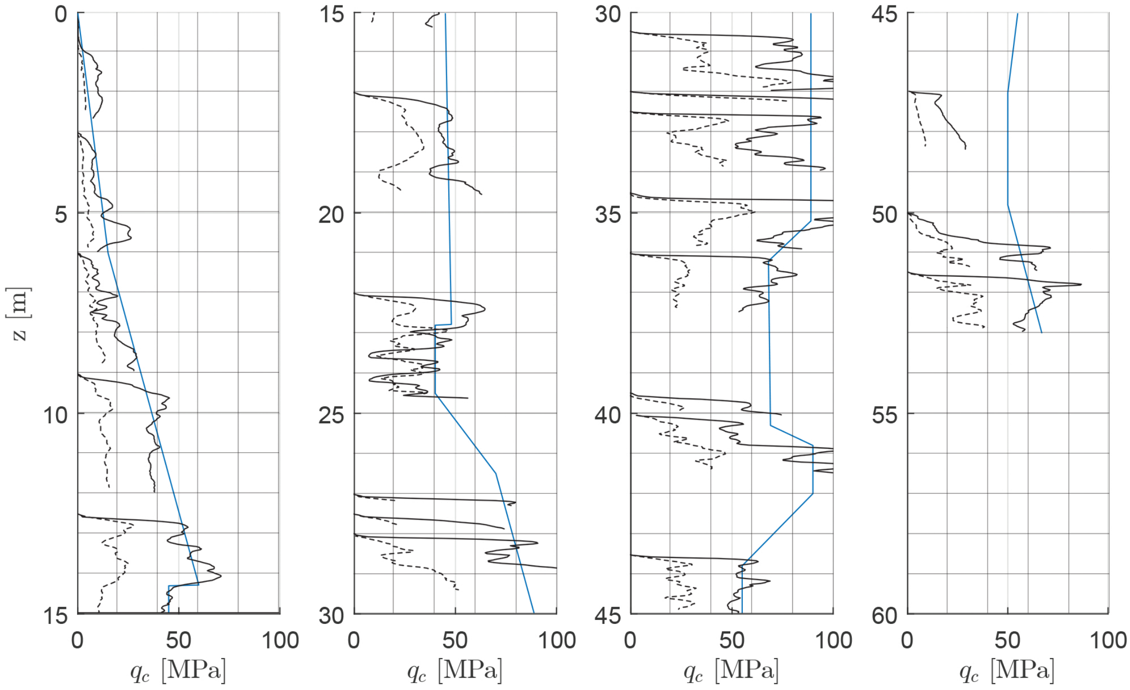

Figure 6.1. Corrected cone resistance and assumed simplification hereof.

Except for the silt layer, the friction ratio is approximately 1% throughout.

Besides the unit weight and cone resistance, it is necessary to estimate the critical-state interface friction angle δ_{cv} between pile and soil. This is done by estimating the effective friction angle

Table 6.1. Simplified strata description of North Sea case. Unit weight estimated based on Table A.1.

Depth [m]	Description	γ [kN/m^3]
0-5.75	Fine and medium sand, organic contents, mildly calcareous to calcareous, slightly silty	18.5
5.75-16.25	Medium sand, gravelly, fine sandy, stripes of silty sand, organic deposits	19.5
16.25-22.80	Medium sand, gravelly, fine sandy, non-calcareous	19.5
22.80-26.50	Silt, slightly sandy, medium stiff, interbedded with medium-coarse sand	18.5
26.50-42	Fine sand, medium sandy, slightly silty	19.5
42-48.50	Fine sand, medium sandy, with silt lenses, with stripes of organic deposits	19.5

based on Section A.2 and subtracting 5° to crudely estimate δ_{cv}. Such an approach is not especially accurate. The alternatives are:

- The correlation between median grain size and δ_{cv} of clean laboratory sands as suggested by Jardine et al. [2005] (see Figure 3.6)
- The suggestion of Randolph et al. [1994] of 0.6-0.7 times the measured friction angle
- Using the recommendation of CUR C118 [2001] of $\delta_{cv} = 29°$ regardless of cone resistance

The first alternative is most likely not realistic in a mixed soil and the latter two options seem non-conservative in a driveability study, which leaves the aforementioned estimation technique.

To summarize, the basic soil parameters used in the simulations can be seen in Figure 6.2.

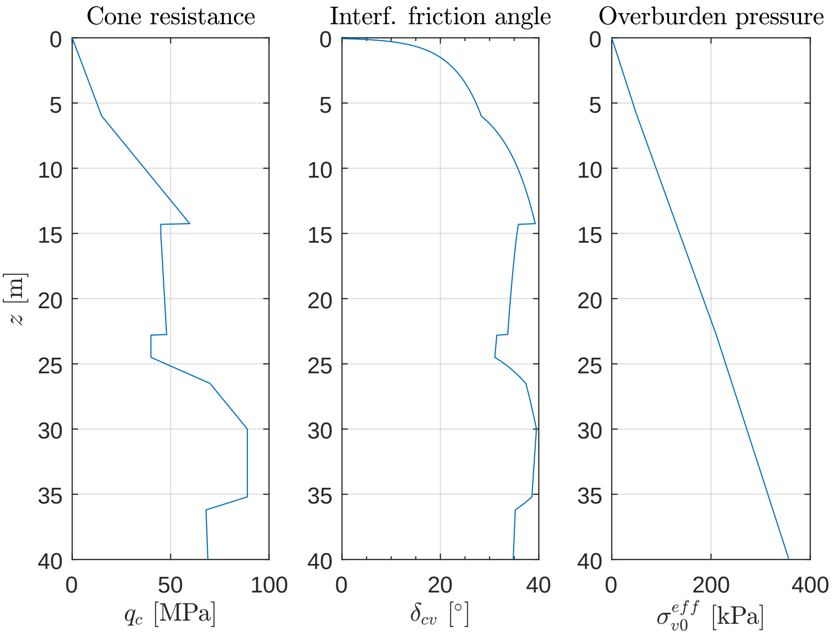

Figure 6.2. Summary of basic soil parameters assumed for the North Sea case.

6.2 Available information about the driving

The available properties of the pile can be seen in Tables 6.2 and 6.3.

Table 6.2. Available pile properties for the North Sea case.

Length L	62.8 m
Specific mass density γ_p	7850 kg/m^3
Young's modulus E	2×10^5 MPa
Yield strength f_y	355 MPa
Outer diameter D_o	5940 mm
Total weight	6218 kN
Penetration at first hammer strike p_{ini}	7.5 m
Final penetration p_{final}	31.05 m

Table 6.3. Available pile segment properties for the North Sea case.

Segment no.	Segment length [mm]	Wall thickness [mm]
1	2000	66
2	3050	60
3	2450	60
4	3050	60
5	2830	60
6-8	3050	60
9	2680	68
10	2240	82
11	1500	96
12	1200	126
13	1500	96
14	2600	84
15-18	2360	78
19	2420	76
20	2480	74
21	2600	70
22	2950	62
23-24	3050	60
25	2560	60

The pile was driven using an IHC Hydrohammer type S-2000 with no pile cushion in spring 2012. The available specifications of this hammer can be seen in Table 6.4. The anvil mass is estimated based on extrapolation in the specifications available in Seaway Heavy Lifting [2017] and may thus be slightly different (probably larger due to anvil ring) in reality.

A driving record of the penetration and average energy per blow is available, sampled at a rate of 4 times per m. This data can be seen in Figure 6.3. It is seen that the full potential of the hammer is not utilised, as the maximum applied energy is ≈ 1000 kJ. The weight of the pile and hammer assembly drove the pile to a depth of 8.4 m before the first hammer blow was initiated, after which the energy was gradually increased and was kept at ≈ 1000 kJ for $p > 15$ m.

Table 6.4. Available hammer specifications of North Sea case [IHC Merwede, 2017].

Model	IHC S-2000
Maximum energy per blow	2000 kJ
Minimum energy per blow	200 kJ
Ram mass	100 t
Auxiliary mass	125 t
Anvil mass (est.)	20 t

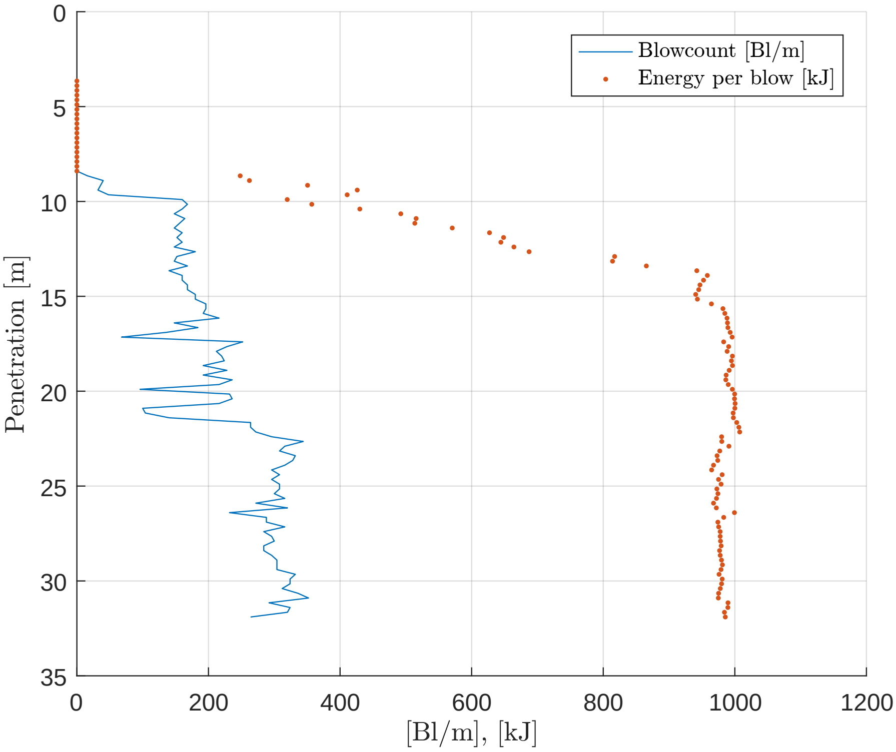

Figure 6.3. Blowcount and average energy per blow for the North Sea case.

6.3 Configuration of model

For the North Sea case, the soil resistance models discussed in Chapter 3 are all used for comparison purposes. As shown in Section 3.2, they all produce quite different results and it is thus expected that some of the models predict pile refusal or underestimate the blowcount seen in Figure 6.3. The energy level is governed by the available driving record and very early refusal is a possibility depending on combination of SRD model and hammer stiffness.

Furthermore, a set of quake and damping values must be assumed. Based on the discussion in Section 3.4 regarding the lack of uniqueness of these parameters in relation to any specific SRD model, the parameters have been chosen as the default values suggested by Pile Dynamics [2010] and Alm and Hamre [1998]. The parameters can be seen in Table 6.5.

Anusic et al. [2016] used different side damping factors for various SRD models (and thus implicitly modifies the models), but fails to state the reason for this. It is suspected that the different damping values in that analysis is due to an iterative fitting procedure. Byrne et al. [2012] also used slightly different side damping factors for different SRD models. For simplicity and because of the lack of uniqueness, the same quake and damping parameters have been used in conjunction with all SRD models in the present project in order to better perform an actual comparison of the SRD models and not case-specific modifications hereof.

Table 6.5. Assumed quake and damping model parameters for North Sea case.

q_s [mm]	q_t [mm]	J_s [s/m]	J_t [s/m]	n
2.5	2.5	0.25	0.5	1.0

A number of characteristic model parameters must be selected for the driving simulations. The assumed parameters are summarised in Table 6.6. All the assumed parameters have been estimated based on Chapter 5 and Appendix F. The hammer stiffness has a large influence on the magnitude and duration of the generated force pulses, and should ideally be calibrated to measurements. It was not possible to compare a sufficiently large range of hammer stiffness values or other model parameters within the time frame of the present project, but an assessment of the possible variations were made and the values of k_{ram} estimated to be most plausible/appropriate were tested. Not all combinations of SRD models and values of k_{ram} were tested.

Table 6.6. Assumed model parameters for North Sea case.

Newton-Raphson tolerances	$\varepsilon_F = 0.01,\ \varepsilon_e = \varepsilon_{\Delta u} = 0.001$
Courant number	$Cr = 0.75$
Elements per wavelength $n_{ele,w}$	20
Sub-step position	$\gamma = 2 - \sqrt{2}$
Simul. to pulse duration ratio	$\tau/T_{pulse} = 5$
Tip soil discretization	$\Delta z_p = 0.05\,\text{m}$
Side soil discretization	$\Delta z = 0.40\,\text{m}$
Stiffness regeneration factor	$\kappa = 0.8$
Hammer stiffness	$k_{ram} = 1 \times 10^9\,\text{N/m},\ 5 \times 10^9\,\text{N/m},\ 1 \times 10^{10}\,\text{N/m}$
Hammer damping ratio	$\zeta_{ram} = 0.2$

The shape and magnitude of the force-time series depends on the pile head movement, which in turn depends on choice of SRD model.

The values of k_{ram} and ζ_{ram} yields force-time series of the hammer spring at maximum energy level as seen in Figure 6.4 (assuming no pile head movement - each individual blow and each individual soil model is in reality slightly different).

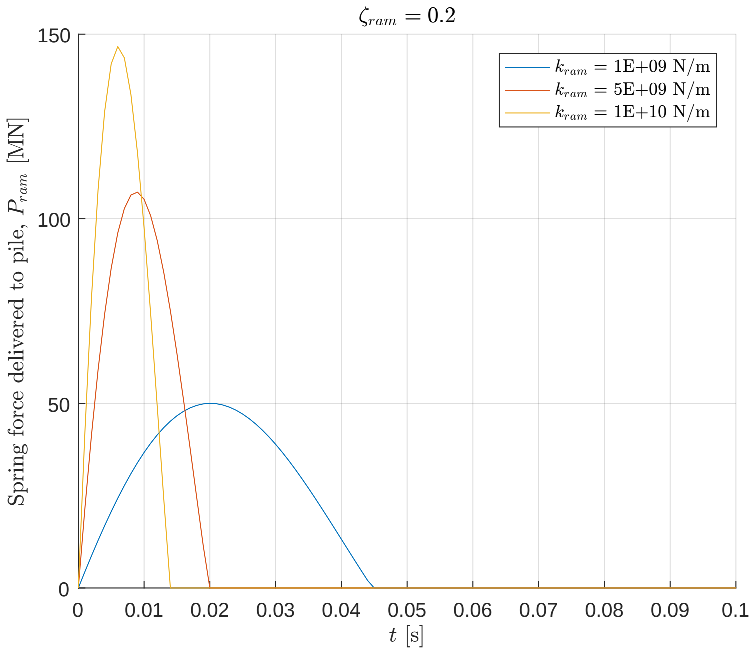

Figure 6.4. Force-time series of the load delivered to the pile head at maximum energy, assuming no pile head movement.

6.4 Results and discussion

The program running time depends heavily on choice of soil model, due to the variations in total resistance. For a large pile with many DOF and soil discretization chosen as the present, the computational speed is approximately 30 s per blow at larger depths (on a laptop with low CPU clock speed), increasing with depth.

The blowcount results of the series of simulations of the test case for various SRD models can be seen in Figures 6.5 and 6.6. It is evident, that large differences in the predictions occur. The associated soil resistance values can be seen in Figures 6.7 through 6.10.

Some of the models apparently predict too large soil resistance, as the simulation fails to even drive the pile to the penetration of the first entry of the driving record. For larger k_{ram} the problem is less prevalent and the simulations proceed - but the resulting short pulse duration is perhaps unlikely. A lower limit of the pulse duration is assumed to correspond with the value $k_{ram} = 1 \times 10^{10}$ N/m. This highlights the problem of the hammer modelling constants - if no calibration data is available the predictions are not reliable and difficult to compare. Another possible reason for the early refusal predictions is that the simple total soil resistance model applied in the algorithm overestimates the static soil resistances for the chosen SRD models and quake values, and as the algorithm is fully dynamic it is possible for the pile to move upwards slightly due to this. The duration in which the hammer force magnitude is different from zero is smaller than the time in which only the self-weight acts, which of course adds to this issue.

Despite the uncertainty regarding the hammer stiffness coefficient, it is possible to deduce that the NGI-99 method as expected predicts the highest blowcounts/earliest refusals. Even with the highest stiffness value, the NGI-99 model predicts refusal at a depth of 12 m. The API, Stevens and Alm & Hamre methods predict the lowest blowcounts. The MTD/ICP results with $k_{ram} = 1 \times 10^{10}$ N/m is similar to the Alm & Hamre at 10 times lower hammer stiffness, which is equivalent to a third of the load magnitude.

The Toolan & Fox model with $k_{ram} = 1 \times 10^9$ N/m exhibits the same problem as the NGI-99 model with $k_{ram} = 5 \times 10^9$ N/m and the MTD/ICP with $k_{ram} = 5 \times 10^9$ N/m regarding failing very early due to high soil resistance and subsequent refusal. It is not clear whether this is due to:

a) The SRD models being unreasonable regarding prediction of resistance to driving (the earliest refusing models are derived as formulas for long-term capacity)
b) An unresolved error in the developed program

An argument for why a) can be the reason is that other combinations of soil model and hammer stiffness coefficient produce somewhat realistic results, and because long-term capacity is known to be larger than resistance to driving.

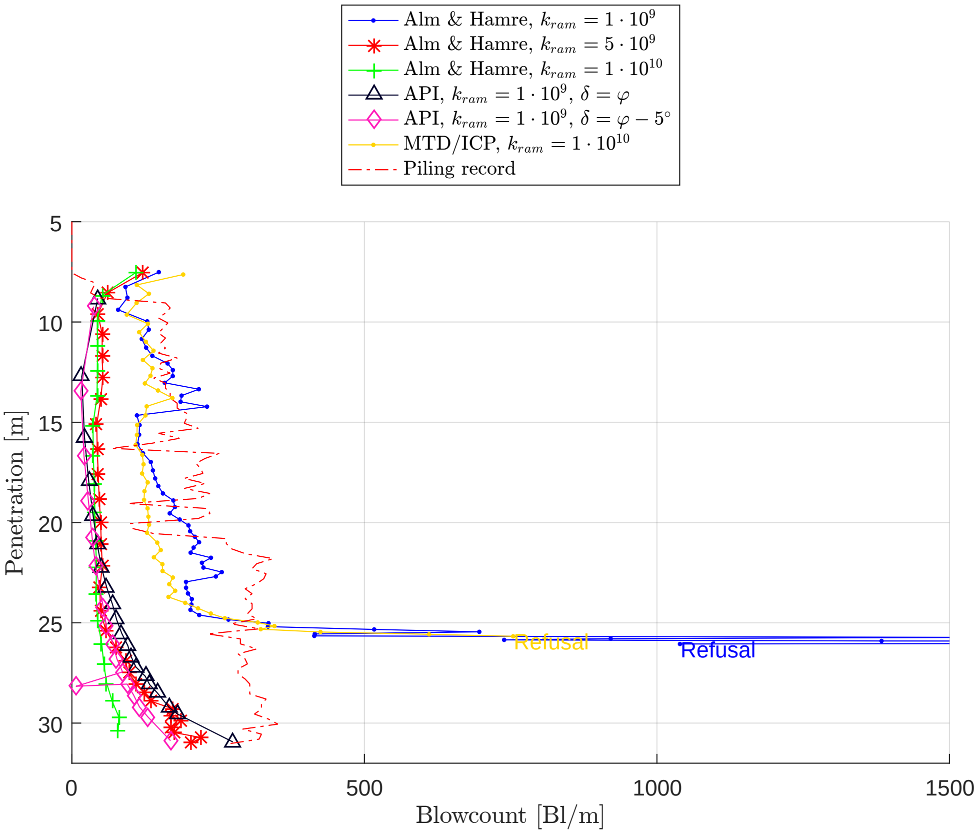

Figure 6.5. Blowcount as function of depth for the North Sea case, assuming a variety of SRD models. Sampled at the time of maximum tip velocity of each blow series. (Figure 1 of 2)

Even though it is not clear whether the model parameters are accurate or which soil models can be generally recommended, the driveability analysis program has been proven to be applicable to real cases, and more analyses similar to the one presented here can reveal more trends in the results.

For dense sands as in this case, the simplest SRD models (API and Stevens) are as expected inaccurate and predict too small blowcounts and too small resistances. Those models can not be recommended for use in driveability analysis of piles driven in sand. Interestingly, some of the

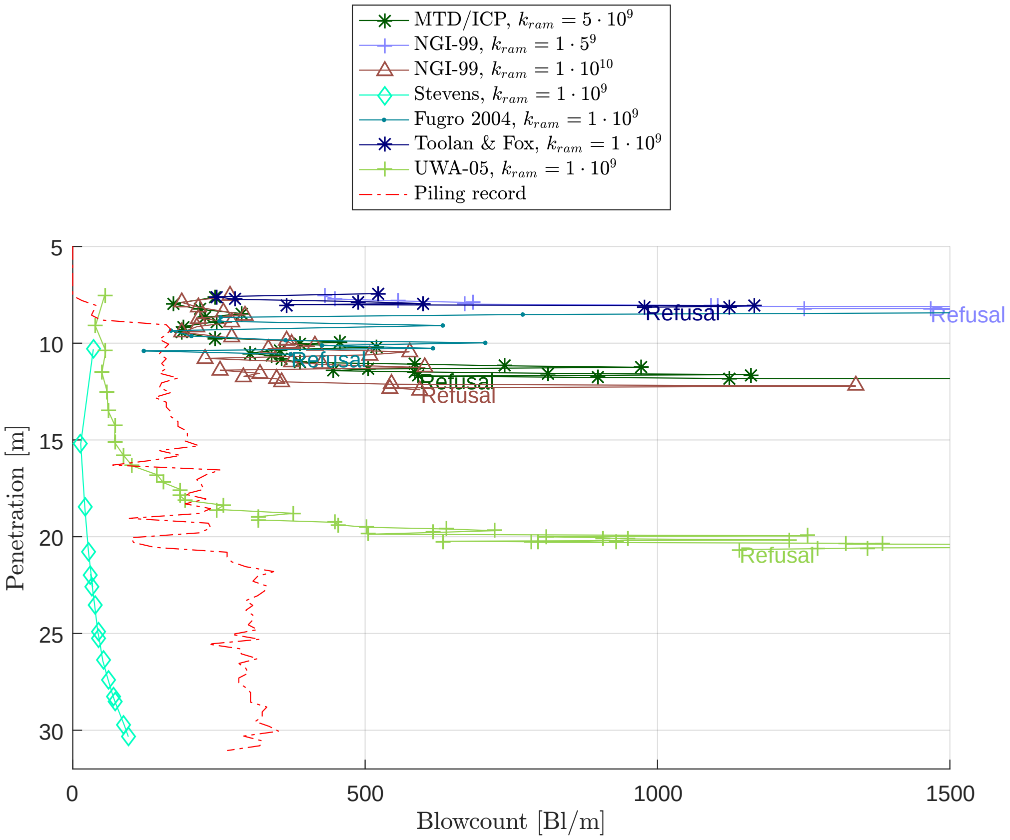

Figure 6.6. Blowcount as function of depth for the North Sea case, assuming a variety of SRD models. Sampled at the time of maximum tip velocity of each blow series. (Figure 2 of 2)

more complex models like the MTD/ICP, NGI-99 and UWA-05 predict much too large resistances (assuming that the hammer stiffness are in the order used in this example) and consequently predict pile refusal when that is not the case.

This might be due to the fact that these models are models of the capacity and not the resistance to driving. Furthermore, it is known that at least the NGI-99 method was proposed as a response to the unrealistically low capacities suggested by the API method. The dedicated driveability model Alm & Hamre seem most accurate, and it is estimated (based on Figure 6.5) that a specific hammer stiffness coefficient value in the interval $1 \times 10^9\,\mathrm{N/m} < k_{ram} < 5 \times 10^9\,\mathrm{N/m}$ can result in a predicted blowcount series very similar to the piling record. The Alm & Hamre, UWA-05 and the API/Stevens methods consistently predict much lower side friction compared to the capacity formula models MTD/ICP and NGI-99.

The predicted tip resistance values for the various models are similar in magnitude, the API, Stevens, UWA-05 and Fugro 2004 tending to predict slightly lower values than the Alm & Hamre and particularly the group of models which assumes $q_{tip} = q_c$ (NGI, MTD/ICP and Toolan & Fox).

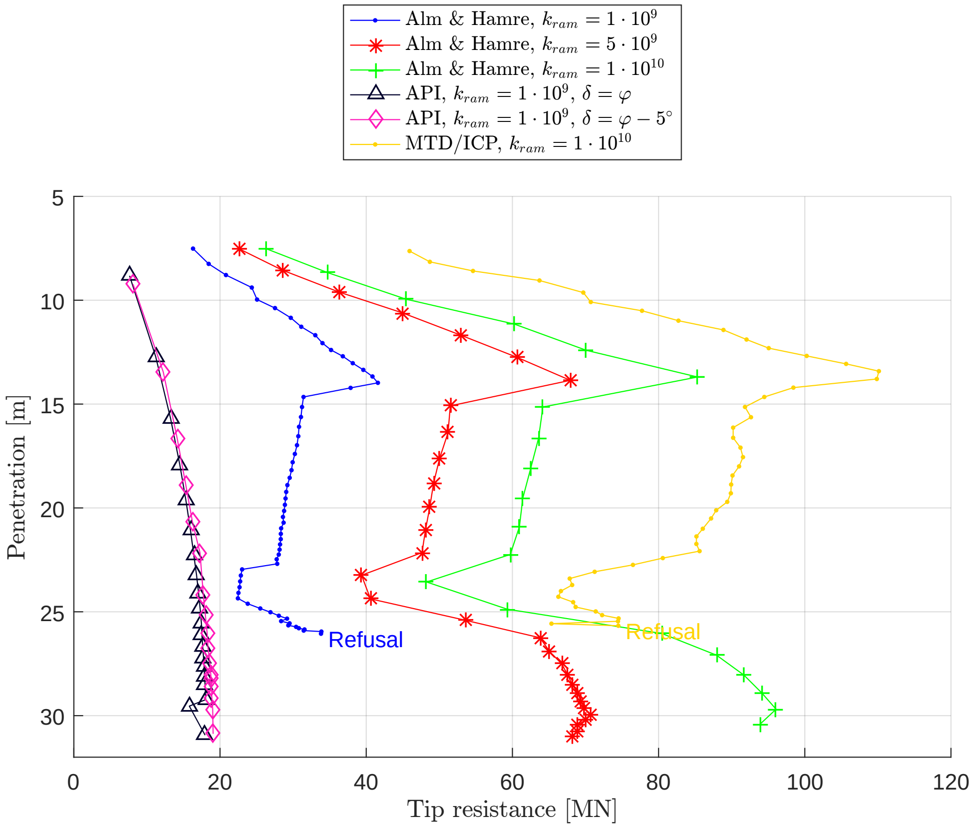

Figure 6.7. Tip resistance as function of depth for the North Sea case, assuming a variety of SRD models. Sampled at the time of maximum tip velocity of each blow series. (Figure 1 of 2)

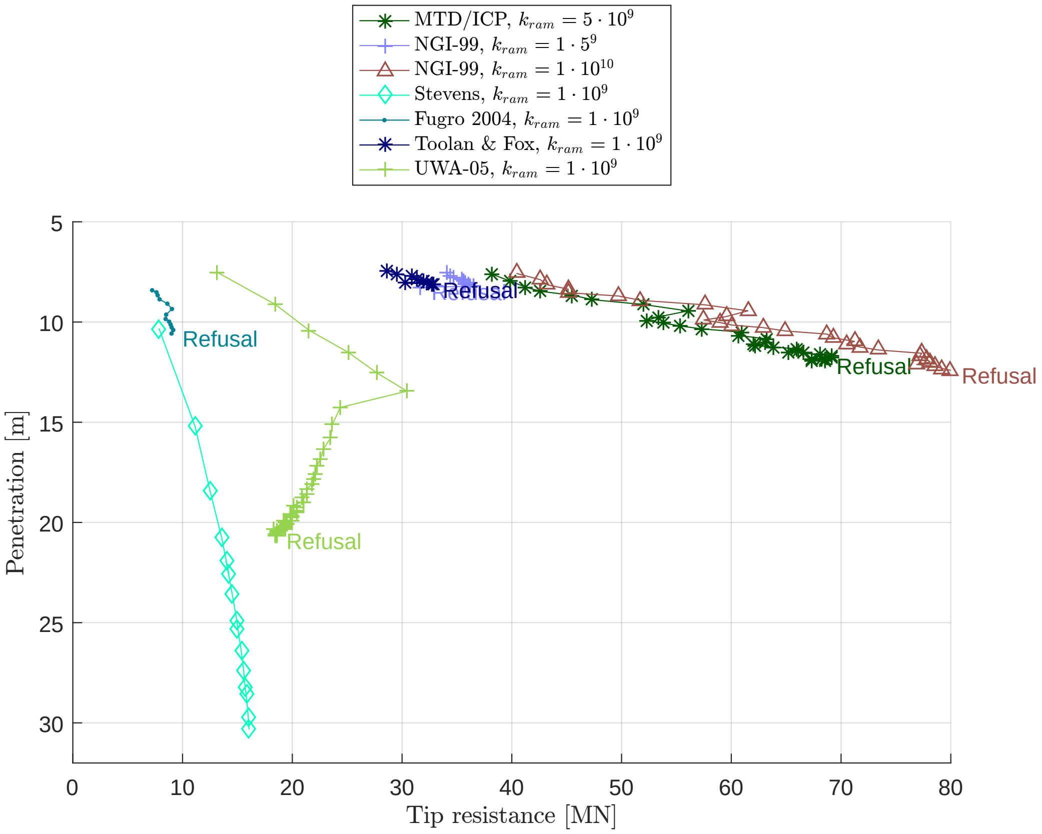

Figure 6.8. Tip resistance as function of depth for the North Sea case, assuming a variety of SRD models. Sampled at the time of maximum tip velocity of each blow series. (Figure 2 of 2)

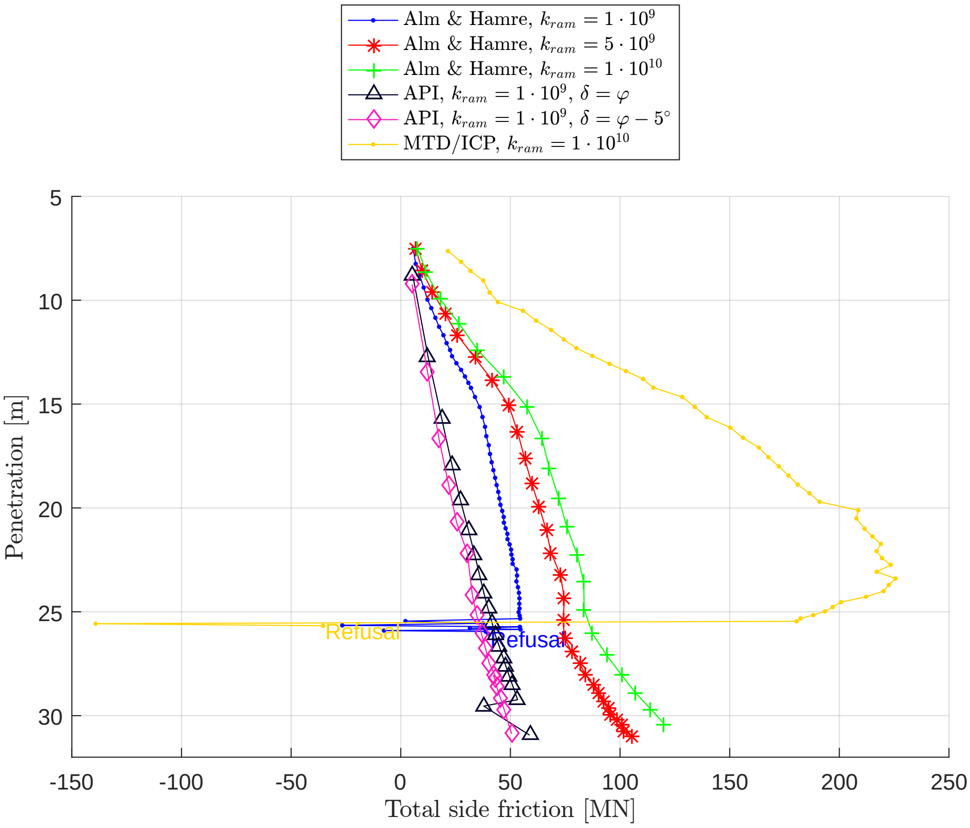

Figure 6.9. Side friction as function of depth for the North Sea case, assuming a variety of SRD models. Sampled at the time of maximum tip velocity of each blow series. (Figure 1 of 2)

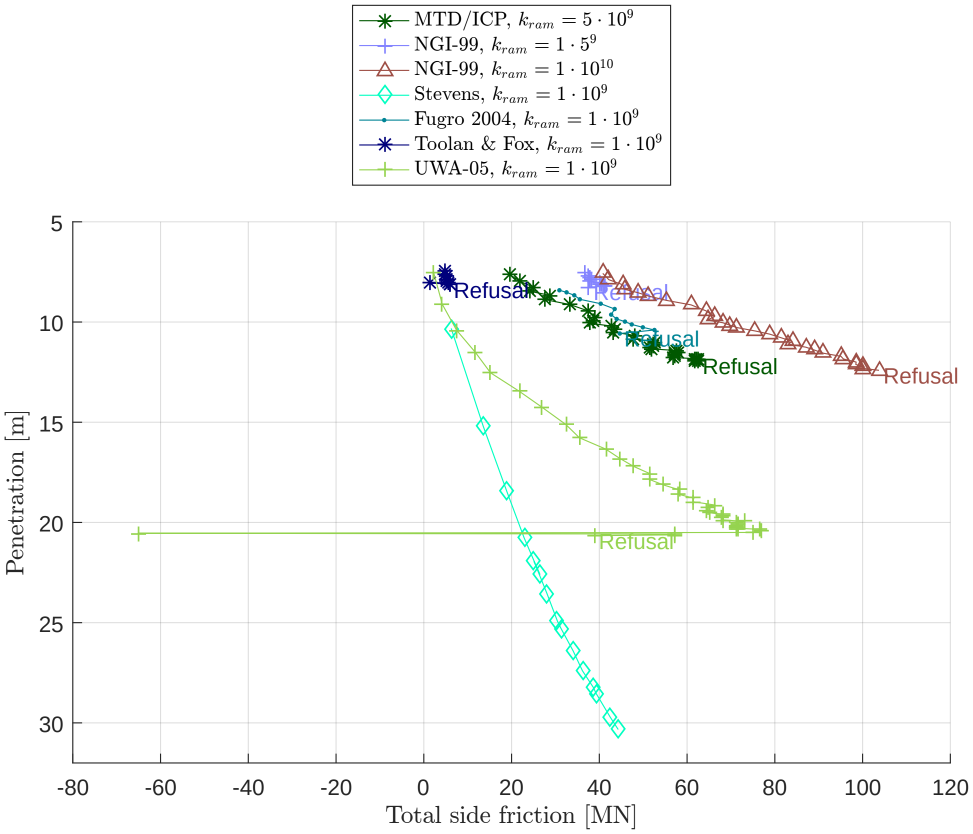

Figure 6.10. Side friction as function of depth for the North Sea case, assuming a variety of SRD models. Sampled at the time of maximum tip velocity of each blow series. (Figure 2 of 2)

7. Conclusion and future work

The present project contains a study of the various commonly applied models for the soil resistance exerted on coring monopiles driven in dense sands. Furthermore, an attempt to unravel and understand the assumptions and procedures of the popular driveability analysis program GRLWEAP and lumped-mass model used in it revealed some critical and not very clearly motivated simplifications and assumptions. Therefore, a new program for driveability analysis attempting to overcome some of these assumptions, while still emphasizing operationality, has been developed by the author.

The investigated models for soil resistance to driving are all based on the Coulomb criterion for shear failure. This is a convenient and physically credible approach, but if desired as the basis of a SRD model for large-diameter piles, future correlations in the style of the Alm & Hamre or MTD/ICP methods etc. should include (in addition to the factors already included in that group of models):

- Normalisations with the pile geometry in a sensible manner to account for the sizes of the piles used in the correlations
- A factor accounting for the difference in horizontal pressure on the in- and outside due to:
    - Driving shoe, which will increase the pressure close to the tip but greatly decrease it some distance above the tip
    - Soil material, as the initial void ratio/relative density at tip influences the amount of dilation
    - Poisson effect in the pile material (if the radial displacement of the pile is significant, the effective horizontal pressure should increase temporarily)
    - Relative horizontal and vertical extent of plastic zone inside the pile as function of overburden pressure and load rate

These factors accounting for the difference in pressure can not easily be obtained analytically and must therefore be based on empirical relations like the other parts of the SRD models. A path of future work could be to establish a set of general equations for these individual correlations and, using the developed numerical model, perform back-calculations of a large number of driving logs and/or static load tests, in order to produce an expression similar to the existing ones, but extended and modified to account for large-diameter piles.

As it is difficult to accurately measure the extent of and stresses within the plastic zone in the soil close to the pile wall and tip, future work could be to develop an accurate non-linear continuum model of the system of pile and surrounding and internal soil (installed to some depth "wished-in-place"), using compilations of triaxial and other laboratory test results and corresponding CPT measurements, for each major type of soil and overall degree of consolidation.

This can be done using commercial FEA software with a full material model (which must be specifically calibrated to high accuracy) suitable for the chosen soil, where the pile is incrementally loaded until sliding occurs. This should be performed for many different depths with appropriate overburden pressures as boundary conditions. The extent of the failure zone internally and externally and the magnitude of horizontal pressure should be measured. This can then be correlated to CPT cone resistance normalised with overburden pressure and loading rate to obtain relations to horizontal pressure, actual frictional force and actual stiffness coefficient. The influence of the extents of the failure zone from the tip on the horizontal pressures on the pile wall should be examined. A correlation between CPT cone resistance, overburden pressure, pile wall thickness and pile material to this reduction in horizontal pressure should be made.

Soil damping, i.e. the influence of strain rate on the resistance (alternatively the influence directly on the angle of internal friction) can be assessed based on a dynamic analysis of the continuum, where a time-varying boundary force moves the pile in an oscillatory manner (so slightly, that the finite element mesh is not distorted beyond its capabilities).

The produced set of correlations for each major soil type should then ideally be combined in a single model, taking only quantities derivable from the pile geometry, the kinematic variables of the pile finite-element model presented in the present project and CPT measurements as input. Such an approach is fundamentally different from the existing models, and whether this is practically obtainable in a general sense or only for specific cases similar to the commonly derived t-z and Q-z curves can be the subject of another investigation.

The bulk of the project has been concerned with the complete development of a new truly dynamical finite-element model of pile driving, featuring:

- Full updating of the soil resistance at each iteration step
- Different discretization schemes for pile, side friction and tip resistance
- A continuum approach to the pile model, where a type of master-slave approach is used for evaluating the displacements and velocities at all activated soil nodes
- A stable, more advanced transient solution scheme for the non-linear discrete system equations
- A mathematically separated soil model describing the resistance as function of pile displacement and velocity at all relevant soil nodes. The soil model is however based on the same overall assumptions as in the existing models.
- A dynamical hammer model, which is directly dependent on the pile head response and the current ram energy, and can be calibrated with only two modelling constants
- Few input parameters, all of which are practically obtainable from basic driving system characteristics, pile geometry and commonly performed geotechnical investigations

The main drawback of the developed program is the relatively slow resolution time compared to GRLWEAP. As the entire set of scripts are implemented in MATLAB, which is relatively inefficient as compared to more general programming languages, a significant performance improvement is expected if rewritten in e.g. FORTRAN. Furthermore, a future study could concern more efficient ways of storing data, which can also significantly reduce computation time.

Simply inputting hammer model instead of a set of mass values plus k_{ram} and ζ_{ram} parameters can enhance the ease of use of the program. The values of these parameters can be accurately calibrated to maximum force magnitude and pulse duration measured by e.g. strain gauges in the pile head for each individual hammer model. This will also improve the overall accuracy of the results.

Like GRLWEAP, the precision of the developed model depends heavily on the choice of the quake and damping model parameters, as these govern the stiffness and damping of the soil. The lack of uniqueness of these parameters is a problem, but a more fundamental strain-dependent soil material model is required in order to avoid them. The basic assumptions of these parameters are linearly elastic-perfectly plastic response and that the damping coefficient is simply the proportionality between the current static resistance and the total resistance. Neither of those assumptions are representative of real soil. Soil normally exhibits strain hardening or softening, and damping is normally mainly sensitive to loading frequency.

All input is done by modifying a set of input scripts - the program does not feature a graphical user interface (GUI). Development of a GUI should be a relatively high priority in future work, as this may encourage use of the program if published. Currently, the only practical way of obtaining the soil resistance to driving is through the empirical models, and if more back-calculations of driving records can be gathered, higher statistical confidence can be put on these models.

The numerical model has been somewhat validated based on a North Sea driving record. Various different SRD models has been applied, but as it is impossible to confidently point out a single model as being more precise, and because the quake, damping and hammer model parameters are not uniquely defined, it is of course also impossible to state whether the model is sufficiently accurate for all configurations of pile and soil properties. The general trend for the conditions of the North Sea case is that the the Alm & Hamre model seems most realistic for large-diameter piles driven in dense sands given carefully chosen value of the hammer stiffness coefficient, and that the simplest models are not representative for the actual resistance in dense sands. The more advanced models does not necessarily present improved precision, but are actually too conservative and predicts early refusal for the present case. It is assumed, that this can be partially attributed to the nature of the models; some are dedicated driving resistance models, some are ultimate capacity formulas. Due to the definition of stiffness in the used model for the soil, very large stiffness are present at low depths for the capacity models. Reducing the side resistance in the MTD/ICP, NGI-99 and Fugro methods by some factor, depending on e.g. relative density from cone resistance, will improve the applicability of these methods in driveability analysis. As mentioned, more analyses can reveal whether these trends are applicable to all large-diameter piles and/or can be used to calibrate new SRD models.

List of symbols

a	Acceleration
a_{ram}	Ram acceleration
A	External wall area of pile
A_{end}	End cross-sectional area of pile
A_P	Average cross-sectional area of pile
A_s	Internal wall area of pile
$\{b_e(t)\}$	Boundary load vector
$[B]$	Strain interpolation matrix
c_d, c_{ram}	Driving system or hammer damping coefficient
c_0	Speed of sound in steel
c_1, c_2, c_3	Backward Euler scheme parameters
$[C]$	System damping matrix
C_e	Circumference of pile finite element
C_{method}	Method-specific pile circumference
Cr	Courant-Friedrichs-Lewy condition number
$[C_{soil}(u,v,t)]$	Tangential soil damping matrix
d	Depth
d_{50}	Mean grain size
D_o, D_i	Outer and inner pile diameter
D_r	Relative density of soil
e_{max}	Maximum work of residual force on residual displacement
$e_{res,i}$	Work of residual force on residual displacement in iteration i
E	Young's modulus of pile material
E_{kin}	Kinetic ram energy
E_P	Energy loss in pile
E_R	Rated hammer energy
E_s	Energy loss in soil
f	Frequency
f_{Ny}	Nyquist frequency
f_{pulse}	Basic frequency of load pulse

f_{ram}	Hammer spring force
f_s	Unit skin friction
f_{si}	Initial side friction
$f_{s,i}$	Internal side friction
$f_{s,o}$	External side friction
$f_{s,res}$	Residual side friction
$f_{t,i}$	Unit soil resistance at soil soil node i
f_y	Steel yield strength
f_0	Base-value side friction of model or first natural frequency
$\widetilde{f_i}$	Residual force vector
$\{f^{damp}(t)\}$	Vector of internal damping force
$\{f_{e,g}\}$	Element self-weight vector
$\{f^{ext}(t)\}$	Vector of external forces
$\{f^{int}(t)\}$	Vector of internal forces
$F_{A_{end}}$	Correction for end area proportions
$F_{\overline{q_c}}$	Correction for cone tip resistance averaging
F_{FF}	Friction fatigue coefficient
$F_{g,aux}$	Weight of driving ram auxiliaries (anvil, sleeve, housing etc.)
F_{int}	Internal force vector
$F_{\sigma'_{v0}}$	Correction for normalisation against overburden pressure
$\{F\}$	External force vector
G	Soil shear modulus
$\hat{1}_{toe}$	Column vector with unity in last row and zero everywhere else
J, J_{toe}	Smith damping coefficient of side and toe
$[J]$	Jacobian matrix
k	Wavenumber, shape factor of friction degradation, current soil stiffness
k_0	Initial stiffness coefficient
k_d, k_{ram}	Driving system or hammer stiffness coefficient
k_P	Pile stiffness coefficient
k_s	Soil stiffness coefficient
K	Coefficient of lateral earth pressure
K_0	Coefficient of lateral earth pressure at rest
$\widetilde{K}$	Iteration matrix

K_1^*, K_2^*	Iteration or "effective stiffness" matrix, substep 1 and 2, respectively
$[K]$, $[K_e]$	System and element stiffness matrix
$[K']$	Tangent stiffness matrix
$[K_{soil}(u,v,t)]$	Tangential soil stiffness matrix
l_e	Pile finite element length
$l_{e,segment}$	Pile element length in segment
$l_{segment}$	Pile segment length
L	Pile length
L_i	Element length in Smith model
L_w	Wavelength
m_{ram}	Ram mass
$[M]$, $[M_e]$	System and element mass matrix
n	Smith damping exponent
n_{ele}	Number of pile elements in segment
$n_{ele,w}$	Number of pile elements per wavelength
N_q	Bearing capacity factor
N_q, N_c, N_γ	Terzaghi bearing capacity factors
$N_s(p)$, $N_t(p)$	SPT-N value at side and tip, respectively, at current penetration
$N(y,t)$	Normal force
p	Penetration
$p(y,t)$	Loads including gravity, hammer impact and soil resistance
p_a	Reference (atmospheric) pressure
$\{p_e(t)\}$	Consistent nodal load vector
q, q_{toe}	Side and toe quake relative to global coordinate
q_c	Corrected CPT cone resistance
q_i, $q_{toe,i}$	Local side and toe quake relative to local coordinate
$q_{c,N}$	Normalised cone tip resistance
q_{tip}	Unit end bearing, unit tip resistance
$\overline{q_c}$	Average cone tip resistance in a depth of $\pm 1.5D$ of the pile tip
Δr	Radial displacement mobilising a radial effective stress change
$\{r\}$	Residual force vector
R, $\{R\}$	Soil resistance, soil resistance vector
R_o, R_i	Outer and inner pile radii

R_s	Current static soil resistance to driving
R_T	Total soil resistance to driving
R_u	Total, ultimate soil resistance
$R_{u,s}$	Sum of ultimate skin (side) friction
$R_{u,t}$	Sum of ultimate toe (tip) resistance
s	Permanent set per blow
s_0	Empirical elastic pile deformation
t	Time, wall thickness
Δt	Time increment
$\Delta t_{cri,i}$	Critical time increment for element i in Smith model
T_{blow}	Total single blow simulation duration
T_{pulse}	Load pulse duration
u	Displacement
u_{end}, v_{end}	Displacement and velocity of last pile DOF
u_{rel}	Hammer spring compression
$\delta u(y,t)$	Virtual displacement field
Δu	Displacement increment
v	Velocity
v_{rel}	Ram velocity relative to pile head velocity
w_t	Segment wall thickness
$W_{mid,i}$	Midpoint Riemann sum integration weight at soil node i
Δy	Assumed dilation
y	Pile coordinate, $y = 0$ at pile head
y_e	Pile finite element end coordinates
y_s	Pile coordinate relative to surface
z	Soil coordinate, $z = 0$ at surface
Δz	Side friction node spacing
Δz_p	Tip resistance node spacing
α	Rayleigh damping coefficient
$[\alpha]$	Aitken convergence acceleration matrix
β	Newmark scheme parameter, Rayleigh damping coefficient
β_m	Mass lumping parameter
γ	Sub-step position or unit soil weight or Newmark scheme parameter

γ'	Effective unit soil weight
δ_{cv}	Constant-volume or critical-state interface friction angle
δ_f	Soil-pile interface friction angle at failure
$\Delta\sigma'_{rd}$	Horizontal stress change during installation and equalisation
ε	Normal strain
ε_F	Force tolerance of Newton-Raphson scheme
ε_e	Energy tolerance of Newton-Raphson scheme
$\varepsilon_{\Delta u}$	Displacement increment tolerance of Newton-Raphson scheme
ζ_{min}	Dimensionless damping ratio at minimum damping
ζ_{ram}	Hammer damping ratio
ζ_{pile}	Pile structural damping ratio
η_d	Driving system loss factor
η_h	Hammer loss factor
κ	Stiffness regeneration factor
ρ_i	Mass density of pile element *i* in Smith model
ρ_P	Mass density of pile material
σ	Normal stress
σ'	Total effective soil stress
σ'_f	Normal stress at failure
σ'_{h0}	Effective lateral earth pressure at rest
σ'_{rc}	Horizontal stress infinitely long time after installation
σ'_{rf}	Horizontal stress at failure
σ'_{v0}	Effective overburden pressure
τ	Total single blow simulation duration
τ'_f	Effective shear stress at failure
φ'	Effective friction angle
φ'_{cv}	Critical-state or constant-volume eff. friction angle
φ_{method}	Method-specific friction angle
ϕ_f	Angle of internal friction at failure
$[\Phi]$	Global shape function (displacement interpolation) matrix
$\{\Phi(y_e)\}$	Pile element shape function (displacement interpolation) vector
ω_0	First natural angular frequency
Ω	Pile circumference

References

Aitken, 1937. A. C. Aitken. *The evaluation of the latent roots and latent vectors of a matrix*. Proc. Royal Society of Edinburgh, 57, 269–304, 1937.

Alm and Hamre, 1998. Torstein Alm and Liv Hamre. *Soil model for driveability predictions*. Proc. 1998 Offshore Technology Conference, Houston, TX, USA, 4-7 May., 1998.

Alm and Hamre, 2001. Torstein Alm and Liv Hamre. *Soil model for driveability predictions based on CPT interpretations*. Proc. 15th International Conference on Soil Mechanics and Geotechnical Engineering, Istanbul, Turkey, 2, 1297–1302, 2001.

Andersen, 2006. Lars Andersen. *Linear Elastodynamic Analysis*. ISSN 1901-7286. Dept. Civil Eng., Aalborg University, Denmark, 2006.

Anusic et al., 2016. I. Anusic, G. R. Eiksund and M. A. Liingaard. *Comparison of pile driveability methods based on a case study from an offshore wind farm in North Sea*. Proc. of the 17th Nordic Geotechnical Meeting: Challenges in Nordic Geotechnic, 25-28 May, pages 1038–1046, 2016.

API, 1981. API. *Recommended Practice for Planning, Designing and Constructing Fixed Offshore Platforms - Working Stress Design*. American Petroleum Institute, Washington D.C., USA., 12th edition, 1981.

API, 2002. API. *Recommended Practice for Planning, Designing and Constructing Fixed Offshore Platforms - Working Stress Design*. American Petroleum Institute, Washington D.C., USA., 21st edition, 2002.

Atkinson, 2007. John Atkinson. *Mechanics of Soils and Foundations*. ISBN: 9780415362559. CRC Press, Taylor and Francis Group, 2007.

Augustesen, 2006. Anders Hust Augustesen. *The Effect of Time on Soil Behaviour and Pile Capacity - Ph.D. thesis*. Dept. Civil Eng., Aalborg University, 2006.

Baldi et al., 1986. G. Baldi, R. Bellotti, V. Ghionna, M. Jamiolkowski and E. Pasqualini. *Interpretation of CPTs and CPTUs; 2nd part: Drained penetration of sands*. Proc. 4th Int. Geotechnical Seminar, Singapore., pages 143–156, 1986.

Bartoskewitz and Coyle, 1970. Richard E. Bartoskewitz and Harry M. Coyle. *Wave Equation Prediction of Pile Bearing Capacity compared with Field Test Results*. Texas Transportation Institute, Texas A&M Uni. - sponsored by Texas Hwy. Dept. and Federal Hwy. Adm., U.S. Dept. of Transportation, 1970.

Bathe, 2007. Klaus-Jürgen Bathe. *Conserving energy and momentum in nonlinear dynamics: A simple implicit time integration scheme*. Computers and Structures, 85, 437–445, 2007.

Bathe, 2016. Klaus-Jürgen Bathe. *Finite Element Procedures*. ISBN 978-0-9790049-5-7. Watertown, MA, USA, 2nd ed. 4th print edition, 2016.

Bathe and Baig, 2005. Klaus-Jürgen Bathe and Mirza M. Irfan Baig. *On a composite implicit time integration procedure for nonlinear dynamics*. Computers and Structures, 83, 2513–2524, 2005.

Bathe and Cimento, 1980. Klaus-Jürgen Bathe and Arthur P. Cimento. *Some practical procedures for the solution of nonlinear finite element equations*. Computer methods in applied mechanics and engineering, 22, 59–85, 1980.

Bathe and Noh, 2012. Klaus-Jürgen Bathe and Gunwoo Noh. *Insight into an implicit time integration scheme for structural dynamics*. Computers and Structures, 98-99, 1–6, 2012.

Borja, 1988. Ronaldo I. Borja. *Dynamics of Pile Driving by the Finite Element Method*. Computers and Geotechnics, 5, 39–49, 1988.

Byrne et al., 2012. T. Byrne, P. Doherty, K. Gavin and R. Overy. *Comparison of Pile Driveability Methods in North Sea Sand*. Offshore Site Investigation and Geotechnics: Integrated Technologies - Present and Future, 12-14 September, London, 2012.

Chopra, 1995. Anil K. Chopra. *Dynamics of Structures - Theory and Applications to Earthquake Engineering*. Prentice-Hall Inc., Englewood Cliffs, NJ, USA, 1995.

Clausen and Aas, 2001. C.J.F. Clausen and P.M. Aas. *Bearing Capacity of Driven Piles - Piles in sand*. NGI report 525211-2, 2001.

Clausen et al., 2005. C.J.F. Clausen, P.M. Aas and K. Karlsrud. *Bearing Capacity of Driven Piles in Sand, the NGI Approach*. Frontiers in Offshore Geotechnics: ISFOG 2005, (ISBN 0 415 39063 X), 2005.

Cook et al., 2002. Robert D. Cook, David S. Malkus, Michael E. Plesha and Robert J. Witt. *Concepts and applications of finite element analysis*. ISBN 978-0-471-35605-9. John Wiley & Sons, Inc., 4th ed. edition, 2002.

Courant et al., 1928. R. Courant, K. Friedrichs and H. Lewy. *Über die partiellen Differenzengleichungen der mathematischen Physik*. Mathematische Annalen, 100, 32–74, 1928. Translation in IBM Journal, March 1967, pp. 215-234.

CUR C118, 2001. CUR C118. *Bearing capacity of steel pipe piles - Report 2001-8 of the Centre for Civil Eng. Research and Codes*. Gouda, Netherlands., 2001.

Dassault Systèmes, 2017. Dassault Systèmes. *Homepage of 3DS Abaqus*. `http://www.3ds.com/products-services/simulia/products/abaqus/abaquscae/`, 2017. Last visited: 17-03-2017.

Deeks and Randolph, 1993. A. J. Deeks and M. F. Randolph. *Analytical modelling of hammer impact for pile driving*. Int. J. for Numerical and Analytical Methods in Geomechanics, 17, 279–302, 1993.

Deeks, 1992. Andrew John Deeks. *Numerical analysis of Pile Driving Dynamics - Ph.D. thesis*. Dept. Civil Eng., Uni. Western Australia, 1992.

Douglas-Westwood, 2010. Douglas-Westwood. *Offshore Wind Asessment for Norway*. The Research Council of Norway, 2010.

Forehand and Reese, **1964**. P. W. Forehand and J. L. Reese. *Prediction of capacity by the wave equation*. Journal of Soil Mechanics and Foundation Division, 1964.

Gates, **1957**. M. Gates. *Empirical Formula for predicting pile bearing capacity*. Civil Engineering, 27(3), 65–66, 1957.

Gavin, **2016**. Henri. P. Gavin. *Numerical Integration in Structural Dynamics*. Lecture notes for CEE 541. Structural Dynamics, Duke University., 2016.

Gavrilov et al., **2016**. Alexander Gavrilov, Daniel Wilkes and Marta Galindo Romero. *Modelling and Measurements of Underwater Noise from Marine Pile Driving (Final Report) - Prepared for Chevron Australia*. CMST, Curtin University, Perth, Western Australia, 2016.

Gudavalli et al., **2013**. S.R. Gudavalli, O. Safaqah and H. Seo. *Effect of Soil Plugging on Axial Capacity of Open-Ended Pipe Piles in Sands*. Proc. 18th Int. Conf. on Soil Mechanics and Geotechnical Eng., Paris, 2013.

Hannigan et al., **2016**. Patrick J. Hannigan, Frank Rausche, Garland E. Likins, Brent P. Robinson and Matthew L. Becker. *Design and Construction of Driven Pile Foundations – Volume II*. National Highway Institute, Federal Highway Administration, U.S. Dept. of Transportation., 2016.

Heerema, **1978**. Edward P. Heerema. *Predicting pile driveability: Heather as an Illustration of the Friction Fatigue Theory*. Paper presented at the 1978 European Offshore Petroleum Conference and Exhibition, London, 24-27 October, pages 413–423, 1978.

Heerema, **1979**. Edward P. Heerema. *Relationships between wall friction, displacement velocity and horizontal stress in clay and in sand, for pile driveability analysis*. Ground Engineering, 1979.

Heerema, **1981**. Edward P. Heerema. *Dynamic point resistance in sand and in clay, for pile driveability analysis*. Ground Engineering, 1981.

IEA, **2016**. IEA. *World Energy Outlook 2016*. International Energy Agency, 2016.

IHC Merwede, **2017**. IHC Merwede. *IHC Hydrohammer® - Pile driving equipment*. Brochure and datasheet regarding offshore IHC Hydrohammers., 2017. Downloaded: 10-05-2017.

IRENA, **2012**. IRENA. *Wind Power - Cost analysis series, Volume 1, Issue 5/5*. International Renewable Energy Agency, 2012.

Jamiolkowski et al., **1988**. M. Jamiolkowski, V. N. Ghionna, R. Lancellotta and E. Pasqualini. *New Correlations of Penetration Tests for Design Practice*. Proc. First Int. Symposium on Penetration Testing (ISOPT-1), Orlando, FL, USA, pages 263–296, 1988.

Jardine et al., **2005**. R. Jardine, F. Chow, R. Overy and J. Standing. *ICP Design Methods for Driven Piles in Sands and Clays*. Thomas Telford, London, 2005.

Jardine et al., **2015**. Richard J. Jardine, Andrew S. Merritt and Felix C. Schroeder. *The ICP Design Method and Application to a North Sea Offshore Wind Farm*. Proc. International Foundations Congress and Equipment Expo (IFCEE2015), 2015.

Jardine and Chow, 1996. R.J. Jardine and F.C. Chow. *New design methods for offshore piles, Report to the Marine Technology Directorate*. 1996.

Kolk et al., 2005. H.J. Kolk, A.E. Baaijens and M. Senders. *Design criteria for pipe piles in silica sands*. Frontiers in Offshore Geotechnics: ISFOG 2005, (ISBN 0 415 39063 X), 711–716, 2005.

Kreyszig et al., 2011. Erwin Kreyszig, Herbert Kreyszig and Edward J. Norminton. *Advanced Engineering Mathematics*. ISBN 9780470646137. John Wiley & Sons, Inc., New York City, NY, USA, 10th international student version edition, 2011.

Kumar and Gautam, 2015. S. Kumar and S. S. Gautam. *Extension of A Composite Time Integration Scheme for Dynamic Problems*. Proc. Indian National Conference on Applied Mechanics (INCAM), pages 41–46, 2015.

Lehane et al., 2005. B.M. Lehane, J.A. Schneider and X. Xu. *The UWA-05 method for prediction of axial capacity of driven piles in sand*. Proc. Int. Symp. Frontiers in Offshore Geotechnics, ISFOG 2005, pages 683–690, 2005.

Liang and Sheng, 1992. R. Y. Liang and Y. Sheng. *Interpretation of Smith model parameters based on cavity expansion theory*. Proc., 4th Int. Conf. on Application of Stress-Wave Theory to Piles, pages 111–116, 1992.

Litkouhi and Poskitt, 1980. S. Litkouhi and T.J. Poskitt. *Damping constants for pile driveability calculations*. Geotechnique, XXX (1), 1980.

Lunne et al., 1997. Tom Lunne, Peter K. Robertson and John J.M. Powell. *Cone Penetration Testing in Geotechnical Practice*. ISBN 0 751 40393 8. Blackie, Chapman & Hall, London, UK., 1st edition, 1997.

Masouleh and Fakharian, 2007. Shahram Feizee Masouleh and Kazem Fakharian. *Application of a continuum numerical model for pile driving analysis and comparison with a real case*. Computers and Geotechnics, 35, 406–418, 2007.

Mayne, 2014. P. W. Mayne. *Interpretation of geotechnical parameters from seismic piezocone tests*. Proc. 3rd Int. Symposium on Cone Penetration Testing, Las Vegas, Nevada, USA - 2014, pages 47–73, 2014.

McVay and Kuo, 1999. Michael C. McVay and Ching L. Kuo. *Estimate damping and quake by using traditional soil testings*. Dept. Civil Eng., Uni. Florida - submitted to the Florida Dept. of Transportation, 1999.

Meynard and Corte, 1984. A. Meynard and J.-F. Corte. *Experimental study of lateral resistance during driving*. Paper presented at the Second International Conference on the Application of Stress-Wave Theory of Piles, Stockholm, 1984.

MHI Vestas, 2016. MHI Vestas. *MHI Vestas Offshore Wind V164-8.0 MW*. URL: `http://www.mhivestasoffshore.com/innovations/`, 2016. Downloaded: 12-02-2017.

Middendorp and van Weele, 1986. P. Middendorp and A. F. van Weele. *Application of characteristic stress wave method in offshore practice*. Proc. 3rd Int. Conf. on Numerical Methods in Offshore Piling, Nantes, France., pages 6–18 (in supplement), 1986.

Newmark, 1959. Nathan M. Newmark. *A method of computation for structural dynamics*. Journal of Engineering Mechanics, American Society of Civil Engineers, 85 (EM3), 67–94, 1959.

Olson and Flaate, 1967. R. Olson and K. Flaate. *Pile driving formulas for friction piles in sand*. Journal of the Structural Mechanics and Foundation division (ASCE), 93(SM6), 279–296, 1967.

Ovesen et al., 2012. Niels Krebs Ovesen, Leif Fuglsang, Gunnar Bagge and Anette Krogsbøll. *Lærebog i geoteknik*. ISBN: 978-87-502-1042-9. Polyteknisk Forlag, 2012.

Parola, 1970. Jerry Frank Parola. *Mechanics of Impact Pile Driving - Ph.D. thesis*. Graduate College, University of Illinois at Urbana-Champaign, IL, USA, 1970.

Pile Dynamics, 2010. Pile Dynamics. *GRLWEAP Procedures and Models*. Pile Dynamics Inc., Cleveland, Ohio, USA., 2010.

Pile Dynamics, Inc., 2017. Pile Dynamics, Inc. *Pile Driving Analyzer (PDA)*. URL: `http://www.pile.com/pdi/products/pda/`, 2017. Downloaded: 28-04-2017.

Plaxis, 2017. Plaxis. *Plaxis geo-engineering software*. URL: `https://www.plaxis.com/`, 2017. Downloaded: 17-03-2017.

Randolph and Simons, 1986. M. F. Randolph and H. A. Simons. *An improved soil model for one-dimensional pile driving analysis*. Proc. of the 3rd International Conference on Numerical Methods in Offshore Piling, Nantes, pages 3–15, 1986.

Randolph et al., 1994. M. F. Randolph, J. Dolwin and R. Beck. *Design of driven piles in sand*. Géotechnique, 44 (3), 427–448, 1994.

Robertson et al., 1986. P.K. Robertson, R.G. Campanella, D. Gillespie and J. Greig. *Use of In-situ testing in Geotechnical Engineering*. Proc. GSP6, In-Situ '86, ASCE, Reston, VA, USA, 1986.

Schmertmann, 1978. J. H. Schmertmann. *Guidelines for cone penetration test, performance and design*. Fed. Hwy. Adm., Washington D.C., USA, 1978.

Schneider and Harmon, 2010. J.A. Schneider and I.A. Harmon. *Analyzing Driveability of Open Ended Piles in Very Dense Sands*. Journal of the Deep Foundation Institute, (4), 32–44, 2010.

Schneider et al., 2010. J.A. Schneider, D.J. White and Y. Kikuchi. *Analysis of Large Diameter Pipe Pile Drivability in Tokyo Bay Using Piezocone Data*. Proc. GeoFlorida 2010 (GSP 199), ASCE, pages 1488–1497, 2010.

Schofield and Wroth, 1968. A. N. Schofield and C. P. Wroth. *Critical State Soil Mechanics*. The McGraw-Hill Book Company, London, UK, 1968.

Seaway Heavy Lifting, 2009. Seaway Heavy Lifting. *Pile Driveability and Installation*. Booklet promoting awareness of driveability issues., 2009.

Seaway Heavy Lifting, 2017. Seaway Heavy Lifting. *Our Equipment*. URL: `https://www.seawayheavylifting.com.cy/equipment/`, 2017. Downloaded: 20-03-2017.

Silva and Bezerra, **2008**. William Taylor Matias Silva and Luciano Mendes Bezerra. *Performance of Composite Implicit Time Integration Scheme for Nonlinear Dynamic Analysis*. Mathematical Problems in Engineering, 2008.

Smith, **1960**. E.A.L. Smith. *Pile Driving Analysis by the Wave Equation*. Journal of the Soil Mechanics and Foundations Division (ASCE), 86, 1960.

Sørensen and Hansen, **1957**. T. Sørensen and B. Hansen. *Pile driving formula - an investigation based on dimensional considerations and a statistical analysis*. Proc. of the 4th International Conf. on Soil Mechanics and Foundations, London., 2, 61–65, 1957.

Stevens et al., **1982**. Robert S. Stevens, Edward A. Wiltsie and Thomas H. Turton. *Evaluating Pile Driveability for Hard Clay, Very Dense Sand, and Rock*. Paper presented at the 1982 Offshore Technology Conference, Houston, TX, USA, 3-6 May, pages 465–482, 1982.

Take et al., **1999**. W. A. Take, A. J. Valsangkar and M. F. Randolph. *Analytical solution for pile hammer impact*. Computers and Geotechnics, 25, 57–74, 1999.

Thomassen, **2016**. Kristina Thomassen. *Experimental Investigations of Tension Piles in Sand Subjected to Static and Cyclic Loading - Ph.D. thesis*. Dept. Civil Eng., Aalborg University, 2016.

Toolan and Fox, **1977**. F. E. Toolan and D. A. Fox. *Geotechnical planning of piled foundations for offshore platforms*. Proc. Instn. Civ. Eng., 62 (1), 221–244, 1977.

Wijewickreme, **1986**. Dharmapriya Wijewickreme. *Constant volume friction angle of granular materials - M.Sc. thesis*. Dept. Civil Eng., Uni. British Columbia, Vancouver, Canada., 1986.

WindEurope, **2017**. WindEurope. *The European offshore wind industry - Key trends and statistics 2016*. Wind Europe (Wind power industry trade organisation), 2017.

Zhang et al., **2017**. Jie Zhang, Yinghua Liu and Donghuan Liu. *Accuracy of a composite implicit time integration scheme for structural dynamics*. Int. J. for Numerical Methods In Engineering, 109, 368–406, 2017.

AALBORG UNIVERSITY
STUDENT REPORT

Development of driveability model for piles for offshore wind turbines

Master's thesis
Appendices

by
Mads Helsager Harpøth

AALBORG UNIVERSITY
STUDENT REPORT

The School of Engineering and Science
Study Board of Civil Engineering
Thomas Manns Vej 23, 9220 Aalborg Ø
http://www.ses.aau.dk/

Title:

Development of driveability model
for piles for offshore wind turbines

Author:

Mads Helsager Harpøth

Project period:

February 2017 - June 2017

Delivered as partial requirement for obtaining the degree of Master of Science in Engineering (Structural and Civil Engineering) at Aalborg University, Denmark.

Supervisors:

Lars Vabbersgaard Andersen
Associate Professor, Aalborg University

Martin Underlin Østergaard
Geotechnical Engineer, COWI A/S

Front page picture:
Aerial photo of a part of the Anholt Offshore Wind Farm, Kattegat. Courtesy of DONG Energy A/S.

Thesis pages: 101
Appendix pages: 43
Completed: 8 June 2017

Synopsis:

This project contains a study of driveability analysis of offshore monopiles driven in sands, which identifies the key components, methods and models involved. The most commonly applied computer program used in these predictions is not truly dynamic and uses some assumptions which may not be appropriate for all situations. An input to the program, the static resistance to driving (SRD), along with a set of parameters relating the resistance to the stiffness and damping within the soil, are not uniquely defined. A thorough investigation into various SRD models is performed, which finds that the models are all semi-empirical and that they can not be expected to be reliable for conditions dissimilar to the conditions from which they were derived. A fully dynamic model seeking to overcome some of the simplifications, using three different discretization regimes for pile, side friction and tip resistance, and using a more advanced transient solving algorithm is developed and tested for sensitivity to model parameters. The SRD models are applied within the model to investigate their ability to reproduce an available driving record from a pile installed in the North Sea, and large variations in accuracy are found.

Appendices

Appendix A Estimating unit weight, soil type and friction angle from CPT **A1**

A.1 Unit weight and soil type A1

A.2 Effective friction angle A1

Appendix B Newton-Raphson iterative scheme **A4**

Appendix C Incremental numerical integration by the Newmark-β method **A6**

Appendix D Derivation of modified Bathe composite scheme **A10**

D.1 First substep A10

D.2 Second substep A12

Appendix E Enclosed set of scripts **A14**

Appendix F Results of convergence and sensitivity studies **A16**

F.1 Case (a) - Constant q_c and δ A16

F.2 Case (b) - Linearly varying q_c and δ A23

F.3 Case (c) - Single, much stronger layer A26

F.4 Case (d) - Numerical model parameters A29

F.5 Case (e) - Load parameters and structural damping A36

A. Estimating unit weight, soil type and friction angle from CPT

This appendix contains a few correlations applicable for correlating CPT measurements to soil parameters required for driveability analysis.

A.1 Unit weight and soil type

All the presented methods for obtaining SRD requires unit weight as input in order to calculate the overburden pressure σ'_{v0}. Jardine et al. [2005] recommends laboratory unit weight measurements. If these measurements are not available, the unit weight may be estimated from the Robertson charts [Robertson et al., 1986], as seen in Figure A.1 and Table A.1. It should be noted that this chart uses non-normalised values of the CPT data, which for great depths can be ill-suited for classification purposes because of the influence of overburden pressure on the measurements. Various other correlations exists, e.g. to pore pressure ratio for fine-grained soils or to shear wave velocity (seismic) tests (SCPT).

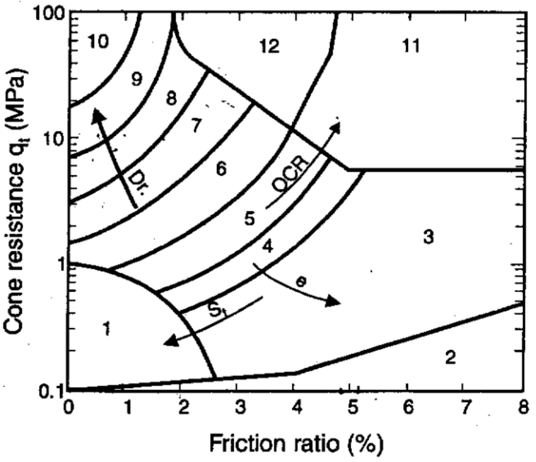

Figure A.1. Soil classification by CPT measurements using the Robertson 86 chart. Friction ratio: $R_f = \frac{f_s}{q_c}$. Reproduced from Lunne et al. [1997].

Zone	Soil behaviour type	γ [kN/m^3]
1	Sensitive fine grained	17.5
2	Organic material	12.5
3	Clay	17.5
4	Silty clay to clay	18.0
5	Clayey silt to silty clay	18.0
6	Sandy silt to clayey silt	18.0
7	Silty sand to sandy silt	18.5
8	Sand to silty sand	19.0
9	Sand	19.5
10	Gravelly sand to sand	20.0
11	Very stiff fine grained	20.5
12	Sand to clayey sand	19.0

Table A.1. Soil classification and approximate unit weight according to the Robertson 86 empiricial charts [Lunne et al., 1997].

A.2 Effective friction angle

The simpler SRD models requires the effective friction angle as input. Lunne et al. [1997] suggest for coarse-grained soils to make an estimate based on the relative density as seen in Figure A.2.

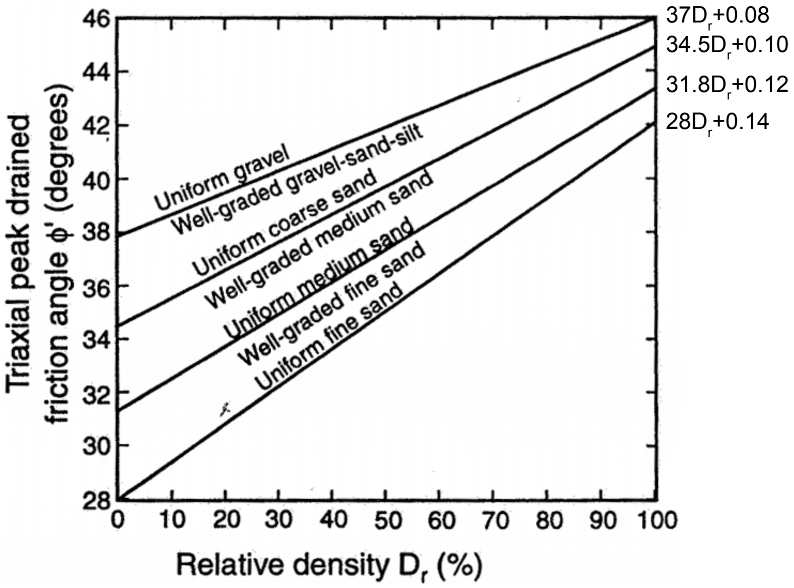

Figure A.2. Empirical relation between relative density and effective friction angle according to Schmertmann [1978]. From Lunne et al. [1997].

Relative density may be estimated by [Baldi et al., 1986]:

$$D_r = \frac{1}{C_2} \ln \left(\frac{q_c}{C_0 \left(\sigma'\right)^{C_1}} \right) \tag{A.1}$$

where

C_0, C_1, C_2	Empirical constants, normally consolidated: $C_0 = 157, C_1 = 0.55, C_2 = 2.41$ and $\sigma' = \sigma'_{v0}$ overconsolidated: $C_0 = 181, C_1 = 0.55, C_2 = 2.61$ and $\sigma' = \left(\sigma'_{v0} + 2\sigma'_{h0}\right)/3$
q_c	Cone resistance [kPa]
σ'_{v0}	Overburden pressure [kPa]
σ'_{h0}	Effective horizontal stress, $\sigma'_{h0} = K_0 \sigma'_{v0}$ [kPa]
K_0	Earth pressure coefficient

D_r is according to API [2002, Errata and Supplement 3] more commonly estimated by the formula by Jamiolkowski et al. [1988]:

$$D_r = \frac{1}{2.93} \ln \left(\frac{q_c}{205 \left(\frac{\sigma'_{v0} + 2\sigma'_{h0}}{3} \right)^{0.51}} \right) \tag{A.2}$$

where

q_c, σ'_{v0}, σ'_{h0}	in [kPa]

Several other correlations exist - the most caution in use of these should be taken when silty sands are present.

K_0 may be estimated by iteration of:

$$K_0 = \begin{cases} 1 - \sin\varphi' & \text{for NC} \\ (1 - \sin\varphi')\, OCR^{1-\sin\varphi'} & \text{for OC} \end{cases} \tag{A.3}$$

$$OCR = 5.04 K_0^{1.54} \tag{A.4}$$

where an estimate on ϕ' may be [Mayne, 2014]:

$$\varphi' = 17.6 + 11.0 \log\left(\frac{q_c/p_a}{\left(\sigma'_{v0}/p_a\right)^{0.5}}\right) \tag{A.5}$$

where

ϕ'	Effective friction angle [°]

B. Newton-Raphson iterative scheme

The most basic non-linear finite element equation is:

$$[K]\{u\} = \{F\} \tag{B.1}$$

where

$[K] = [K(\{u\})]$ | Non-linear stiffness matrix

It is obvious that this equation can not be solved by inverting $[K]$. Instead, one of several different procedures can be used:

- Incremental/stepwise methods
- Iterative or Newton-Raphson methods
- Mixed methods

The Newton-Raphson method is used in the present project, as it has the property of being unconditionally convergent, given that the function is uniformly convex, concave or linear. Assume an approximation to the solution at iteration n can be found, then a residual (or out-of-balance) load vector can be defined as:

$$\{r\} = [K]\{u\} - \{F\} \tag{B.2}$$

Given that $\{u^n\}$ is an approximate solution to B.2, then the true solution at $u_j^n + \Delta u_j^n$ can be written using the first-order truncated Taylor series in tensor notation:

$$r_i\left(u_j^{n+1}\right) = r_i\left(u_j^n\right) + \left(\frac{\partial r_i}{\partial u_j}\right)^n \Delta u_j^n = 0 \tag{B.3}$$

$$u_j^{n+1} = u_j^n + \Delta u_j^n \tag{B.4}$$

Rewriting:

$$\{r^n\} = -[J(u^n)]\{\Delta u^n\} \tag{B.5}$$

where $[J]$ is the Jacobian matrix:

$$J_{ij}(u^n) = \left(\frac{\partial r_n}{\partial u_j}\right)^n = K_{ij}(u^n) + \sum_{k=1}^{N}\left(\frac{\partial K_{ik}}{\partial u_j}\right)^n u_k^n \tag{B.6}$$

The last term is not symmetric and is the reason why the full Newton-Raphson iteration scheme can be computationally expensive. If both terms are kept anyway, it is possible to write:

$$[J(u)] = [K(u)] + \left[K'(u)\right]\{u\} \tag{B.7}$$

$$\{\Delta u^n\} = -[J(u^n)]^{-1}\{r(u^n)\} = -\left([K(u^n)] + \left[K'(u^n)\right]\{u\}\right)^{-1}\{r(u^n)\} \tag{B.8}$$

where

$[K]$ | Initial stiffness matrix
$[K']$ | Tangent stiffness matrix

This approach allows a correction to the vector of unknown displacements to be obtained from the residual force vector at any iteration step. The idea is that this equation is iterated upon until the residual force becomes tolerable small, i.e. until equilibrium has been reached.

Evaluating Equation (B.7) at each iteration is as mentioned not feasible in the present application. One can approximate the Jacobian by its initial value, i.e. the "initial stiffness" Newton-Raphson method:

$$\{\Delta u^n\} = -\left[J(u^0)\right]^{-1}\{R(u^n)\} \tag{B.9}$$

This approach yields slower convergence rate but smaller computation effort per iteration.

C. Incremental numerical integration by the Newmark-β method

This appendix is based on Gavin [2016] and serves to illustrate an alternative and simpler to implement approach compared to the one described in Section 4.4.2. The method described in this appendix was initially used in the present model, but proved to be unsuccessful in keeping the error of the solution bounded and eventually diverged.

In many cases of structural dynamics a semi-discrete system of equations typically called the equation of motion arises, essentially due to Newtons 2nd law:

$$[M]\{\ddot{u}(t)\} = \{f^{ext}(t)\} - \{f^{int}(t)\} - \{f^{damp}(t)\} \tag{C.1}$$

where

$\{f^{ext}(t)\}$	External forces
$\{f^{int}(t)\}$	Internal forces
$\{f^{damp}(t)\}$	Internal damping force

The nature of the external forces depends on the problem, but the damping and internal forces are typically described by:

$$\{f^{damp}(t)\} = [C]\{\dot{u}(t)\} \tag{C.2}$$

$$\{f^{int}(t)\} = [K]\{u(t)\} - \{R(u(t),\dot{u}(t))\} \tag{C.3}$$

where

$\{R(u(t),\dot{u}(t))\}$	Non-linear restoring force

$R(u(t),\dot{u}(t))$ arises because the stiffness and/or external loads of the system depend on the displacement and/or velocity and are thus denoted the *restoring force*, as it is a non-physical force that describes the difference between the linear internal force and the real internal force. The system matrices in the present application are constant as the pile material is assumed elastic. The restoring forces are thus interpreted as the soil resistance. This is of course a modification of the method, which is equivalent to assuming the *initial stiffness* modification to the iteration scheme explained later. For unconditional stability, this assumption however requires that the resistance forces are continuous with respect to displacement (and velocity), which is not the case in this project - the soil resistance is assumed bilinear.

Equation (C.1) can be rewritten to:

$$[M]\{\ddot{u}(t)\} + [C]\{\dot{u}(t)\} + [K]\{u(t)\} + \{R(u(t),\dot{u}(t))\} = \{f^{ext}(t)\} \tag{C.4}$$

At a point in time, denoted t_{i+1}, the goal is then to evaluate $\{\dot{u}(t_{i+1})\} = \{\dot{u}_{i+1}\}$ and $\{u(t_{i+1})\} = \{u_{i+1}\}$. This is clear if one supposes that $\{u_i\}$, $\{\dot{u}_i\}$ and $\{\ddot{u}_i\}$ is known and that $t_{i+1} = t_i + \Delta t$, as

$\{\ddot{u}_{i+1}\}$ may then simply be evaluated from Equation (C.4) as:

$$\{\ddot{u}_{i+1}\} = -[M]^{-1}\left([C]\{\dot{u}_{i+1}\} + [K]\{u_{i+1}\} + \{R(u_{i+1}, \dot{u}_{i+1})\} - \{f_{i+1}^{ext}\}\right) \tag{C.5}$$

The Newmark-β method [Newmark, 1959] states that the approximated displacement and velocity sought for is:

$$\begin{aligned} \{u_{i+1}\} &\approx \{u_i\} + \Delta t\{\dot{u}_i\} + \Delta t^2\left(\left(\frac{1}{2} - \beta\right)\{\ddot{u}_i\} + \beta\{\ddot{u}_{i+1}\}\right) \\ \{\dot{u}_{i+1}\} &\approx \{\dot{u}_i\} + \Delta t\left((1-\gamma)\{\ddot{u}_i\} + \gamma\{\ddot{u}_{i+1}\}\right) \end{aligned} \tag{C.6}$$

where β and γ for example can take the values stated in Table C.1.

Table C.1. Commonly applied Newmark parameters.

β	γ	Assumes
$\frac{1}{4}$	$\frac{1}{2}$	Constant $\ddot{u}(t)$ in Δt
0	$\frac{1}{2}$	Identical to central diff. method
$\frac{1}{6}$	$\frac{1}{2}$	Linear interpolation of $\ddot{u}(t)$
$\in \left[0, \frac{1}{2}\right]$	$\neq \frac{1}{2}$	Not second order accurate
$\in \left[0, \frac{1}{2}\right]$	$\frac{1}{2}$	Second order accurate

$\beta = \frac{1}{4}$ and $\gamma = \frac{1}{2}$ is often used to gain unconditional stability in linear systems. Because of the non-linearities involved the usual guidelines regarding stability of the method in linear structural dynamics may not necessarily hold. For a non-linear application, an incremental form of the scheme is most convenient, i.e. in terms of:

$$\begin{aligned} \delta\{u_i\} &= \{u_{i+1}\} - \{u_i\} \\ \delta\{\dot{u}_i\} &= \{\dot{u}_{i+1}\} - \{\dot{u}_i\} \\ \delta\{\ddot{u}_i\} &= \{\ddot{u}_{i+1}\} - \{\ddot{u}_i\} \\ \delta\{R(u_i, \dot{u}_i)\} = \delta\{R_i\} &= \{R(u_{i+1}, \dot{u}_{i+1})\} - \{R(u_i, \dot{u}_i)\} \\ \delta\{f_i^{ext}\} &= \{f_{i+1}^{ext}\} - \{f_i^{ext}\} \end{aligned} \tag{C.7}$$

An incremental formulation of the finite difference approximation (C.6) can according to Gavin [2016] be:

$$\begin{aligned} [M]\,\delta\{\ddot{u}_i\} + [C]\,\delta\{\dot{u}_i\} + [K]\,\delta\{u_i\} + \delta\{R_i\} &= \delta\{f_i^{ext}\} \\ \delta\{\dot{u}_i\} &= \frac{\gamma}{\beta\Delta t}\delta\{u_i\} - \frac{\gamma}{\beta}\{\dot{u}_i\} + \Delta t\left(1 - \frac{\gamma}{2\beta}\right)\{\ddot{u}_i\} \\ \delta\{\ddot{u}_i\} &= \frac{\gamma}{\beta\Delta t^2}\delta\{u_i\} - \frac{1}{\beta\delta t}\{\dot{u}_i\} - \frac{1}{2\beta}\{\ddot{u}_i\} \end{aligned} \tag{C.8}$$

Assuming $\beta = \frac{1}{4}$, $\gamma = \frac{1}{2}$ and regrouping:

$$\begin{aligned} &\left(\frac{2}{\Delta t}[C] + [K] + \frac{4}{\Delta t^2}[M]\right)\delta\{u_i\} = \\ &\qquad \left(\frac{4}{\Delta t}[M] + 2[C]\right)\{\dot{u}_i\} + 2[M]\{\ddot{u}_i\} + \delta\{f_i^{ext}\} - \delta\{R_i\} \end{aligned} \tag{C.9}$$

Or in more compact form with the vector and matrix notations dropped, while it is implicitly understood that the procedure is performed for all DOF simultaneously:

$$\begin{aligned} \widetilde{K}\delta u_i &= \widetilde{f}_i(\delta u_i) \\ \widetilde{K} &= \left(\frac{2}{\Delta t}C + K + \frac{4}{\Delta t^2}M\right) \\ \widetilde{f}_i(\delta u_i) &= \left(\frac{4}{\Delta t}M + 2C\right)\dot{u}_i + 2M\ddot{u}_i + \delta f_i^{ext} - R(u_i + \delta u_i, \dot{u}_i + \delta\dot{u}_i) + R(u_i, \dot{u}_i) \end{aligned} \tag{C.10}$$

This system must be solved for $\delta\{u_i\}$.

Newton-Raphson iteration for solving Equation (C.10)

The incremental nonlinear restoring forces δR_i is in this project generally essential to the solution, not small, dependent on displacement and associated values such as instantaneous pile penetration and interpolated velocities/displacements, and must thus be solved using an iterative procedure (as a loop within the incremental loop). For this, a Newton-Raphson procedure according to Gavin [2016] is adopted. For simpler notation in the following, superscripts in parenthesis (i.e. $x^{(n)}$) are Newton-Raphson iteration number:

1. Initially, $\delta u_i^{(n=0)} = 0$ and $\widetilde{f}_i\left(\delta u_i^{(n=0)}\right) = \left(\frac{4}{\Delta t}M + 2C\right)\dot{u}_i + 2M\ddot{u}_i + \delta f_i^{ext}$.
2. The Newton-Raphson recurrence relation states:

   $$\delta u_i^{(n+1)} = \widetilde{K}^{-1}\widetilde{f}_i\left(\delta u_i^{(n)}\right)$$

   with

   $$\widetilde{f}_i\left(\delta u_i^{(n)}\right) = \widetilde{f}_i\left(\delta u_i^{(0)}\right) - R\left(u_i + \delta u_i^{(n)}, \dot{u}_i + \delta\dot{u}_i^{(n)}\right) + R(u_i, \dot{u}_i)$$

   and

   $$\delta\dot{u}_i^{(n)} = \frac{2}{\Delta t}\delta u_i^{(n)} - 2\dot{u}_i$$

3. If

   $$||\delta u_i^{(n+1)} - \delta u_i^{(n)}|| < \varepsilon$$

   (where ε is accuracy) the solution is converged, otherwise $\delta u_i^{(n)} = \delta u_i^{(n+1)}$ and step 2 is repeated.

The convergence of this simple scheme depends on the smoothness of the restoring force $R(u, \dot{u})$. A maximum allowable number of iterations is specified, and if this is surpassed, Δt is lowered for the particular time step and $\widetilde{K}^{-1}$ is recalculated. The benefit of this type of integration scheme is that the system matrices does not need be inverted more than once per simulation (unless too large a time step is applied).

Updating

When a solution to Equation (C.10) has been obtained, the displacements (and associated quantities), velocities and accelerations are updated:

$$\begin{aligned}
u_{i+1} &= u_i + \delta u_i \\
\dot{u}_{i+1} &= \frac{2}{\Delta t}\delta u_i - 2\dot{u}_i \\
\ddot{u}_{i+1} &= -M^{-1}\left(C\dot{u}_{i+1} + Ku_{i+1} + R\left(u_{i+1}, \dot{u}_{i+1}\right) - f_{i+1}^{ext}\right)
\end{aligned} \tag{C.11}$$

D. Derivation of modified Bathe composite scheme

This appendix contains an overall mathematical description of the modified Bathe composite time integration scheme, which as explained in Section 4.4.2 is applied in the present project.

The method is based on the Newmark integration scheme [Newmark, 1959] and the Euler backward scheme, both of which are and have been used extensively in structural dynamics.

The combination of the two schemes and its derivation was presented in Bathe and Baig [2005] and Bathe [2007] with its attributes discussed in, among many, Silva and Bezerra [2008], Bathe and Noh [2012] and Zhang et al. [2017]. The idea behind the scheme comes from early simulations of electronic circuits.

Similarly to Figure 4.18, vector and matrix notation is for the sake of readability omitted in this appendix, as it is implicitly understood that all calculations are performed for all DOF's, i.e.:

K, C, M	System stiffness, damping and mass matrix $= [K], [M], [M]$
f, R, r	Force, nodal soil resistance and residual system vectors $= \{f\}, \{R\}, \{r\}$
$u, \dot{u}, \ddot{u}$	Displ., vel. and acc. system vectors $= \{u\}, \{\dot{u}\} = \{v\}, \{\ddot{u}\} = \{a\}$

D.1 First substep

Given the three generalized substep positions as shown in Figure 4.17 and assuming the trapezoidal rule, the displacement and velocity at the substep can be written as a finite difference approximation:

$$\dot{u}_{t+\gamma\Delta t} = \dot{u}_n + \gamma\Delta t \frac{\ddot{u}_t + \ddot{u}_{t+\gamma\Delta t}}{2} \tag{D.1}$$

$$u_{t+\gamma\Delta t} = u_t + \gamma\Delta t \frac{\dot{u}_t + \dot{u}_{t+\gamma\Delta t}}{2} \tag{D.2}$$

$$\Leftrightarrow u_{t+\gamma\Delta t} = u^*_{t+\gamma\Delta t} + \frac{\gamma^2\Delta t^2}{4}\ddot{u}_{t+\gamma\Delta t} \tag{D.3}$$

where

$$u^*_{t+\gamma\Delta t} = u_t + \gamma\Delta t\dot{u}_t + \frac{\gamma^2\Delta t^2}{4}\ddot{u}_t \tag{D.4}$$

Similarly, the velocity may be written as:

$$\dot{u}_{t+\gamma\Delta t} = \dot{u}^*_{t+\gamma\Delta t} + \frac{\gamma\Delta t}{2}\ddot{u}_{t+\gamma\Delta t} \tag{D.5}$$

where

$$\dot{u}^*_{t+\gamma\Delta t} = \dot{u}_t + \frac{\gamma\Delta t}{2}\ddot{u}_t \tag{D.6}$$

Combining Equations (D.3) and (D.5), the accelerations and velocities may be obtained as:

$$\ddot{u}_{t+\gamma\Delta t} = \frac{4}{\gamma^2\Delta t^2}\left(u_{t+\gamma\Delta t} - u^*_{t+\gamma\Delta t}\right) \tag{D.7}$$

$$\dot{u}_{t+\gamma\Delta t} = \dot{u}^*_{t+\gamma\Delta t} + \frac{2}{\gamma\Delta t}\left(u_{t+\gamma\Delta t} - u^*_{t+\gamma\Delta t}\right) \tag{D.8}$$

The equation of motion at the substep is:

$$M\ddot{u}_{t+\gamma\Delta t} + C\dot{u}_{t+\gamma\Delta t} + Ku_{t+\gamma\Delta t} + R\left(u_{t+\gamma\Delta t}, \dot{u}_{t+\gamma\Delta t}\right) = f_{t+\gamma\Delta t} \tag{D.9}$$

where

$f_{t+\gamma\Delta t}$	Hammer load interpolated to $t+\gamma\Delta t$

Applying Equations (D.7) and (D.8) in Equation (D.9), it is possible to define a *residual* vector, i.e. the out-of-balance force:

$$\begin{aligned} r_{t+\gamma\Delta t} = & \frac{4}{\gamma^2\Delta t^2}M\left(u_{t+\gamma\Delta t} - u^*_{t+\gamma\Delta t}\right) + C\left(\dot{u}^*_{t+\gamma\Delta t} + \frac{2}{\gamma\Delta t}\left(u_{t+\gamma\Delta t} - u^*_{t+\gamma\Delta t}\right)\right) + \\ & Ku_{t+\gamma\Delta t} + R\left(u_{t+\gamma\Delta t}, \dot{u}^*_{t+\gamma\Delta t} + \frac{2}{\gamma\Delta t}\left(u_{t+\gamma\Delta t} - u^*_{t+\gamma\Delta t}\right)\right) - f_{t+\gamma\Delta t} \end{aligned} \tag{D.10}$$

By linearisation (i.e. expanding Equation (D.10) to a Taylor series as per Kreyszig et al. [2011] and then ignoring all terms higher than first order), it is possible to obtain a pseudo-"incremental"(in the sense of "incremental" referring to the common *incremental load iterative method*, which is not the method used in this application) formulation of this residual:

$$\begin{aligned} & \left(K^i_{t+\gamma\Delta t} + \frac{4}{\gamma^2\Delta t^2}M + \frac{2}{\gamma\Delta t}C\right)\Delta u^{i+1}_{t+\gamma\Delta t} \\ & = f_{t+\gamma\Delta t} - Ku^i_{t+\gamma\Delta t} - R\left(u^i_{t+\gamma\Delta t}, \dot{u}^*_{t+\gamma\Delta t} + \frac{2}{\gamma\Delta t}\left(u^i_{t+\gamma\Delta t} - u^*_{t+\gamma\Delta t}\right)\right) - \\ & \frac{4}{\gamma^2\Delta t^2}M\left(u^i_{t+\gamma\Delta t} - u^*_{t+\gamma\Delta t}\right) - C\left(\dot{u}^*_{t+\gamma\Delta t} + \frac{2}{\gamma\Delta t}\left(u^i_{t+\gamma\Delta t} - u^*_{t+\gamma\Delta t}\right)\right) \end{aligned} \tag{D.11}$$

where

i	Iteration counter
$u^{i+1}_{t+\gamma\Delta t}$	$= u^i_{t+\gamma\Delta t} + \Delta u^{i+1}_{t+\gamma\Delta t}$
$K^i_{t+\gamma\Delta t}$	Consistent tangent stiffness matrix (full Newton-Raphson scheme) $= \dfrac{\partial f^i_{t+\gamma\Delta t}}{\partial u^i_{t+\gamma\Delta t}}$

As the pile material is assumed elastic, there is no non-linearity in K and instead the initial-stiffness Newton-Raphson method (see Appendix B) with the, indirectly, added stiffness of the soil resistance is used. The consistent tangent stiffness matrix $K^i_{t+\gamma\Delta t}$ in Equation (D.11) is thus replaced simply by K and the non-linearity is evaluated independently for each iteration. This also has the advantages that a) the stiffness matrix remains symmetric ($\frac{\partial f^i_{t+\gamma\Delta t}}{\partial u^i_{t+\gamma\Delta t}}$ is generally full and not necessarily symmetric) and its determinant remains *exactly* zero, which lowers inversion time and b) it is then necessary to perform all required inversion procedures only once per simulation and not once per iteration, which lowers overall simulation time dramatically.

Equation (D.11) can be written as:

$$K_1^* \Delta u^{i+1}_{t+\gamma\Delta t} = -r_{t+\gamma\Delta t} \tag{D.12}$$

$$\Leftrightarrow \Delta u^{i+1}_{t+\gamma\Delta t} = (K_1^*)^{-1}\left(-r_{t+\gamma\Delta t}\right) \tag{D.13}$$

where

K_1^*	Iteration or "effective stiffness" matrix, substep 1 $\approx K + \frac{4}{\gamma^2\Delta t^2}M + \frac{2}{\gamma\Delta t}C$

Equation (D.12) is iterated upon, i.e. an update for each iteration $i+1$:

$$u^{i+1}_{t+\gamma\Delta t} = u^i_{t+\gamma\Delta t} + \Delta u^{i+1}_{t+\gamma\Delta t} \tag{D.14}$$

$$\dot{u}^{i+1}_{t+\gamma\Delta t} = \dot{u}^i_{t+\gamma\Delta t} + \Delta u^{i+1}_{t+\gamma\Delta t}\frac{2}{\gamma\Delta t} \tag{D.15}$$

$$\ddot{u}^{i+1}_{t+\gamma\Delta t} = \ddot{u}^i_{t+\gamma\Delta t} + \Delta u^{i+1}_{t+\gamma\Delta t}\frac{4}{\gamma^2\Delta t^2} \tag{D.16}$$

This is done until the convergence criteria listed in Figure 4.18 is met.

D.2 Second substep

The derivative of any continuous function f can according to the three-point Backward Euler rule be approximated as:

$$\dot{f}_{t+\Delta t} = c_1 f_t + c_2 f_{t+\gamma\Delta t} + c_3 f_{t+\Delta t} \tag{D.17}$$

$$c_1 = \frac{1-\gamma}{\gamma\Delta t} \quad , \quad c_2 = \frac{-1}{(1-\gamma)\gamma\Delta t} \quad , \quad c_3 = \frac{(2-\gamma)}{(1-\gamma)\Delta t} \tag{D.18}$$

Evaluating the velocity in terms of displacement and acceleration in terms of velocity yields:

$$\dot{u}_{t+\Delta t} = c_1 u_t + c_2 u_{t+\gamma\Delta t} + c_3 u_{t+\Delta t} \tag{D.19}$$

$$\ddot{u}_{t+\Delta t} = c_1 \dot{u}_t + c_2 \dot{u}_{t+\gamma\Delta t} + c_3 \dot{u}_{t+\Delta t} \tag{D.20}$$

Defining

$$\dot{u}^*_{t+\Delta t} = c_1 u_t + c_2 u_{t+\gamma\Delta t} \tag{D.21}$$

$$\ddot{u}^*_{t+\Delta t} = c_1 \dot{u}_t + c_2 \dot{u}_{t+\gamma\Delta t} \tag{D.22}$$

and substituting Equation (D.19) in to (D.20), it is possible to obtain:

$$\ddot{u}_{t+\Delta t} = \ddot{u}^*_{t+\Delta t} + c_3 \dot{u}^*_{t+\Delta t} + c_3^2 u_{t+\Delta t} \tag{D.23}$$

Assembling the equation of motion at time $t+\Delta t$, inserting Equations (D.19), (D.23), the residual of the second substep can be obtained as:

$$\begin{aligned} r_{t+\Delta t} =& M\left(\ddot{u}^*_{t+\Delta t}+c_3\dot{u}^*_{t+\Delta t}+c_3^2u_{t+\Delta t}\right)+C\left(\dot{u}^*_{t+\Delta t}+c_3u_{t+\Delta t}\right)+Ku_{t+\Delta t} \\ &+R\left(u_{t+\Delta t},\dot{u}^*_{t+\Delta t}+c_3u_{t+\Delta t}\right)-f_{t+\Delta t} \end{aligned} \tag{D.24}$$

Like Equation D.10, Equation D.24 may be linearised:

$$\begin{aligned} &\left(K+c_3^2M+c_3C\right)\Delta u^{i+1}_{t+\Delta t} \\ &= f_{t+\Delta t}-Ku^i_{t+\Delta t}-R\left(u^i_{t+\gamma\Delta t},\dot{u}^*_{t+\Delta t}+c_3u_{t+\Delta t}\right)- \\ &M\left(\ddot{u}^*_{t+\Delta t}+c_3\dot{u}^*_{t+\Delta t}+c_3^2u_{t+\Delta t}\right)-C\left(\dot{u}^*_{t+\Delta t}+c_3u_{t+\Delta t}\right) \end{aligned} \tag{D.25}$$

Equation (D.25) may be written as:

$$K_2^*\Delta u^{i+1}_{t+\Delta t} = -r_{t+\Delta t} \tag{D.26}$$

$$\Leftrightarrow \Delta u^{i+1}_{t+\Delta t} = \left(K_2^*\right)^{-1}\left(-r_{t+\Delta t}\right) \tag{D.27}$$

where

K_2^*	Iteration or "effective stiffness" matrix, substep 2 $\approx K+c_3^2M+c_3C$

Equation (D.26) is iterated upon, i.e. an update for each iteration $i+1$:

$$u^{i+1}_{t+\Delta t} = u^i_{t+\Delta t}+\Delta u^{i+1}_{t+\Delta t} \tag{D.28}$$

$$\dot{u}^{i+1}_{t+\Delta t} = \dot{u}^*_{t+\Delta t}+c_3u^{i+1}_{t+\Delta t} \tag{D.29}$$

$$\ddot{u}^{i+1}_{t+\Delta t} = \ddot{u}^*_{t+\Delta t}+c_3\dot{u}^{i+1}_{t+\Delta t} \tag{D.30}$$

This is done until the convergence criteria listed in Figure 4.18 is met.

The procedure outlined above can readily be generalized to contain several sub-steps instead of just two, which can be useful in situations where the increases in internal or external forces are significant over each time step (which implies large differences in the acceleration predictors for the two sub-steps).

Furthermore, Kumar and Gautam [2015] showed that if the Newmark parameters are changed (i.e. from trapezoidal rule $\beta = \frac{1}{4}$ and $\gamma_{Newmark} = \frac{1}{2}$), the numerical dissipation of the system can be altered if stability issues are encountered.

E. Enclosed set of scripts

This appendix contains a description of the general structure of the program, and a description of the enclosed digital scripts. The scripts have been tested in Windows using the 2016a distribution of MATLAB. The files are available on-line through `http://projekter.aau.dk/`.

The digital enclosures consists of three folders:

- Post-processing: Two scripts for assembling data series and plotting basic results from output files
- Simulation program: Input script `master.m` and simulation program files
- Tools: Small scripts intended to help create input data-files

Scripts are subdivided into sections indicated by %%. In the following, scripts (i.e. code which can access the global variable workspace) are indicated as `script.m` and functions (i.e. code which can only access the variables transferred to it) are indicated as `function()`.

The program is organised as:

- An *input script* `master.m`, which is the only interface with the user. Different sections account for necessary inputs regarding pile properties, soil properties, hammer properties and model settings including choice of SRD model. Dependent on the values of the definitions in this script, the program can be configured for any combination of pile, soil and driving system and for back-calculation of driving record or for automatic hammer energy control based on desired penetration rate.
- A top-level program script `top.m`, which is not a user interface script. This script contains several sections:
    - Import of piling records
    - Calculation of derived soil parameters such as overburden pressure, angle of friction etc. and grouping into structure array
    - Initial estimate on the load pulse duration through a small numerical simulation
    - Estimation of wave length, critical element length etc.
    - Grouping of parts of load data into structure array
    - Loading and running of core script depending on SRD model
- For each SRD model a core script `main.m` exists, which, among other, performs the following tasks:
    - Calls functions `makesoil()` which takes soil data as input to generate a structure array containing computational soil matrices such as initial and residual ultimate unit side friction, ultimate unit tip resistance, global quake etc.
    - Calls function `soilupdate()` which takes the generated soil structure as input and updates the friction fatigue degradation factor within that structure according to initial penetration
    - Calls function `makepile()` which takes the pile properties and critical element length based on Courant condition as input and generates pile structure array containing derived physical parameters, FEM coordinates and system matrices and calculates self-weight vector

  - Checks existence and consistency of inputs, obtains computer system information and pre-allocates memory for various variables used in the simulation
  - Defines various computational arrays, iteration counters etc.
  - Pre-simulation loop, ramping the self-weight linearly over a period of 0.1 s per DOF, using the time-marching algorithm shown in Figure 4.18 until pile tip velocity slows to below 0.01 m/s
  - Starts main simulation loop, which loads energy setting, blow simulation duration and initiates time-marching algorithm, and continues until either final penetration has been reached or pile is refused. Main simulation loop includes various storage handling sub-algorithms, hammer energy updates, stress level checks etc.
- The pre-simulation and main simulation calls two functions for each iteration of the kinematic variables, which serves to evaluate the total resistance to driving at any discrete step:
  - `interp2soil()` which takes penetration, kinematic variables in pile DOF resolution, pile coordinates relative to pile top and soil coordinates as input and creates a structure array containing interpolated kinematic variables, integration weights etc.
  - `SRD_AH_sand()` (AH: Alm & Hamre, other models have similar functions), which evaluates the soil resistance due to the interpolated kinematic variables and soil structure array and returns it as integrated pile nodal values. The bulk of this function is identical for all SRD models, the difference being whether the specific model includes friction fatigue and how the initial and residual side friction is defined.
- The main simulation calls a hammer energy update function when necessary. Based on model setting, this is either `updateenergy_fromrecord()` (which interpolates in available driving record) or `updateenergy()` (which determines appropriate energy level based on average penetration rate).
- The main simulation also entails the evaluation of the hammer load at the current and next time step, handled by a Newmark approximation.

The program comes pre-configured for the North Sea test case, and can for demonstration purposes be run directly without changing any parameters or MATLAB environment settings. It should be noted that the simulation time is long and varies with choice of soil model.

F. Results of convergence and sensitivity studies

Various convergence and sensitivity studies have been performed. The cases are:

- **(a)** Entirely constant soil parameters with depth to investigate whether the choice of soil discretization as expected in this case have little influence on the results
- **(b)** Simple linear variation with depth of q_T and δ_{cv} to investigate whether similar discretization to case (a) is sufficient in this case
- **(c)** Simple linear variation as case (b) but with a single, thin layer at a significant depth to examine the soil discretization necessary to capture this variation
- **(d)** Same as (b), but investigating (independently) the influence of:
    - Courant number Cr
    - Precisions ε_F, ε_e and $\varepsilon_{\Delta u}$ of Newton-Raphson scheme
    - Value of γ
    - Number of pile elements per wavelength $n_{ele,w}$
- **(e)** Same as (b), but investigating (independently) the influence of:
    - Longer simulation time for each hammer blow
    - Hammer stiffness k_{ram}
    - Hammer damping ratio ζ_{ram}
    - Structural damping ratio ζ_{pile}

The load control mentioned in Figure 4.18 is switched off. The total duration of an individual load series has been set to 3 times the pulse duration. If one assumes a pulse period as here and a blow rate of approximately 40 bl/min, the actual "zero time" should in reality be 4500 times the pulse duration. This would naturally increase simulation time dramatically and, as it is assumed that only minimal oscillation occurs after the mentioned 3 pulse durations. This assumption is tested in case **(e)** (Section F.5).

The hammer load to cone resistance ratios gives a very short driving time and relatively large penetration per blow, and serves as a validation of the ability of the algorithm to handle rapid and large geometric non-linearities.

F.1 Case (a) - Constant q_c and δ

Consider a soil profile as depicted in Figure F.1. The soil profile corresponds to a completely uniform non-layered soil. The overburden pressure increases with depth, and as the Alm & Hamre model uses a normalisation using overburden pressure, a decrease in tip resistance with depth is expected.

Figures F.2 through F.5 depicts strains, stresses, displacements, velocities and accelerations in the configuration $\Delta z = 0.5\,\mathrm{m}$ and $\Delta z_p = 0.05\,\mathrm{m}$. It appears as though the acceleration is not as accurate as the displacements and velocities. This is expected due to the assumptions of the constant-acceleration first sub-step. Furthermore, the precision of the Newton-Raphson scheme

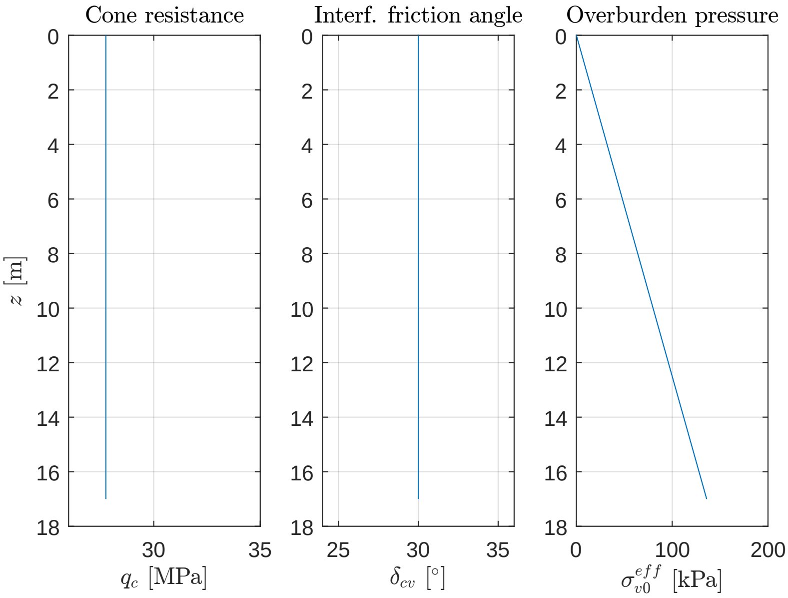

Figure F.1. Idealised soil property profile used for case (a).

is finite, and even insignificant (in soil resistance model terms) errors in displacement are greatly magnified for each approximation of the acceleration. It is seen that the stress wave, as expected, travels almost instantaneously from head to tip, where it is reflected back and forth until it dampens out shortly before the next hammer blow.

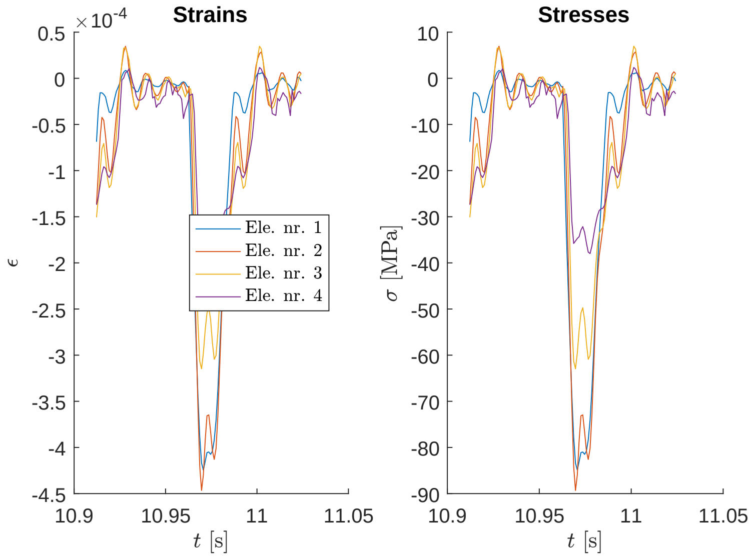

Figure F.2. Case (a): Strains and stresses in all elements in the configuration $\Delta z = 0.5\,\mathrm{m}$ and $\Delta z_p = 0.05\,\mathrm{m}$.

An important aspect when assessing the performance of the model is whether the involved force balances are reasonable in magnitude, shape and duration. The force balance during a single hammer blow is plotted in Figure F.6, where it is seen that the force of the hammer has a sinusoidal shape, with a slight "kink" in the decreasing part of the curve, associated with the pile head motion caused by the reflected stress wave. The build-up of soil resistance is somewhat delayed and elongated compared to the hammer force as expected. A few peaks outside of the main build-up

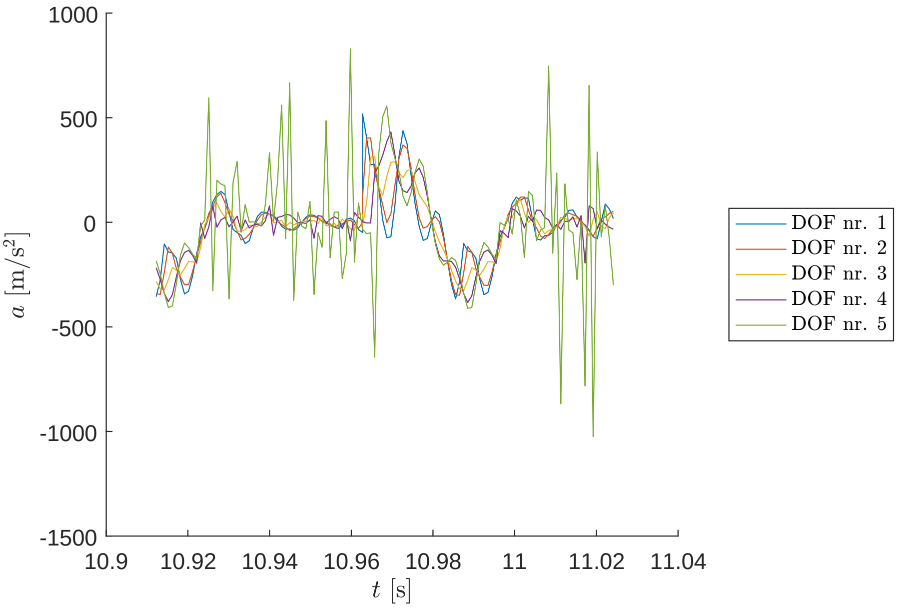

Figure F.3. Case (a): Accelerations in all DOF's in the configuration $\Delta z = 0.5\,\text{m}$ and $\Delta z_p = 0.05\,\text{m}$.

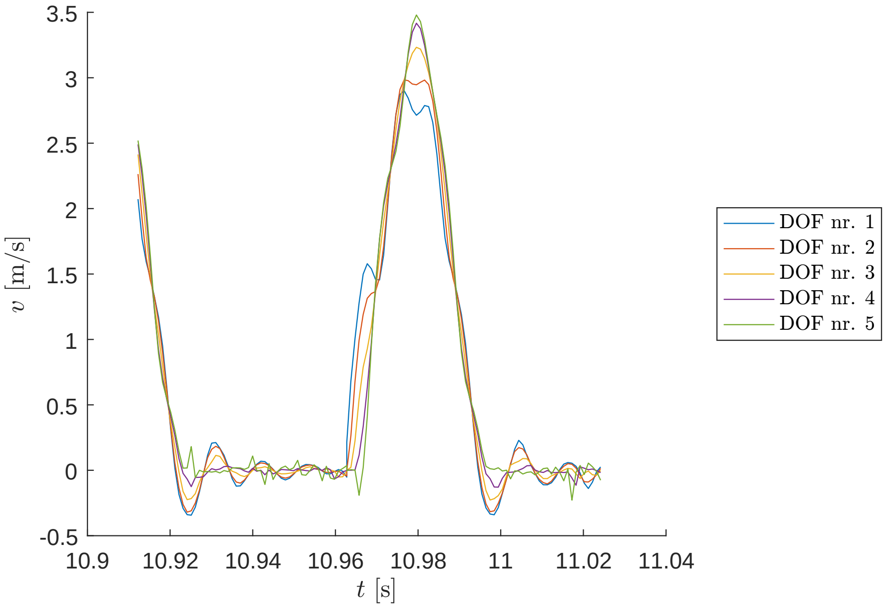

Figure F.4. Case (a): Velocities in all DOF's in the configuration $\Delta z = 0.5\,\text{m}$ and $\Delta z_p = 0.05\,\text{m}$.

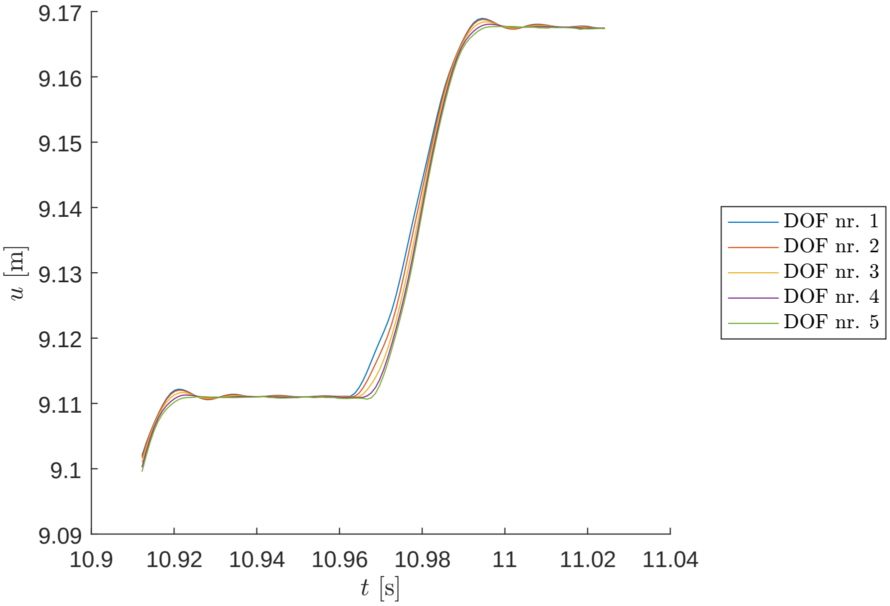

Figure F.5. Case (a): Displacements in all DOF's in the configuration $\Delta z = 0.5\,\mathrm{m}$ and $\Delta z_p = 0.05\,\mathrm{m}$.

can be seen, these are tip resistance developed due to oscillations of the stream wave and associated changes in pile head velocity.

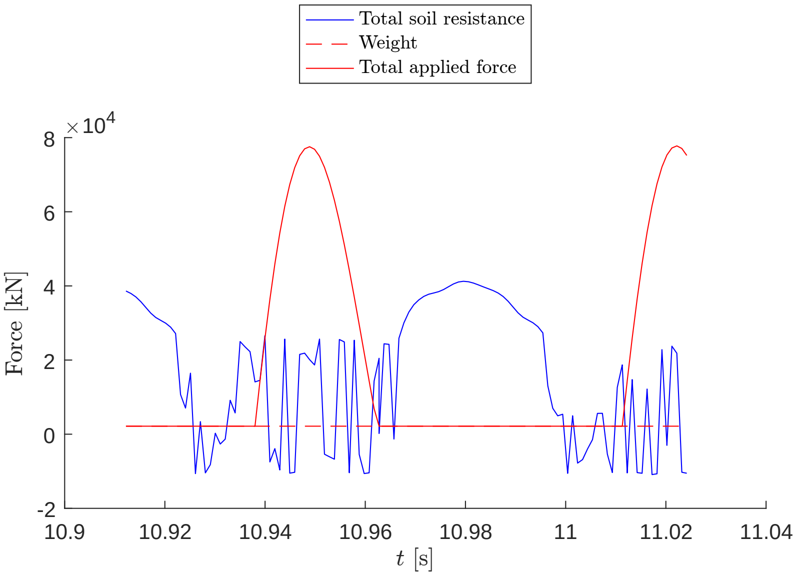

Figure F.6. Case (a): Force balance during a single hammer blow in the configuration $\Delta z = 0.5\,\mathrm{m}$ and $\Delta z_p = 0.05\,\mathrm{m}$.

The main reason for performing a driveability study was mentioned in Section 1.5 as establishing likely pile penetration per hammer blow. This is traditionally plotted as blowcount versus depth, sometimes called a *driveability graph*. Such a plot can be seen in Figure F.7. The combination of large hammer and relatively weak soil gives a very low blowcount, but this is as expected. The side friction is not entirely smooth due to the finite and relatively coarse side discretization, but is as expected plausible on average.

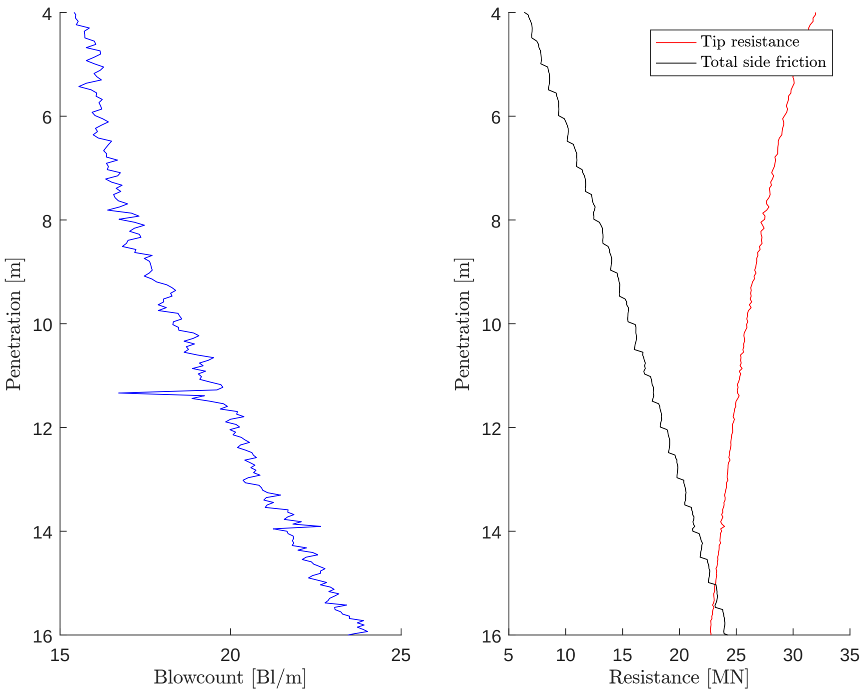

Figure F.7. Case (a): Blowcount vs. depth in the configuration $\Delta z = 0.5\,\mathrm{m}$ and $\Delta z_p = 0.05\,\mathrm{m}$, sampled at the time of maximum pile tip velocity of each blow.

Figure F.8 shows the final number of blows estimated necessary for the final penetration as function of tip and side discretization. As seen, little difference exist in the estimates. The model thus performs as expected, i.e. the soil discretization can be chosen relatively coarse for uniform soils without loss of precision. This is important regarding simulation time, especially in realistic simulations.

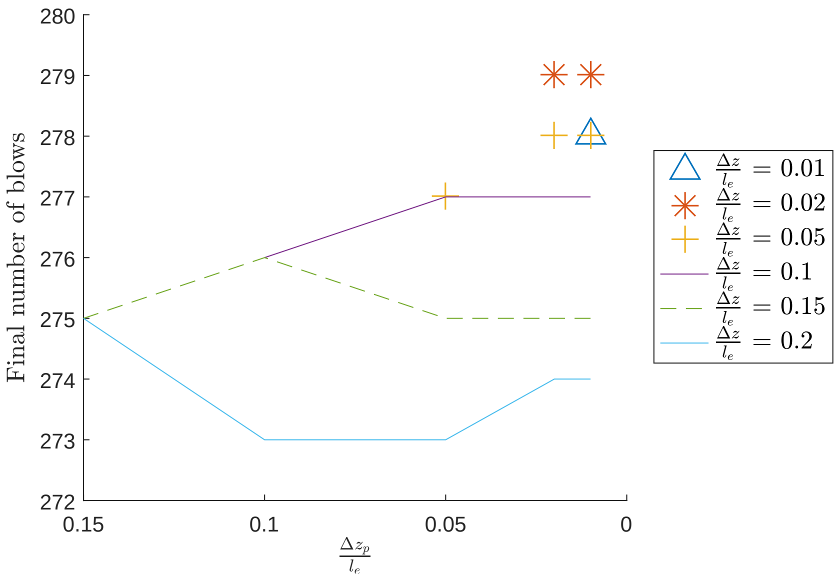

v

Figure F.8. Case (a): Estimates on final number of blows for various soil discretization configurations.

Figure F.9 depicts the blowcounts and resistances for various combinations of tip discretization when keeping the side discretization constant, and vice versa in Figure F.10. It is seen that side friction is more smooth for finer discretizations, but that the results as expected are invariant to soil discretization when the soil parameters are constant/uniformly varying. A few spurious deviations in the blowcount can be seen in Figure F.9, which is to be expected due to random numerical error, which may increase for fine discretization due to the simple fact that a larger volume of calculations is then subject to round-off error.

As seen in Figure F.11, the average values are to all intents and purposes invariant to the chosen discretization when the soil conditions are as in this case.

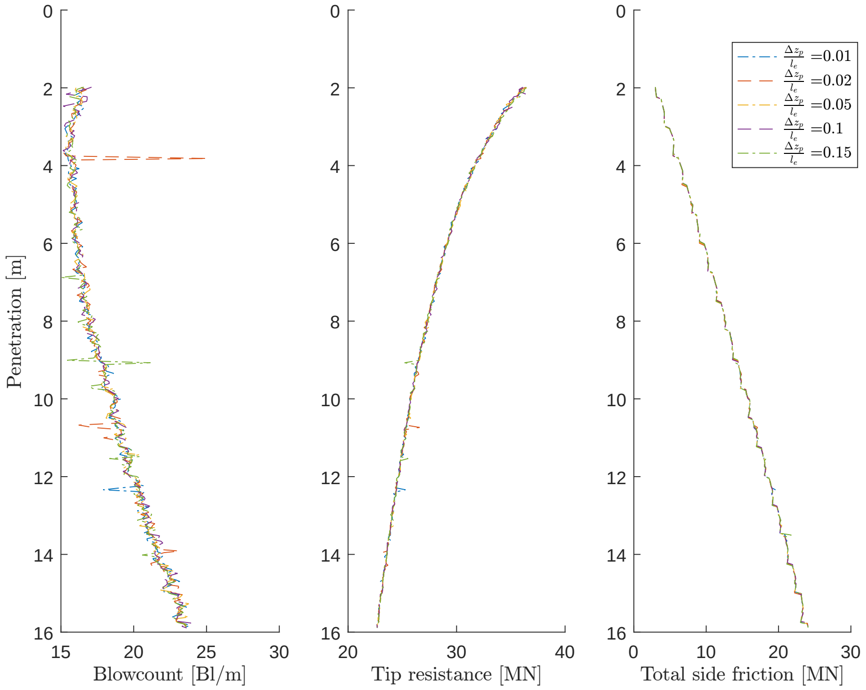

Figure F.9. Case (a): Blowcount, tip resistance and total side friction estimates when assuming a side discretization equal to $\frac{\Delta z}{l_e} = 0.15$. Sampled once for each blow.

A weak tendency seems to be prevalent: Finer discretization results in lower predictions, e.g. less conservative estimates. This being said, such small differences as here may simply be a product of chosen model tolerance.

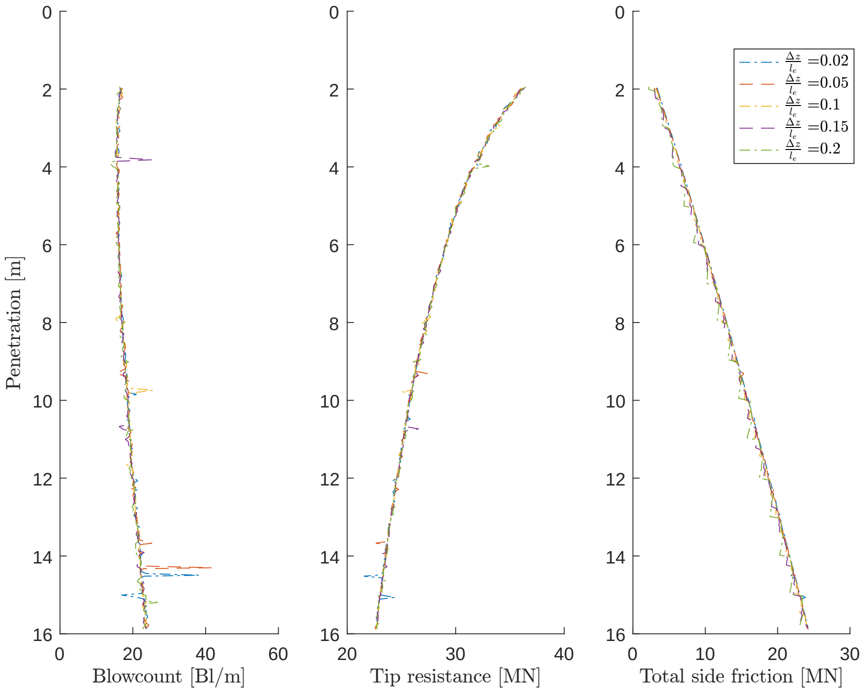

Figure F.10. Case (a): Blowcount, tip resistance and total side friction estimates when assuming a tip discretization equal to $\frac{\Delta z_p}{l_e} = 0.01$. Sampled once for each blow.

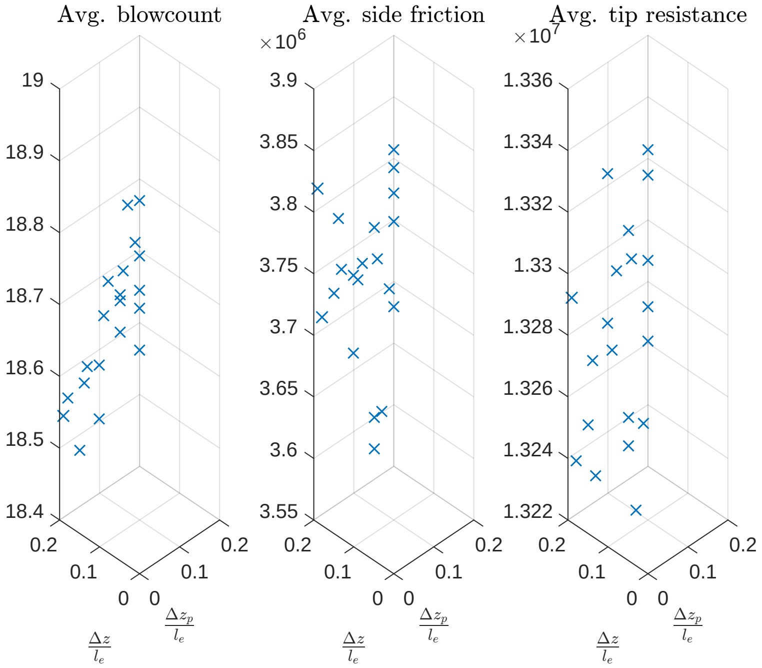

Figure F.11. Case (a): Average blowcount, tip resistance and total side friction for combinations of tip and side discretization.

F.2 Case (b) - Linearly varying q_c and δ

Consider a soil profile as depicted in Figure F.12. The soil profile corresponds to a simple linear increase in strength with depth and constant specific density.

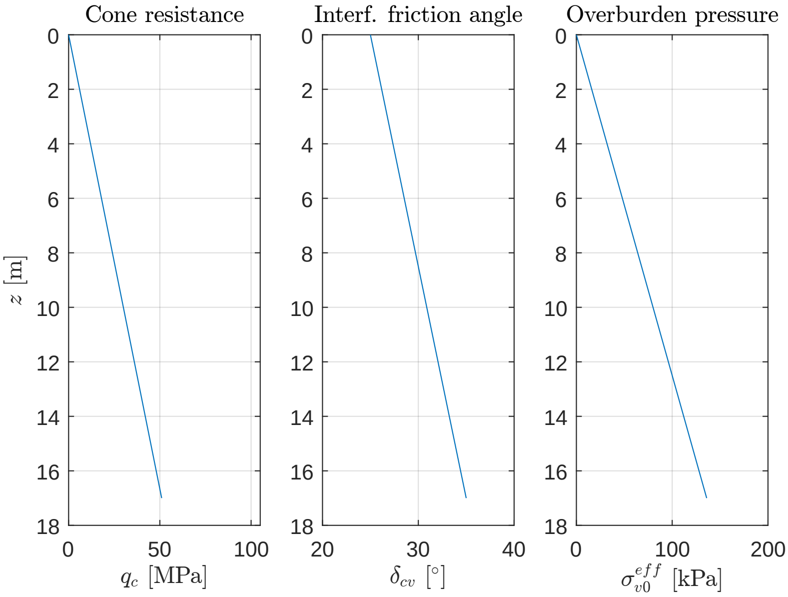

Figure F.12. Assumed soil property profile used for case (b). The profile may not be physically probable, but is only used for convergence purposes.

20 configurations of the soil discretization has been examined, as seen in Table 5.4.

As expected, the discretization considerations are identical to the ones for case (a), as the same behaviour regarding convergence can be seen in Figures F.13 through F.15.

The average and overall values does also not depend on soil discretization, but as the side friction is not longer linearly increasing with depth, the "jumps" in side friction because of discretization are now more significant as seen when comparing Figures F.16 (fine side discretization) and F.17 (20 times coarser).

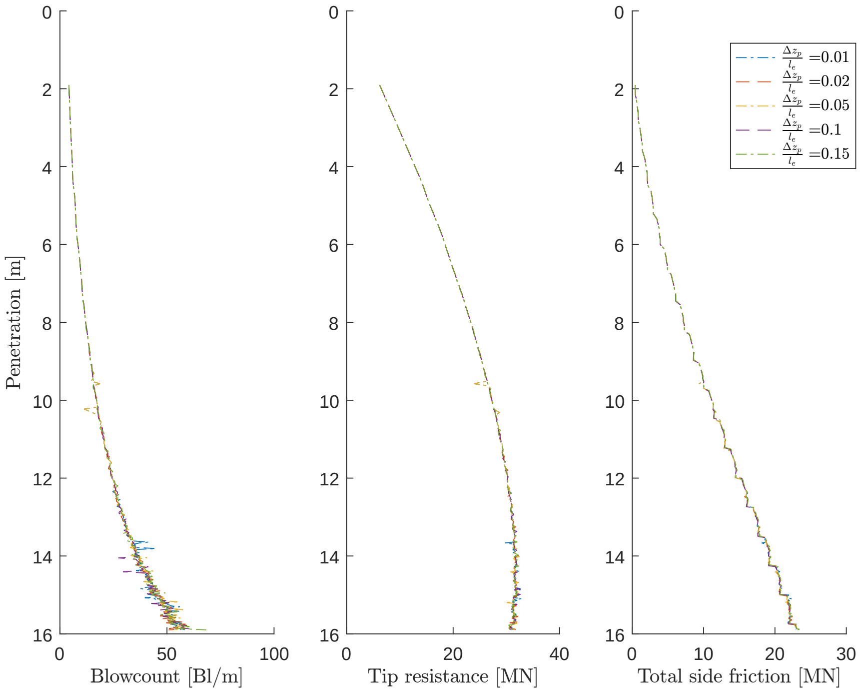

Figure F.13. Case (b): Blowcount, tip resistance and total side friction estimates, when assuming a side discretization equal to $\frac{\Delta z}{l_e} = 0.15$. Sampled once for each blow.

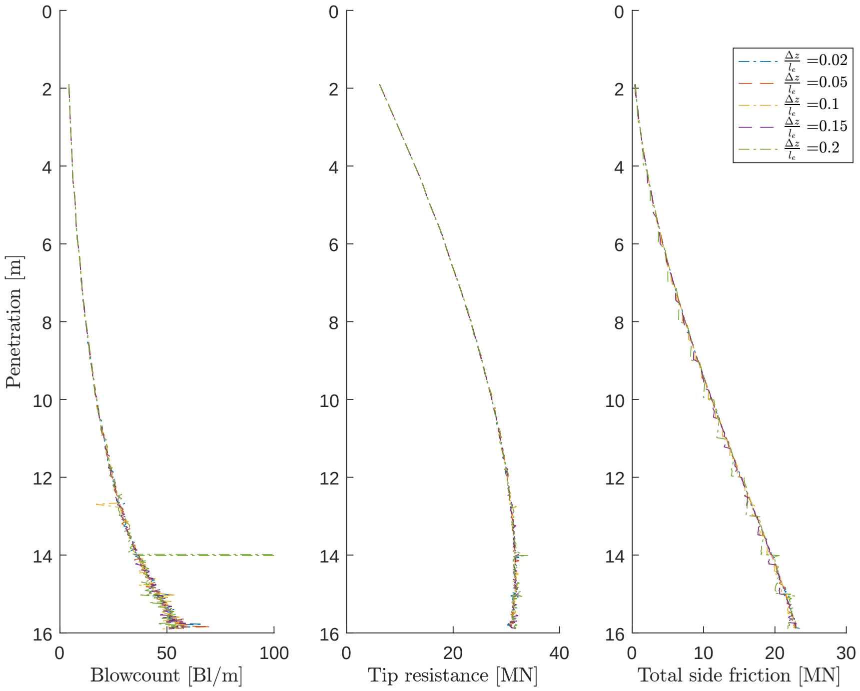

Figure F.14. Case (b): Blowcount, tip resistance and total side friction estimates, when assuming a tip discretization equal to $\frac{\Delta z_p}{l_e} = 0.01$. Sampled once for each blow.

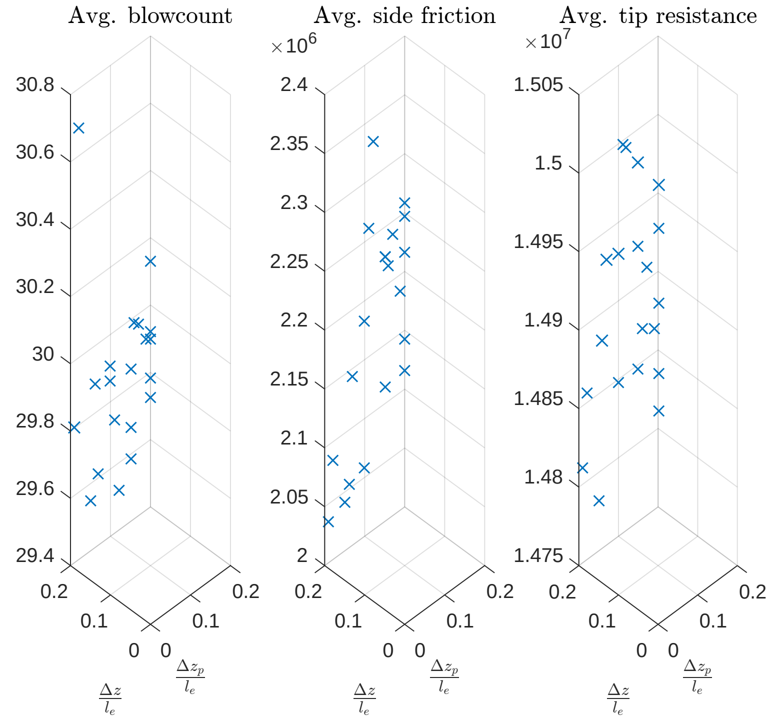

Figure F.15. Case (b): Average blowcount, tip resistance and total side friction for combinations of tip and side discretization.

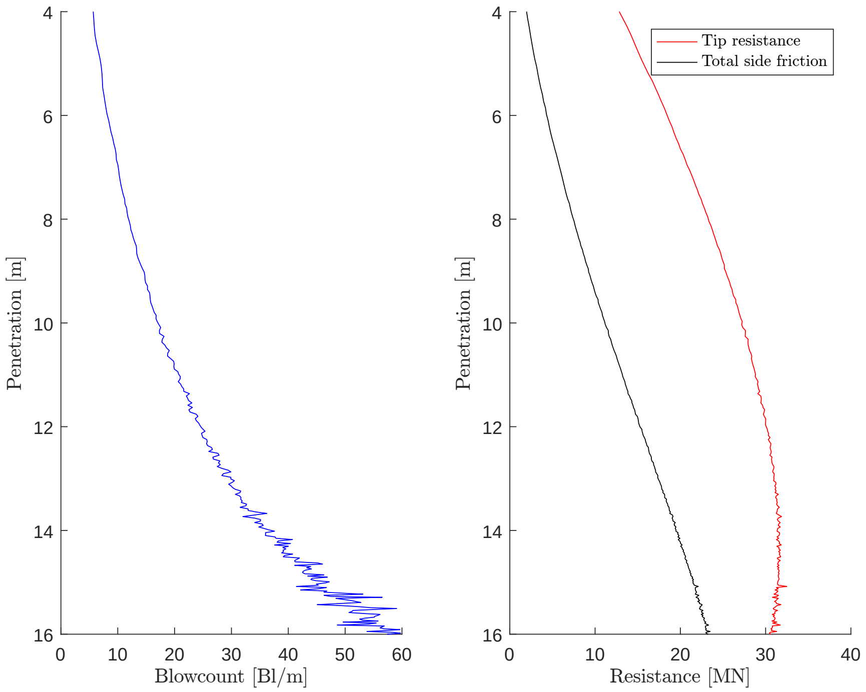

Figure F.16. Case (b): Blowcount and resistance vs. depth in the configuration $\Delta z = 0.05\,\mathrm{m}$ and $\Delta z_p = 0.05\,\mathrm{m}$, sampled at the time of maximum pile tip velocity of each blow.

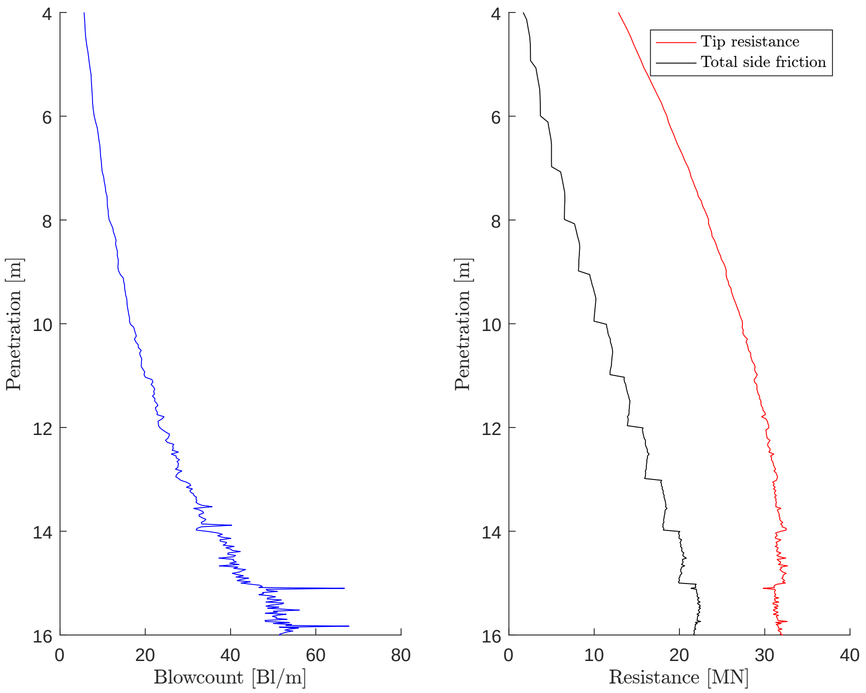

Figure F.17. Case (b): Blowcount and resistance vs. depth in the configuration $\Delta z = 1.00\,\mathrm{m}$ and $\Delta z_p = 0.05\,\mathrm{m}$, sampled at the time of maximum pile tip velocity of each blow.

F.3 Case (c) - Single, much stronger layer

The soil profile used in case (c) can be seen in Figure F.18. The conditions are identical to case (b) except of a single well-bounded much stronger layer at a depth of 10 m - 11 m. It was shown in the two previous sections that a relatively coarse soil discretization can be applied without significant loss of accuracy for the uniform soils in case (a) and (b). The difference in predictions depending on soil discretization for non-uniform soils is much more significant. This can be illustrated by comparing Figures F.19 and F.20, where it is clearly seen that the finer discretization almost immediately after hitting the boundary predicts a much higher blowcount instead of the more physically inconsistent manner of the coarser discretization model, which overestimates the blowcount and tip resistance a meter above and below of the layer.

The convergence rate with regards to total number of blows predicted does strongly depend on tip discretization whereas the side discretization has smaller influence, as seen in Figure F.21. An interesting result is that the convergence rate is apparently not directly proportional to the tip discretization - a minimum can be seen for the value $\Delta z_p / l_e = 0.15$. Furthermore, no clear proportionality between the side discretization and the final number of blows seems to exist, but the trend is that for the present soil conditions, configurations with $\Delta z / l_e < 0.1$ and $\Delta z_p / l_e < 0.05$ seem to have converged, which corresponds to three side friction evaluation points and five tip resistance evaluation points within the significantly different layer.

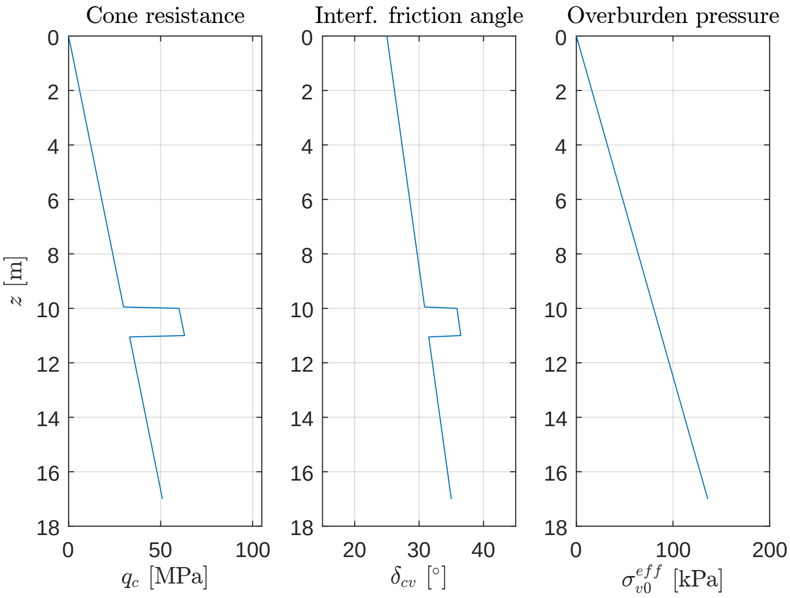

Figure F.18. Idealised soil property profile used for case (c).

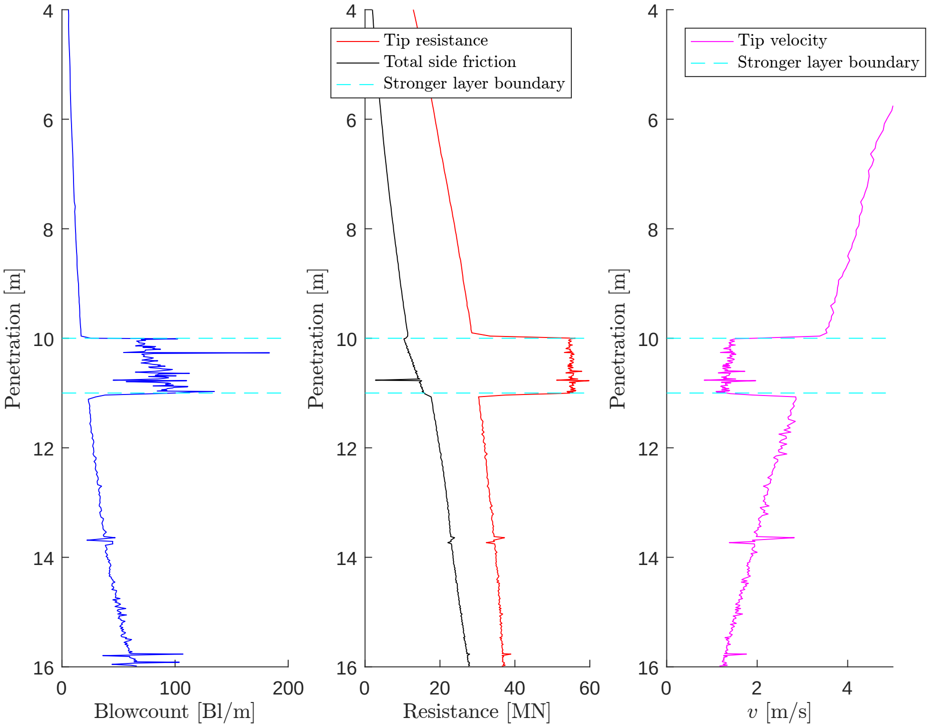

Figure F.19. Case (c): Blowcount and resistance vs. depth in the configuration $\Delta z = 0.05\,\text{m}$ and $\Delta z_p = 0.05\,\text{m}$, sampled at the time of maximum applied load of each blow.

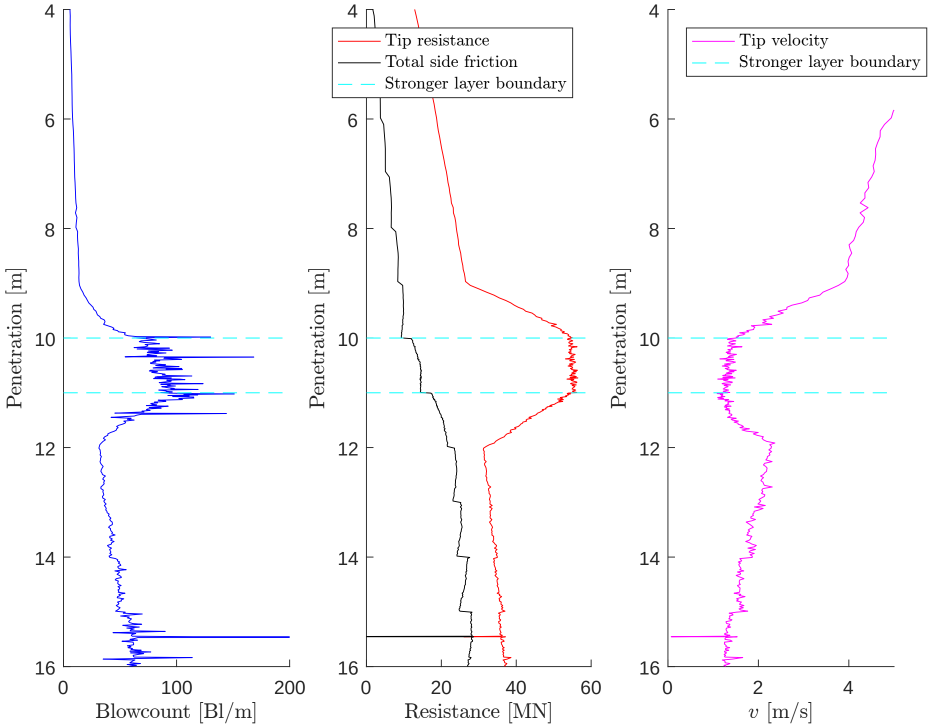

Figure F.20. Case (c): Blowcount and resistance vs. depth in the configuration $\Delta z = 1.00\,\mathrm{m}$ and $\Delta z_p = 1.00\,\mathrm{m}$, sampled at the time of maximum pile tip velocity of each blow.

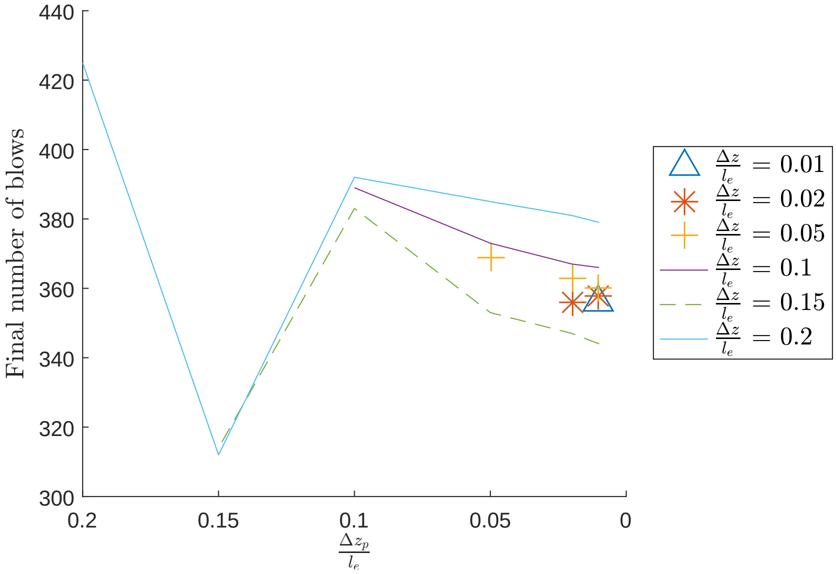

Figure F.21. Case (c): Estimates on final number of blows for various soil discretization configurations.

F.4 Case (d) - Numerical model parameters

Case (d) involves varying the various model parameters not directly related to the soil or hammer models, i.e. the Courant number, the position of the sub-step, the size of pile elements and the required precision in the Newton-Raphson schemes. All simulations of case (d) have been run with a side discretization of $\Delta z = 0.1\,\mathrm{m}$ and tip discretization $\Delta z_p = 0.05\,\mathrm{m}$. The soil conditions can be seen in Figure F.12.

F.4.1 Influence of Courant number

The Courant number (Equation (4.50)) is varied between 1.00 and 0.25. The estimates on necessary number of blows increases slightly with Cr (see Figure F.22). It appears as though it is actually conservative to choose the highest Cr, as the average and total blowcount (Figure F.23) seems to be proportional to Cr. Examining Figure F.24 the influence of choice of Courant number on the calculated tip resistance and side friction can be seen. Even though the simulations with higher Courant numbers predict lower resistances, they also predict higher blowcounts, increasingly with depth. Clearly, for shallow depths, the penetration rate is very high due to the small overburden pressure. For high Courant numbers, little numerical damping is present, and the effect of this higher penetration rate is thus higher (as the amplitude decay of the stress wave is simply smaller). This means that even though the average blowcount may be conservative, the soil resistance is underestimated. This problem will be more prevalent for greater depths and larger piles, so a $Cr < 1$ is advisable.

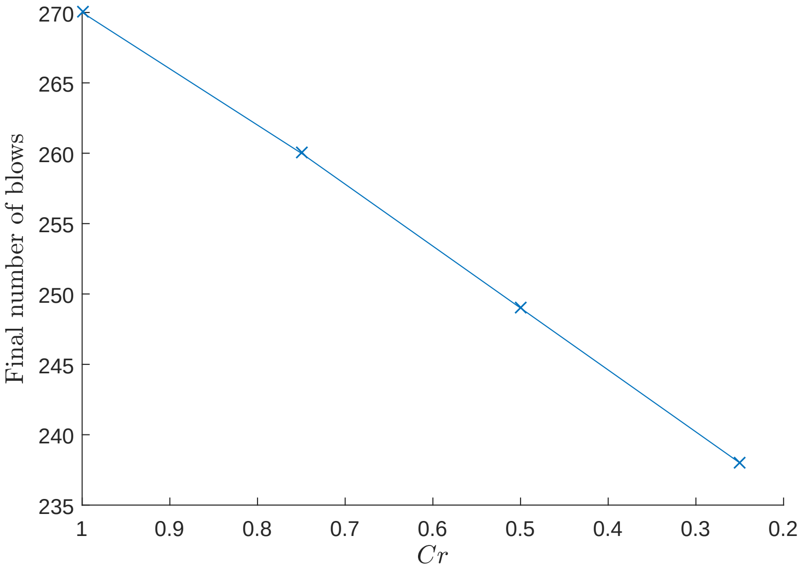

Figure F.22. Case (d): Final number of blows estimate for various Courant numbers.

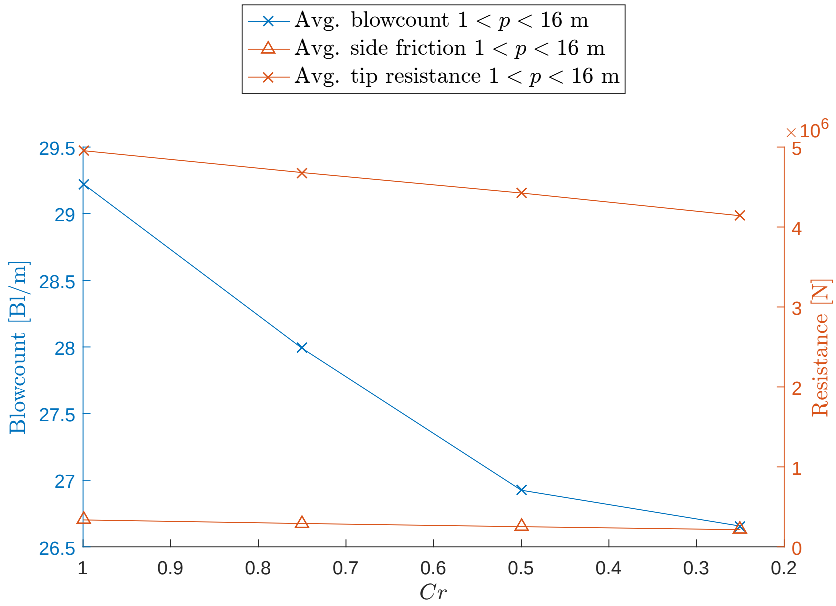

Figure F.23. Case (d): Averages of blowcount and resistances for various Courant numbers.

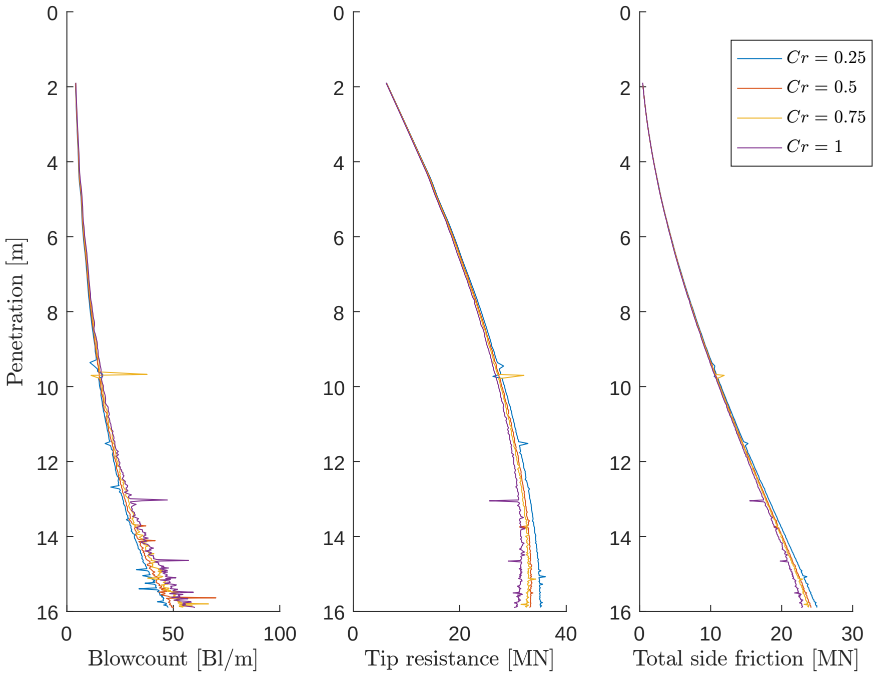

Figure F.24. Case (d): Blowcount and resistance vs. depth for various Courant numbers, sampled at the time of maximum pile tip velocity of each blow.

The computation time should theoretically be inversely proportional to to the time step size, i.e. $Cr = 0.25$ is approximately four times slower than $Cr = 1.00$. A benefit of choosing a Courant number lower than 1.00 is that the load series enters in a higher resolution, which gives less accumulation of numerical errors and less amount of Newton-Raphson iterations in each step, so the computation time is only approximately three times higher for four times lower Courant number.

F.4.2 Influence of position of sub-step

The position of the sub-step $0 < \gamma < 1$ governs the influence of either the implicit or the explicit part of the time integration scheme. Silva and Bezerra [2008] concludes that $\gamma < 0.5$ results in reduction in numerical dissipation and that $\gamma > 0.5$ results in increase in numerical dissipation. Zhang et al. [2017] uses a single-DOF system with no physical damping to assess the numerical damping and period elongation properties of the composite scheme, and finds that when using the trapezoidal approximation for the first sub-step, the most optimal position is $\gamma = 2 - \sqrt{2}$ albeit with similar results for $\gamma = 0.5$. The purpose of this section is to investigate the sensitivity of choice of this parameter in the present model.

The value of γ has an influence on the error accumulated in the penetration, velocity and acceleration of the pile tip as the simulation progresses. For example, Figures F.25 and F.26 depicts the displacement and the estimates of its derivatives at the pile tip during two consecutive blows. The penetration are not in phase as numerical dissipation and/or overshoots based on the value of γ during previous hammer blows have created differences in the result. The acceleration values are the ones predicted by the backward Euler step and are as defined in Figure 4.18 not used for the predictors of the next time step, but it is clear that a) the composite scheme is as expected not accurate for acceleration values (but that the errors in acceleration have minimal impact on the velocity and displacement) and b) the error are more or less random, but somewhat higher for values different from $\gamma = 2 - \sqrt{2}$. The trend of the numerical dissipation being inversely proportional to the value of the sub-step position as described by Silva and Bezerra [2008] is not clear in the present application, as seen in Figure F.27 - no clear trend is present.

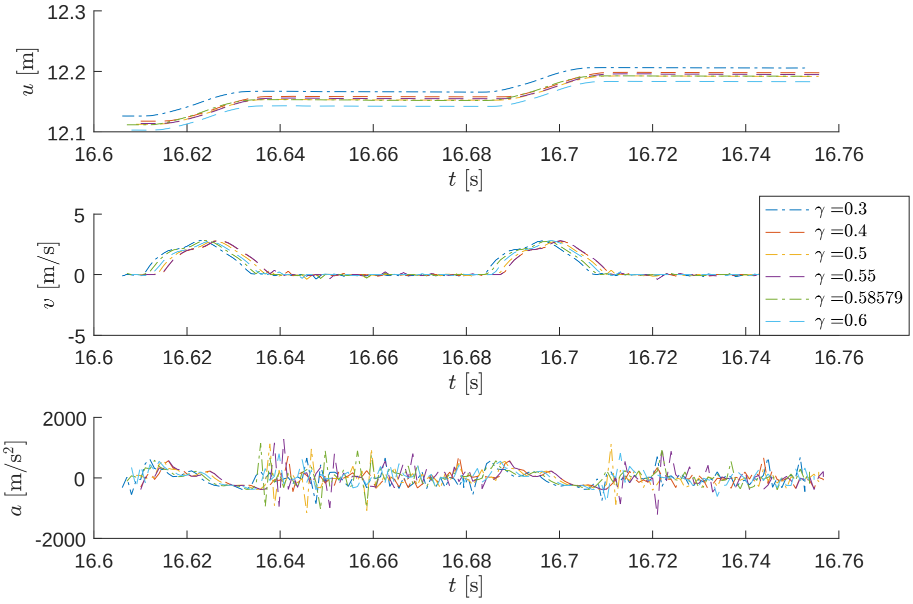

Figure F.25. Case (d): Displacement, velocity and acceleration of the pile finite element DOF representing the pile tip for various values of the sub-step position γ (Part 1).

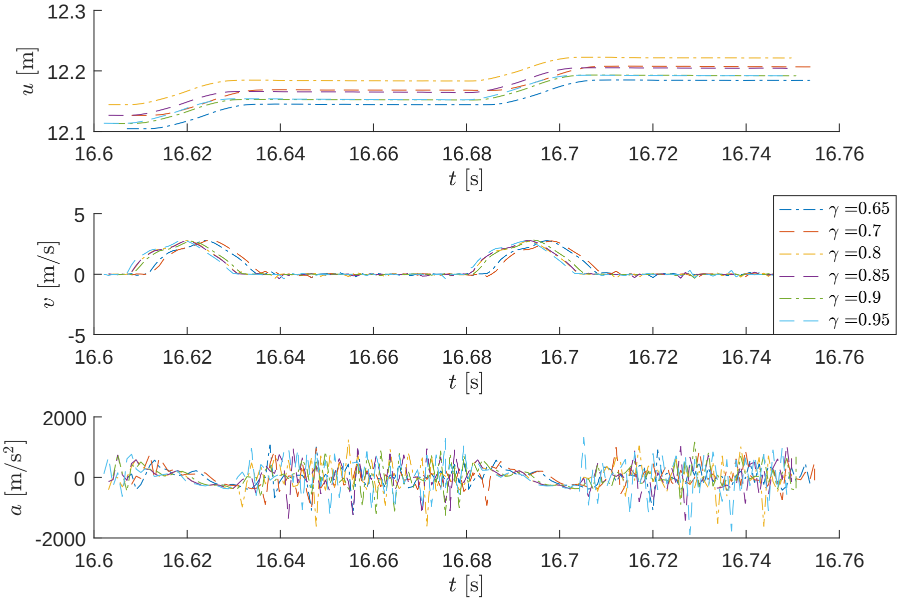

Figure F.26. Case (d): Displacement, velocity and acceleration of the pile finite element DOF representing the pile tip for various values of the sub-step position γ (Part 2).

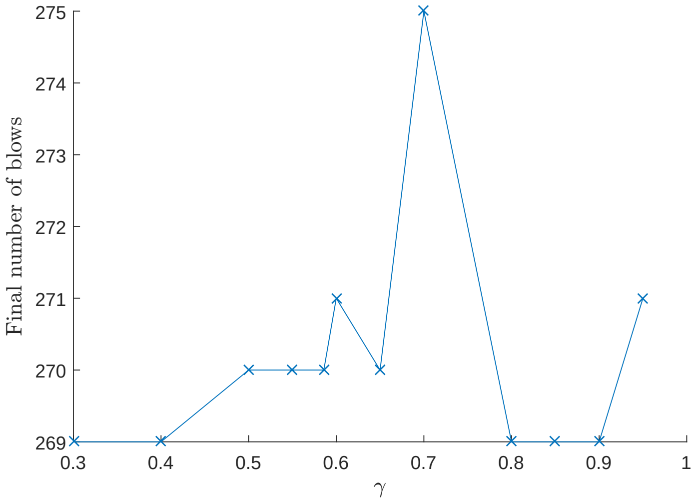

Figure F.27. Case (d): Final number of blows estimate for various values of the sub-step position γ.

As seen in Figure F.28, the choice of γ does not affect the average values of tip resistance and side friction significantly. The reason for the comparatively higher blowcount estimates for a value of $\gamma = 0.7$ and $\gamma = 0.3$ is unknown, but as these points seem to be outliers, it is difficult to outrule random errors as the reason. It is not clear which value of γ is most appropriate, but as the differences apparently are insignificant and the value of $\gamma = 2-\sqrt{2}$ has a slight computational advantage, this value may be used.

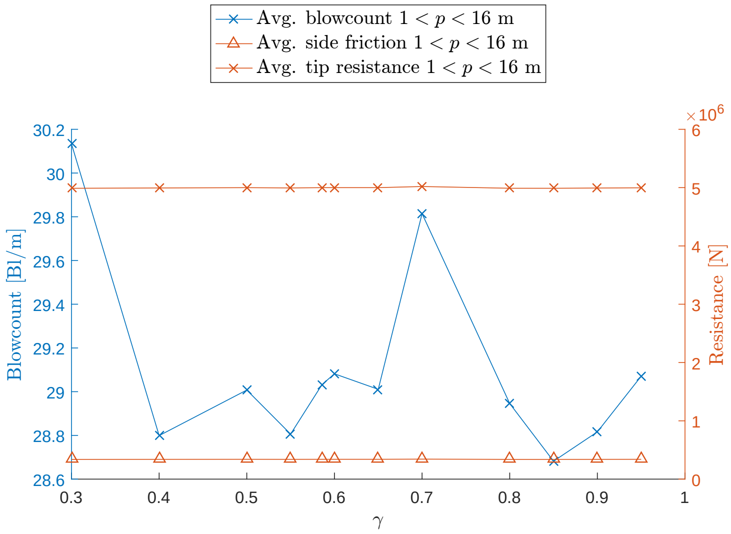

Figure F.28. Case (d): Averages of blowcount and resistances for various values of the sub-step position γ.

F.4.3 Influence of size of pile elements

To investigate whether the size of the pile elements has any significant impact on the results, various number of elements per wavelength have been investigated, as seen in Table F.1. The computation time is naturally dependent on the number of pile DOF's because of the smaller time step, and several times longer solution time is needed for some of the finer discretizations, depending on computer. The effort does not scale linearly as the number of Newton-Raphson iterations may vary independently and because the linear operations are almost independent on size of the matrices.

Table F.1. Investigated pile discretizations.

No. ele. per wavelength	20 (ref.)	30	70	100	120
Max. allow. ele. length [m]	6.31	4.21	1.80	1.26	1.05
Actual ele. length [m]	5	2.5	1.67	1.25	1
No. DOF	5	9	13	17	21

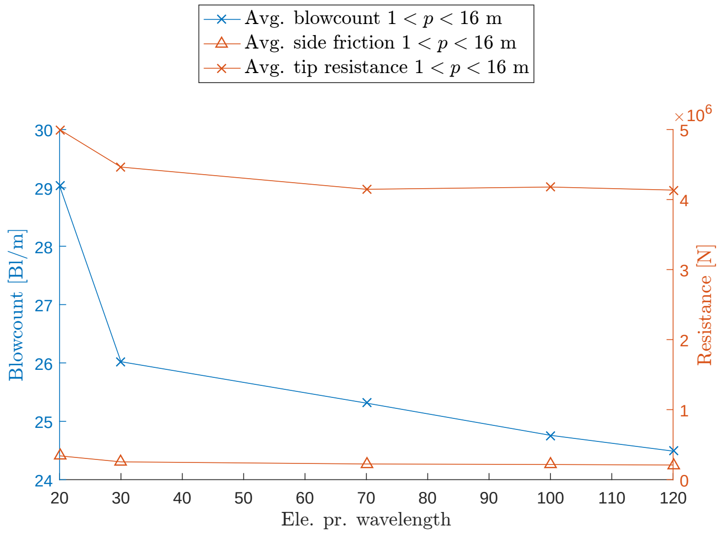

Figure F.29. Case (d): Averages of blowcount and resistances for different pile discretizations.

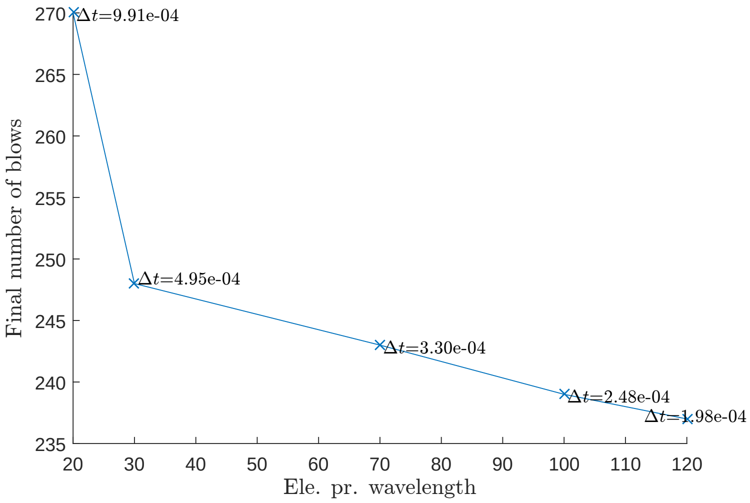

Figure F.30. Case (d): Final number of blows estimates for different pile discretizations.

Figures F.29 and F.30 suggests that the results are relatively invariant to element size. Little difference in the results can be seen for 20-100 pile elements per wavelength, i.e. element sizes of 5 to 1 m, but the trend is that smaller pile elements yield lower total blowcounts - i.e. it is not unsafe (but imprecise) to choose few elements per wavelength. The differences are not necessarily due to the size of the element itself (as it in the previous sections has been established that coarse side discretization compared to pile element length is sufficient in uniform soils), but can also be due to the smaller time step. The smaller time step is necessary in order to keep the Courant number constant.

F.4.4 Influence of precision of Newton-Raphson iteration scheme

The reference values used for the tolerances of the equilibrium iterations is $\varepsilon_F = 0.01$ (force), $\varepsilon_e = 0.001$ (energy) and $\varepsilon_{\Delta u} = 0.001$ (displacement), i.e. a ratio $F : e : \Delta u$ of 10:1:1 as suggested by Bathe and Cimento [1980]. Results of simulations run with various values of tolerances with this ratio can be seen in Figure F.31 and F.32. The tip resistance, side friction and average blowcount seems to be practically invariant to the value of the tolerance in the investigated interval, with slightly higher blowcounts estimated for fine precision values. The estimated total number of blows can be seen in Figure F.33 and is naturally similar to the average blowcount.

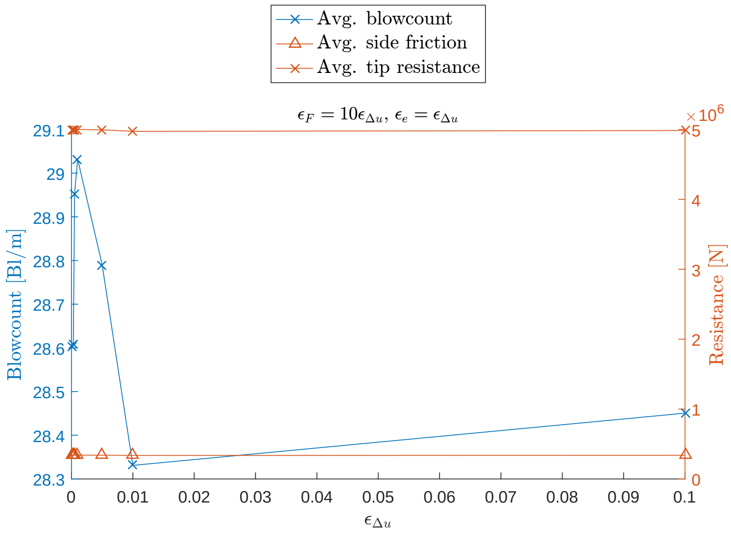

Figure F.31. Case (d): Averages of blowcount and resistances for different values of the Newton-Raphson tolerances.

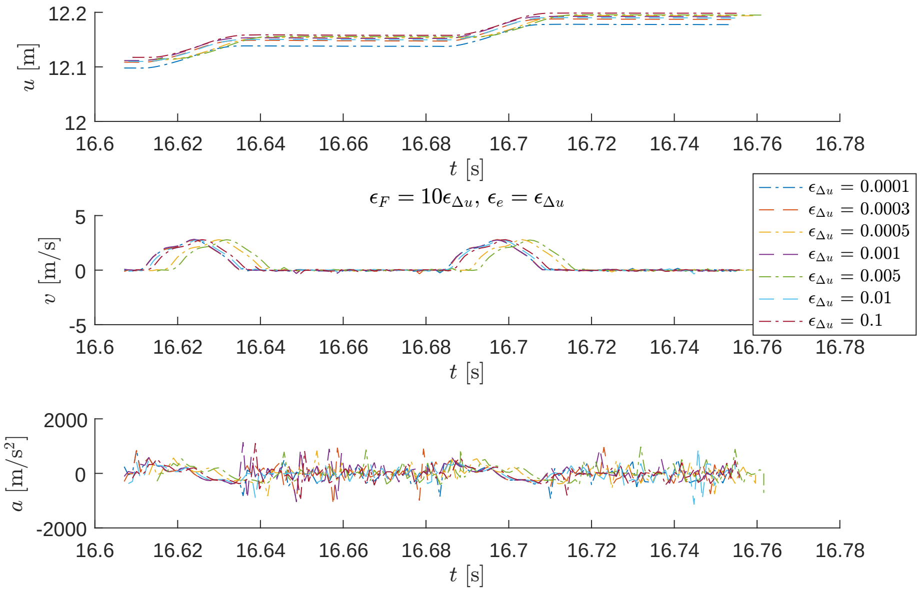

Figure F.32. Case (d): Displacement, velocity and acceleration of the pile finite element DOF representing the pile tip for various values of the Newton-Raphson tolerances.

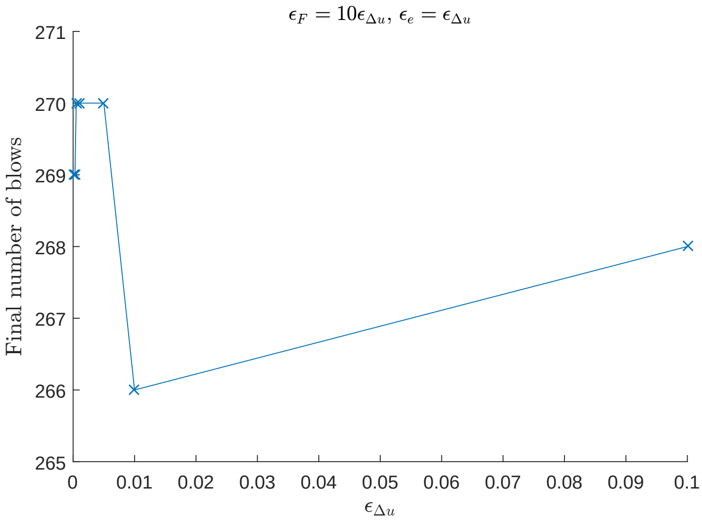

Figure F.33. Case (d): Final number of blows estimates for different values of the Newton-Raphson precisions.

F.5 Case (e) - Load parameters and structural damping

Case (e) entails varying the model parameters not related to the solution algorithm, i.e. the "physical" parameters of the hammer and pile system: The simulation time of each hammer blow, the hammer stiffness k_{ram}, the hammer damping ratio ζ_{ram} and the minimum structural damping ratio ζ_{pile}. The parameters are treated individually and only the parameter in question is changed.

All other values are identical to the ones used in case (b), see Section F.2. All simulations of case (e) have been run with a side discretization of $\Delta z = 0.1\,\text{m}$ and tip discretization $\Delta z_p = 0.05\,\text{m}$. The soil conditions can be seen in Figure F.12.

F.5.1 Influence of simulation time relative to load pulse duration

The dynamical system simulating the ram motion delivers a resulting force to the pile head for each time step for each blow. Depending on the motion of the pile head, the amplitude and shape of this motion can be slightly different for each blow, most pronounced for longer piles in stronger soils as compared to the present example.

The time for which the hammer force is zero in relation to the pulse duration (the time in which the hammer force is different from zero) can also be important, as the oscillations due to the previous blow may not have completely vanished and because gravity still acts on the structure during the time in which the hammer load is zero.

Examining Figure F.34 (where τ is the total simulation time for each blow simulation including time in which the load is zero), it is regarding the estimated number of necessary blows seen that this "zero time" is indeed more important than any of the computational parameters discussed in the previous Section F.4. Unfortunately, it does not seem as though the required simulation time per blow has converged in the investigated range. For longer simulation time relative to load pulse duration, the tip resistance and high skin friction at depths below $\approx 12\,\text{m}$ (in this example) may push the pile tip upwards a small distance during the time in which the hammer force is zero. This phenomenon also explains the higher blowcounts for longer durations seen in Figure F.35.

Ultimately, the problem is also a question of computational efficiency. The stress wave more or less vanishes after very few oscillations, i.e. for $\tau/T_{pulse} >\approx$2-3. All time steps after these are more subjected to spurious single deviations in the accelerations due to numerical errors. The pile model is configured to best handle waves at a frequency corresponding to the load, and not these spurious short motions - which means that the "zero time" is expensive and requires many iterations compared to the "load time".

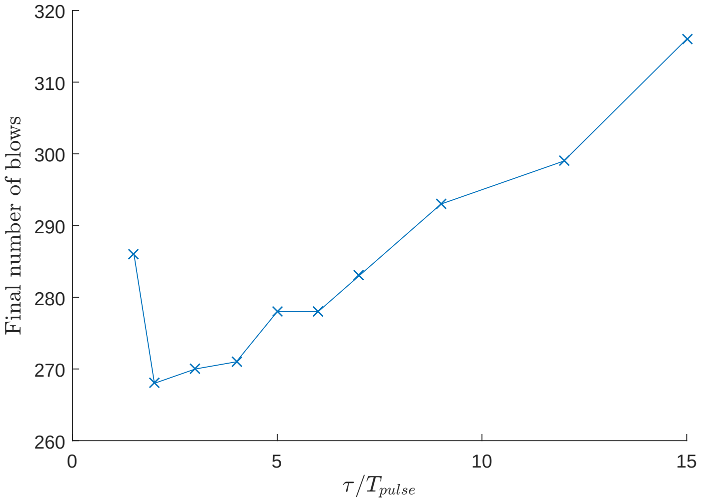

Figure F.34. Case (e): Final number of blows estimates for various relative simulation durations.

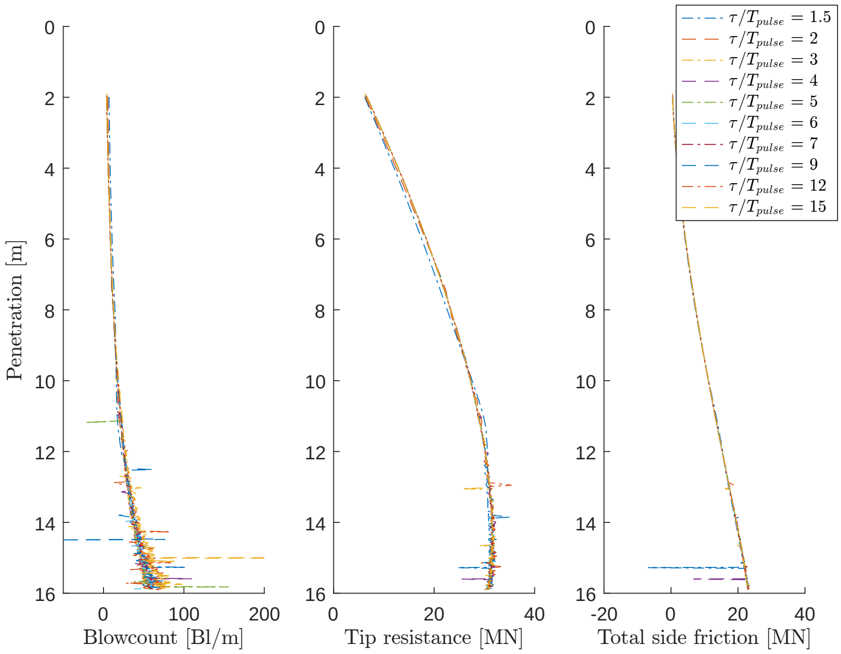

Figure F.35. Case (e): Blowcount and resistance vs. depth for various relative simulation durations, sampled at the time of maximum applied load of each blow. The largest values of τ/T_{pulse} produce the largest blowcounts in the left plot.

F.5.2 Influence of hammer stiffness k_{ram}

The hammer stiffness obviously has a major impact on the simulation, as it governs both amplitude and period of the load pulse and thus the total resistance and pile tip movement, as seen in Figure F.36. If one assumes that a 1200 kJ hammer is sufficient for driving the pile to final depth, refusal happened for hammer stiffness smaller than 1×10^9 N/m. Two values larger than this, estimated to be realistic, were examined and according to Figure F.37 it seems as though the final number of blows are converging with increase in hammer stiffness. The hammer force amplitude simply exceeds the total resistance available for a certain value.

Because the maximum pile element size is determined based on the approximate stress wavelength in the pile (which depend on the pulse duration), the number of finite elements is not constant in the investigated range of k_{ram}.

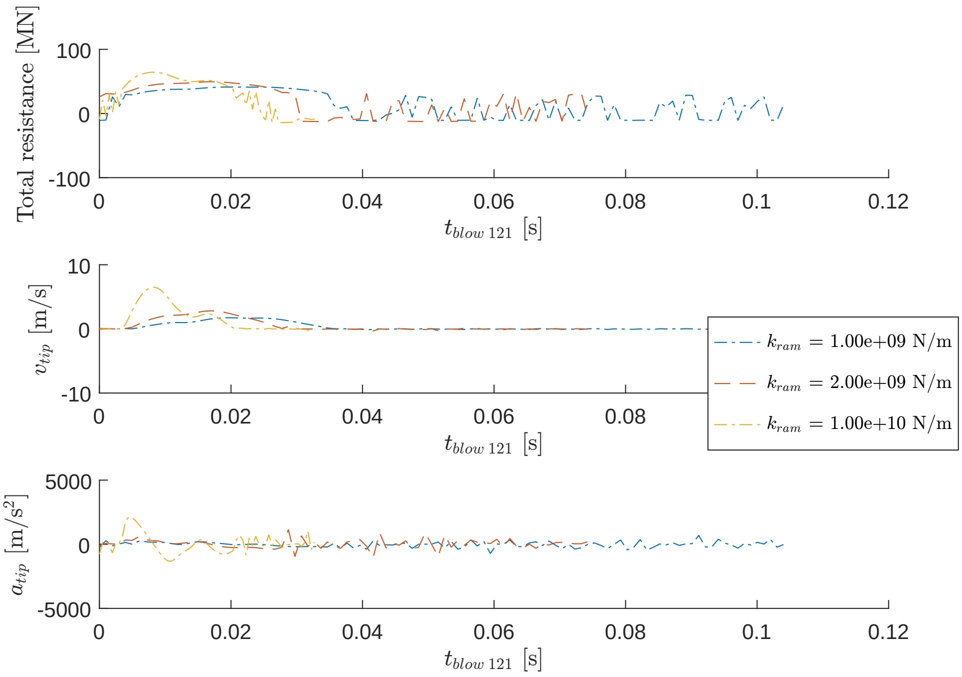

Figure F.36. Case (e): Displacement, velocity and acceleration of the pile finite element DOF representing the pile tip during blow number 121 for various values of the hammer stiffness k_{ram}.

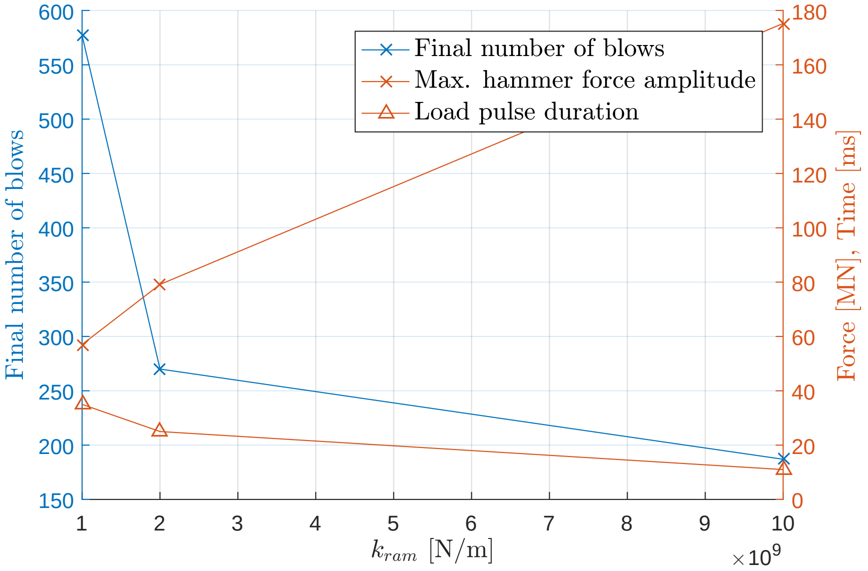

Figure F.37. Case (e): Final number of blows estimates for various values of the hammer stiffness k_{ram}.

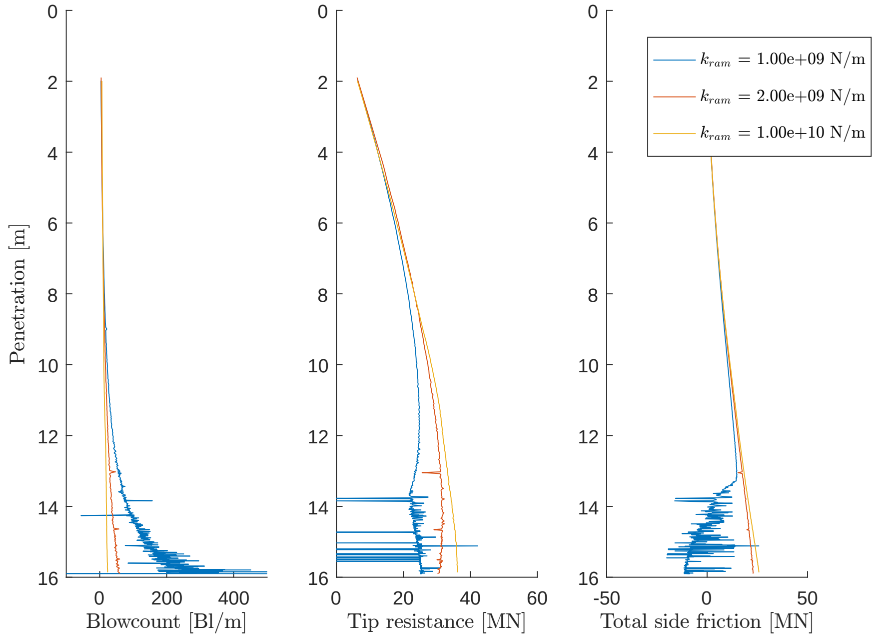

Figure F.38. Case (e): Blowcount and resistance vs. depth for various values of the hammer stiffness k_{ram}, sampled at the time of maximum applied load of each blow.

Figure F.38 shows why the hammer stiffness is important. It is not possible to determine the parameter without knowledge about impact pulse duration. The stiffness of the pile top segment is approximately 1.7×10^{11} N/m and it is clear and obvious that the hammer is more efficient (but the stress wave also has a higher amplitude) for values closer to this. For $k_{ram} = 1 \times 10^9$ N/m, the magnitude of the force is small, and the blowcount thus increases significantly as seen.

No conclusion can be made to what hammer stiffness can be correct, but it seems as though a value close to the pile stiffness would be practical in reality (depending on required fatigue damage levels) in order to minimise driving time.

F.5.3 Influence of hammer damping ratio ζ_{ram}

The hammer damping ratio mainly effects the hammer force amplitude and according to Figure F.39, this also effects the mobilised soil resistance. The duration of the pulse and the pile tip movement is not effected significantly by the value of ζ_{ram}.

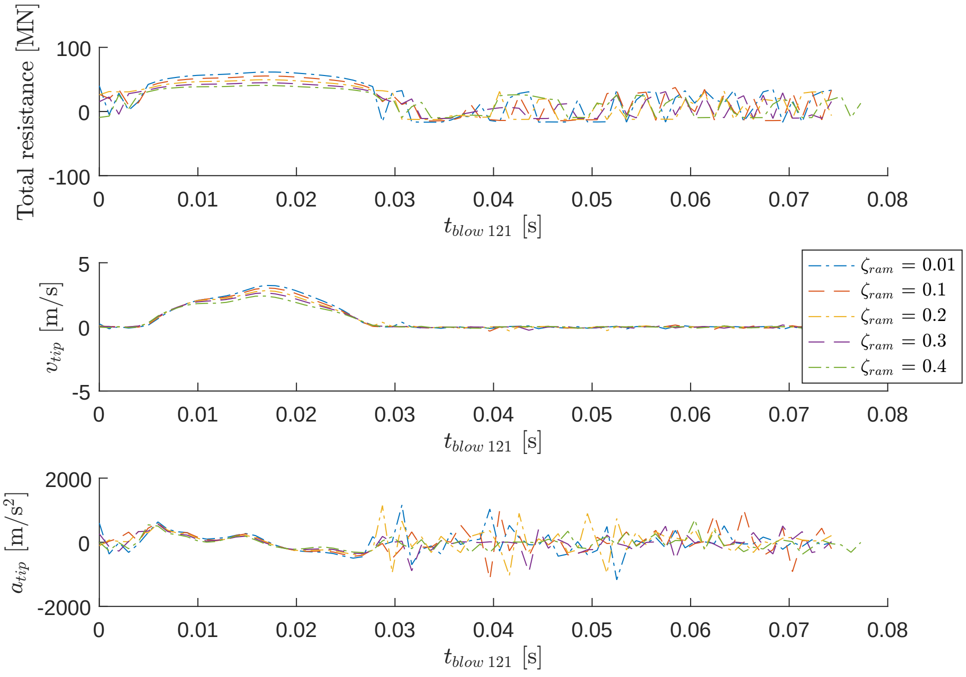

Figure F.39. Case (e): Displacement, velocity and acceleration of the pile finite element DOF representing the pile tip during blow number 121 for various values of the hammer damping ratio ζ_{ram}.

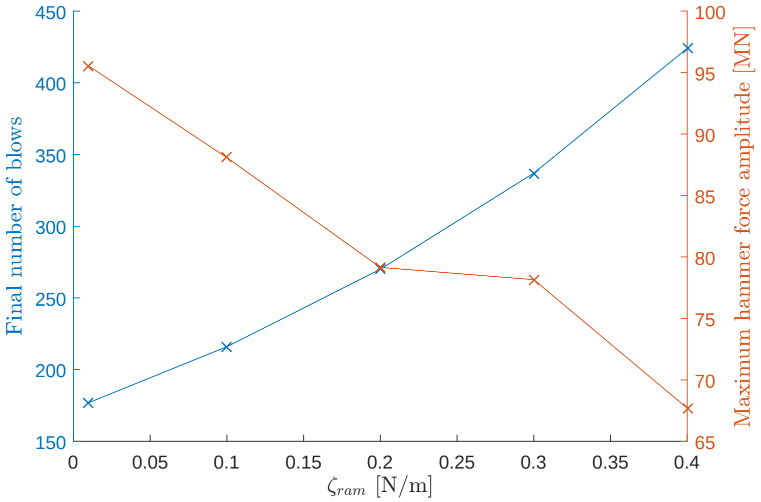

Figure F.40. Case (e): Final number of blows estimates for various values of the hammer damping ratio ζ_{ram}.

Because the damping ratio has a significant impact on the force amplitude, the total number of blows required depends heavily on the value as seen in Figure F.40. It is not clear what value the damping ratio should be, but it can logically be assumed that as small a ratio as possible is desired by the hammer manufacturer in order to maximise load amplitude and reduce energy consumption. As shown in Figure F.41, the largest values as expected gives largest blowcounts and that the mobilised soil resistance is not as smooth compared to $\zeta_{ram} \leq 0.2$. The same considerations as for

k_{ram} regarding need for calibration is applicable to ζ_{ram}, but mainly regarding maximum hammer force magnitude.

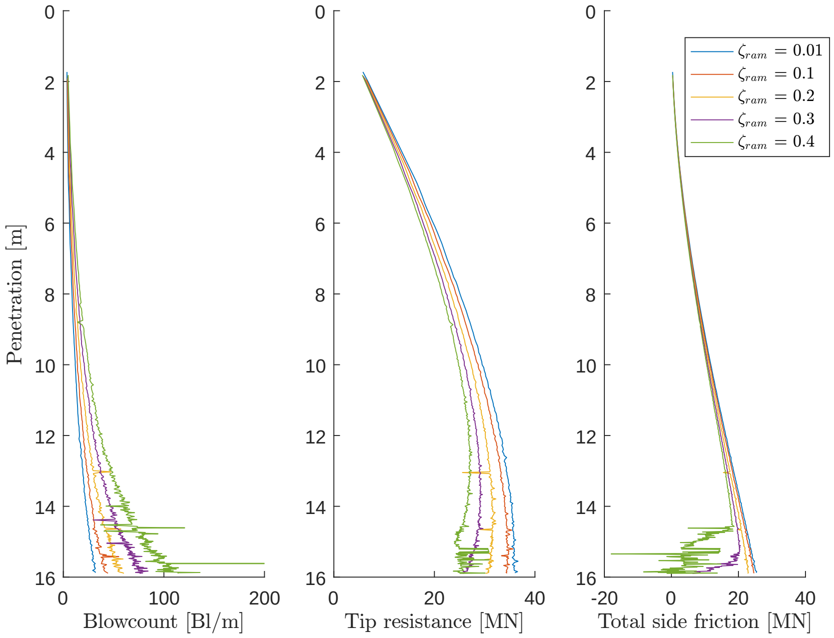

Figure F.41. Case (e): Blowcount and resistance vs. depth for various values of the hammer damping ratio ζ_{ram}, sampled at the time of maximum applied load of each blow.

F.5.4 Influence of pile structural damping ratio ζ_{pile}

The structural damping ratio is likely in the range of 0.03 to 0.08 due to the characteristics of the structure and the material. Examining Figures F.42 and F.43, it is seen that ζ_{pile} has little effect on the pile tip movement. As the stress wave is damped along the shaft the amplitude decreases for higher values, giving a larger estimate on the number of required blows. It is more conservative to choose larger values of ζ_{pile}, but it is assumed that the reference value of $\zeta_{pile} = 0.05$ is sufficiently high.

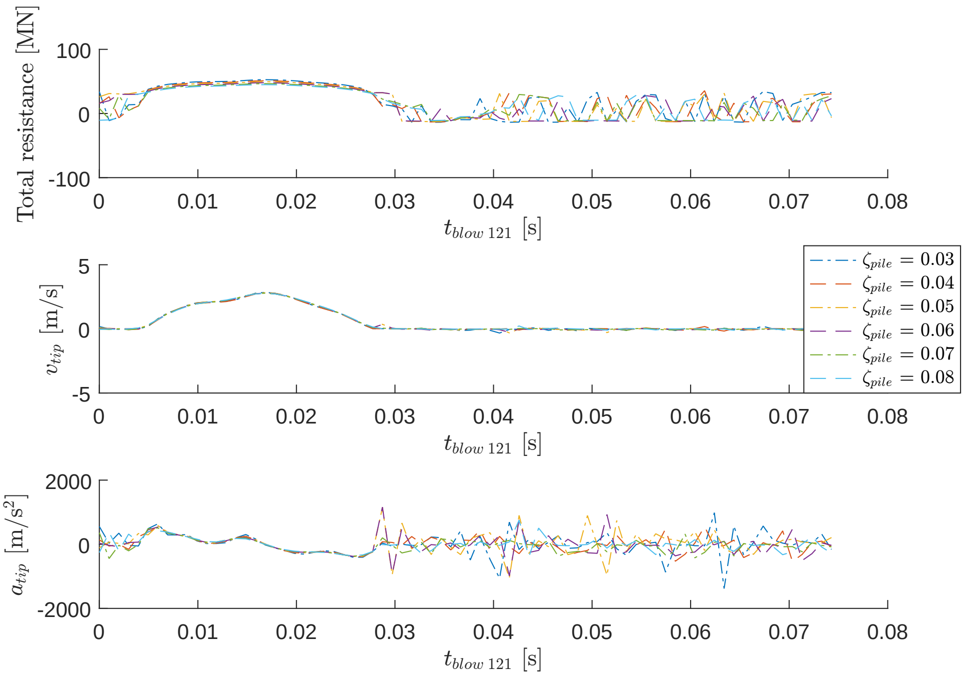

Figure F.42. Case (e): Displacement, velocity and acceleration of the pile finite element DOF representing the pile tip during blow number 121 for various values of the structural damping ratio of the pile ζ_{pile}.

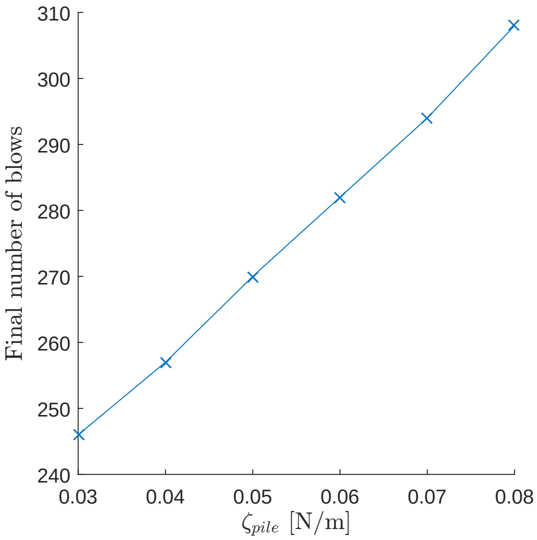

Figure F.43. Case (e): Final number of blows estimates for various values of the structural damping ratio of the pile ζ_{pile}.